Wildfires in the Euro-Mediterranean region: links with meteorological processes

Charles Hernandez

THÈSE

POUR L'OBTENTION DU GRADE DE DOCTEUR DE L'ÉCOLE POLYTECHNIQUE

SPÉCIALITÉ : MÉCANIQUE

présentée par

CHARLES HERNANDEZ

Wildfires in the Euro-Mediterranean region: links with meteorological processes

Les feux de forêts dans la région Euro-Méditerranée : liens avec la météorologie

---

Effectuée dans l'équipe

InTro

du

Laboratoire de Météorologie Dynamique

Institut Pierre Simon Laplace

2015

soutenue le 8 octobre devant le jury composé de :

Président :	R. Plougonven	LMD
Rapporteurs :	C. Flamant	LATMOS
	C. Mari	LA
Examinateurs :	N. Viovy	LSCE
	J.-L. Dupuy	URFM
Directeur :	P. Drobinski	LMD
Co-directrice :	S. Turquety	LMD

“Enfer chrétien, du feu. Enfer païen, du feu. Enfer mahométan, du feu. Enfer hindou, des flammes. A en croire les religions, Dieu est né rôtisseur.”

Victor Hugo

Abstract

The question this thesis stems from is: "To which extent weather controls the life cycle of forest fires in the Mediterranean?". The analysis developed here is based on remotely-sensed fire data, meteorological reanalyses and numerical simulations.

A large part of the thesis work focused on the impact of weather on wildfires. First I showed that weather controls the life cycle of forest fires very tightly when these fires are large enough. Many factors are crucial: the strength of the heatwave, the precipitation deficit in month preceding the summer season and finally wind speed. The relationship between fire size and wind was found very atypical by comparison with other regions (Asia, Central Europe). The largest burned areas are observed for either low wind speeds or high wind situations, with a minimum for moderate winds. This counter-intuitive behavior is observed solely during heatwaves. The causes of these different types or fire/wind relationships were identified. These results allowed to build the foundations of a statistical modeling framework that can be used to forecast not just fire risk but also the distribution of fire size and intensity. This step towards forecasting is innovative and much more informative than fire risk modeled currently used.

A second part was written about on the impact of fires on local weather. I designed a numerical sensibility study of the August 2003 Portugal fire event. In this study, I showed the triggering of inland breezes over the burned areas strengthening convection. I studied the sensibility of this phenomenon with respect to the dynamical and land-use resolution in the model. Finally I showed that burned area were favorable to increased cloudiness with an effect of increased precipitation risk (even if the precipitation signal stays very weak over the unique studied month).

Résumé

La question à la base de cette thèse est ”À quel point la météorologie contrôle le cycle de vie des feux de forêts en Méditerranée?”. L'analyse développée repose sur des observations satellitaires de feux, des réanalyses d'observations météorologiques et des simulations numériques.

Une grande partie du travail de thèse a porté sur l'impact de la météorologie sur les feux de forêts. Il a été tout d'abord été montré que la météorologie contrôle très fortement le cycle de vie des feux, quand ces feux sont très grands. Plusieurs facteurs sont déterminants: l'amplitude de la canicule, le déficit de précipitation des mois précédant la période estivale et enfin le vent. La relation entre surface brulée et vent s'est d'ailleurs révélée très atypique par rapport à d'autres régions du monde (Asie/Europe Centrale). Les plus grandes surfaces brulées sont observées soit pour des vents faibles, soit pour des vents forts avec un minimum aux vents intermédiaires. Ce comportement contre-intuitif n'est observé que pour les épisodes caniculaires. Les causes de ces différents types de relation feux-vent ont pu être identifiées. Ces travaux ont permis de poser les bases d'une modélisation statistique pour envisager la prévision non seulement du risque de feux mais du niveau d'extension et d'intensité du feu. Cette démarche vers la prévision est innovante et bien plus informative que les modèles de risque de feux en opération actuellement.

Une deuxième partie a porté sur l'impact des feux sur la météorologie en s'appuyant sur une étude numérique de sensibilité de l'épisode des feux du Portugal en août 2003. Dans cette étude, j'ai montré la formation de brises continentales au dessus des zones brulées renforant la convection. J'ai étudié la sensibilité de ce phénomène à la résolution du modèle et de la surface brulée. J'ai enfin montré que les surfaces brulées étaient favorables à la formation de nébulosité au dessus des zones affectées avec pour effet d'accrotre le risque de précipitation (même si le signal en précipitation reste très faible sur le seul mois étudié).

Acknowledgements

Ce manuscript est la dernière pierre à l'édifice d'une thèse de 3 ans passée au Laboratoire de Météorologie Dynamique. Ces trois années furent si courtes. Comme quoi, quand on se plaît quelque part, on ne voit pas le temps passer.

Je tiens tout d'abord à remercier mon directeur comme il se doit. Cette thèse n'aurait pas été possible sans un directeur aussi attentif aux besoins de ses thésards et je suis heureux d'avoir si bien choisi le mien ! Mes remerciements vont également à Solène, qui a supporté mes billevesées hasardeuses de jeune thésard avec beaucoup de flegme.

Merci Jean-Luc pour l'intérêt que tu as porté à mes travaux, ton apport a été plus qu'apprécié. Et merci Christine pour ces heures passées à décrypter ensemble les mystères des feux de forêts. C'est dans l'R du temps !

Tout ce travail m'aurait bien entendu été impossible sans l'ambiance feutrée du bureau 05 3057, aussi appelé réservoir de thésards de Philippe. Je remercie Bénédicte pour son humour, Ségolène pour sa main verte qui a tant contribué à la conversion d' O_2 en CO_2 dans ce bureau et Hiba pour son incroyable savoir-faire en matière de choix de patisseries tunisiennes.

Je tiens aussi à remercier particulièrement tous les autres thésards du laboratoire, dont le dynamisme a su contribuer à l'aération de mes neurones. En particulier j'ai une pensée pour Natacha(rme) et Aurélie, qui m'ont offert de franches parties de rigolade tout au long de ces trois ans. Merci Camill pour toutes ces cigarettes empruntées jamais rendues et Matthieu pour le nombre incalculable de fois où tu as accepté que je t'extirpe de ton bureau pour une agréable pause.

Parce que parfois le labo c'est bien, mais ailleurs c'est mieux, je remercie du fond du coeur les locataires du 8 allée Diane de Poitier. Sans rire, je ne sais pas ce que j'aurais fait si je n'avais pas eu votre agréable maisonnée pour me rappatrier le week-end. Une pensée émue va à Maxime, éminent spécialiste des chaussures de sport, pour toutes ces soirées musicales passées ensemble.

Contents

Chapter 1

Introduction

The 2003 fires in Portugal, the 2005 fires in Gallicia, the 2007 wildfires in Greece. These are all fire events in recent European history that shaped our vision of what wildfires can be. Figure 1.1 shows the evolution of the number of fires and accumulated fire size per country in the 1998–2010 time period (San-Miguel-Ayanz et al., 2013). We see that large-fire-size events, called "megafires" happened regularly all over the Mediterranean Basin. Their important costs, both in terms of lost human lives and landscape degradation, made wildfires a subject of concern for Euro-Mediterranean populations, especially with the uncertainties of a changing climate. Fire is the most important natural threat to forests and wooded areas of the Mediterranean basin. It destroys many more trees than all other natural calamities: parasite attacks, insects, tornadoes, frost, etc. Vegetation fires burnt an average 200,000 ha annually in the Mediterranean Basin between 1960 and 1970; the figure attained over 400,000 ha in the 1970's and over 600,000 ha in the 1980's. This three fold increase over 20 years is turning into an annual summer-catastrophe in the Basin, in spite of heavy investments and large budget expenditure spent to prevent and combat the scourge (Le Houérou, 1987). As stated in the first sentence of this introduction, the 2003 wildfires of Portugal are a good example of the amount of damage that large wildfires can cause in the Mediterranean region. More than 57% of the burnt area in the EU occurred in Portugal that year and over 420000 ha were burnt (EFFIS, 2003), with an accumulated cost amounting to 1 billion euros (UNEP, 2004).

Wildfires are conditioned by many factors such as the topography, the land use (Carmo et al., 2011) but also past and concomitant weather (Flannigan et al., 2009). They control the spread and thus the size of the fire, but also its intensity. The size of the fire is a diagnostic of the large and long-lasting imprints of the fire on the environment. The intensity is related to how difficult to control the fire is. It also partly explains the amount of atmospheric emissions of the fire and how high will the smoke plume rise. Weather during the fire episode is essential. Indeed, the wind speed determines the rate of spread of the fire and the fire-line intensity (Rothermel, 1972). Few weeks before the fire episode, wind speed,

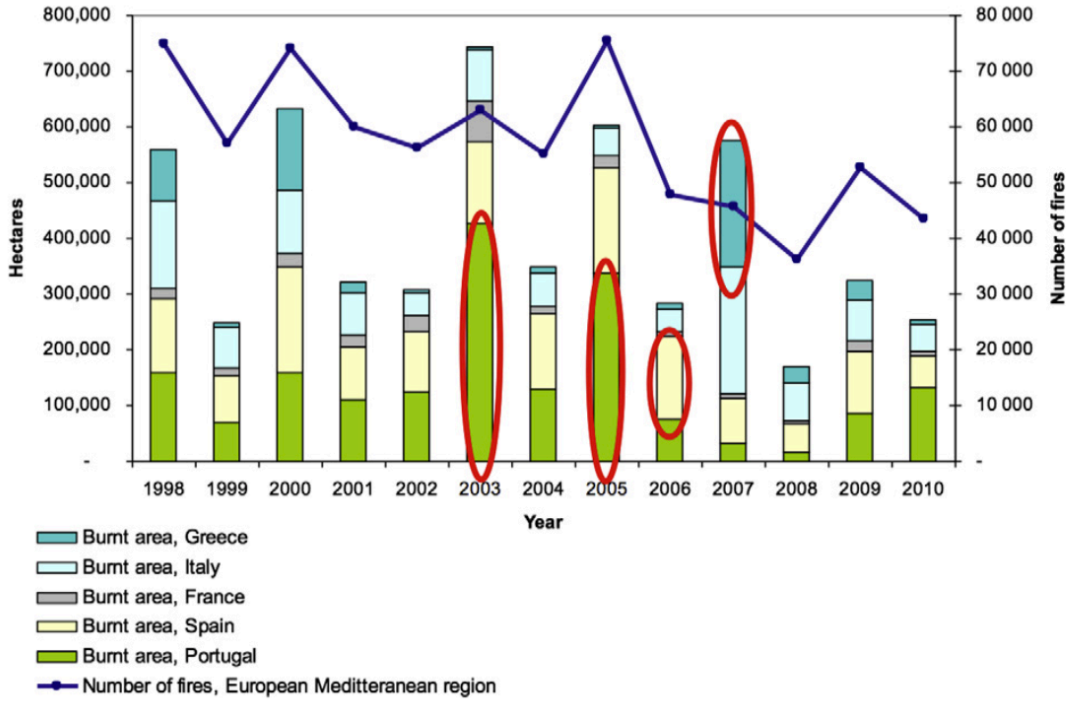

FIGURE 1.1: Time series of the number of fires and accumulated fire size per country during the 1998–2010 time period in the Euro-Mediterranean region (San-Miguel-Ayanz et al., 2013). Marked red are the so called "megafire" events, characterized by large numbers of synchronous fires in the same region.

insolation, humidity and temperature influence fuel moisture by controlling water fluxes in dead and live fuels (Aguado et al., 2007, Castro et al., 2003, Matthews, 2006, Sharples et al., 2009) whereas few months to several years before, they mainly control the vegetation growth and so the fuel amount. For instance, Stéfanon et al. (2012a) show that a springtime meteorological drought, characterized by several months of cloudiness and precipitation deficit, leads to unusually high solar radiation which is beneficial for vegetation growth. In 2003, this unusual excess of vegetation lasted until the end of July when the vegetation started dying leading to large fuel amount and low fuel moisture, favorable to high fire risk. Meteorological conditions propitious to high fire risk have already been investigated in previous work. Flannigan et al. (2001) showed that warm, dry and windy days are correlated to higher burnt area, and that certain synoptic conditions such as the breakdown of an upper blocking ridge lead to particularly favorable conditions for wildfires. Before this work, Flannigan and Harrington (1988) already observed that, in Canada, high fire risk was associated with long sequences of dry and low precipitations days. In the Mediterranean region, Pereira et al. (2005) found that days with large burnt area in Portugal are concomitant with atmospheric blocking regimes in summer, as can be seen in Figure 1.2. These findings are corroborated by Hoinka et al. (2009) and Levin and Saaroni (1999), which find characteristic synoptic patterns associated with wildfire occurrence in Iberia and Israel respectively.

Conversely, burnt scars left by wildfires can impact meteorology by changing the heat flux balance at the surface. Mölders and Kramm (2007) showed that in boreal regions fires tend to thaw the permafrost

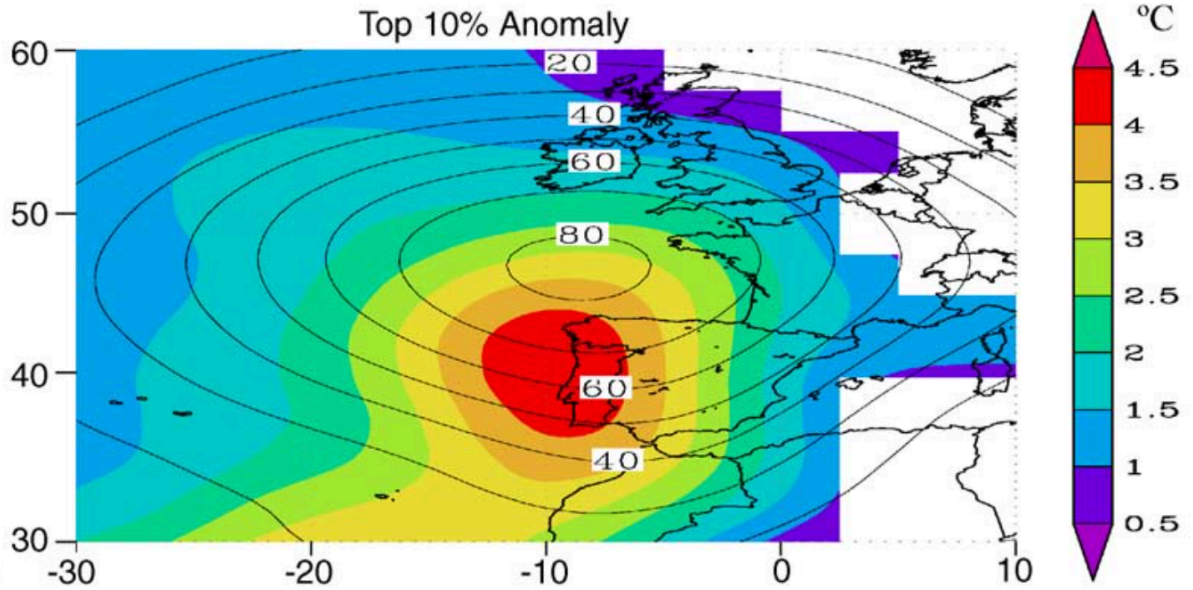

FIGURE 1.2: Composite of 500-hPa (contours) and 850-hPa temperature anomalies (colors) corresponding to the top 10% days in terms of recorded fire size (Pereira et al., 2005). Points under the 99% confidence level are not shown.

layer of the soil, blacken the surface and decrease the roughness length. These surface heterogeneities induce meso-scale circulations (Avissar and Schmidt, 1998, Pielke et al., 1991, Segal et al., 1988) which can have consequences on the local meteorology (Kilinc, 2007, Wendt et al., 2007). Tryhorn et al. (2008) also showed evidence of the link between flash floods that occurred in the Alpine Shire, Australia with 37.2 mm recorded precipitation. The numerical experiment showed that without accounting for the fire occurrence the simulated precipitation were 3.9 mm versus 31.7 mm when accounting for the fire occurrence. At a larger time scale, Görgen et al. (2006) showed by using a fire/regrowth scheme in a climate model, that the vegetation regrowth time scale depends on the intensity of the fire.

In the Mediterranean, temperature anomalies (Bedia et al., 2014) and summer droughts (Dimitrakopoulos et al., 2011) are also critical to explain fire occurrence. On longer time scales, the aridity level is also linked with large fire occurrence (Pausas and Paula, 2012). In Greece, Koutsias et al. (2013) found a positive correlation between 2 years lagged precipitations and burnt area. This climatic driving of burnt area will be impacted by climate and land cover changes. In particular the combination of several factors including rural depopulation and increased fire frequency due to rising temperatures in southern Europe could lead to a general change in the dominant vegetation species, with a predominance of shrublands over forested areas (Moreira et al., 2011). Other studies suggest that the change in fire regime will be different whether the climate shifts towards warmer-drier (less fire activity) or warmer-wetter (more fire activity) conditions in the Mediterranean Basin (Batllori et al., 2013), a question which remains unanswered.

In this thesis I wish to shed light on the physical mechanisms that link wildfire characteristic properties such as their size and intensity to weather phenomena. We will focus on three primary scientific objectives:

- What are the meteorological conditions favorable to wildfires in the Mediterranean area ?
- How can we improve the forecasts of fire danger in this region ?
- To which extent burnt scars impact local weather ?

It seems logical and intuitive that heatwave situations, characterized by low wind speeds, high temperature anomaly and the extreme drying of the forests they trigger, would be linked to large wildfire occurrence. Paradoxically high winds should also lead to large wildfires, as such is suggested by early mathematical implementation of fire rate of spread (Rothermel, 1972). Indeed the strong oxygenation driven by the wind kindles the fire even further. To study this paradox we should first gather extensive data sets over the Euro-Mediterranean region. This has been made possible by satellite observations. Here we use data from the Moderate Resolution Imaging Spectroradiometer (MODIS) instruments, on board of NASA Terra and Aqua satellites since 2003, which provides maps of new burnt area and instantaneous fire intensity over the globe four times a day. Linked with meteorological reanalysis provided by the European Centre for Medium-range Weather Forecasts (ECMWF), these data will help us study the behavior of fire size and intensity with respect to wind speed, synoptic patterns and heatwave occurrence. This will help us answer our first question.

Stemming from our new understanding of specific phenomena governing fire size and intensity, our next step will be to statistically model these two parameters with respect to weather. Our main goal will be to derive probabilities that, knowing that a fire began to spread, its size will exceed a large threshold or its intensity will be so high that firefighters will not be able to control it. To get to this goal I first studied the statistical distribution of these two fire parameters. Then I designed a methodology to infer their conditional distribution with respect to weather covariates in order to compute the extreme fire probabilities. These final probabilities could then be used in a fire danger assessment system, alongside with other modern methods such as burn probability maps (Miller et al., 2008) or real-time physical simulations of fire spread (Kochanski et al., 2013).

Focusing on the third objective I used the Weather Research and Forecast (WRF) atmospheric model and considered as an example the 2003 fires of Portugal. I used different models to take into account the land-surface modifications that fire induces. They correspond to different ages of the fire burnt scar and allow the assessment of the this parameter on the atmospheric flow modifications. Dynamical and land-use downscaling was performed to test the robustness of the results.

This thesis will be organized as follows. In Chapter 2 I will focus on the links between heatwaves, synoptic patterns and wind speed and large wildfires. In Chapter 3 contains my findings about the computation of extreme fire probabilities. In the following Chapter 4 I will discuss the impact of burnt scars on meteorology. Chapter 5 contains the general conclusion of this Ph.D. thesis manuscript and indications for further work on the topic.

Chapter 2

Influence of meteorology on wildfire size and intensity

This chapter is the synthesis of two articles Hernandez et al. (2015c) and Hernandez et al. (2015a), published in Natural Hazard and Earth System Sciences and Annales Geophysicae respectively.

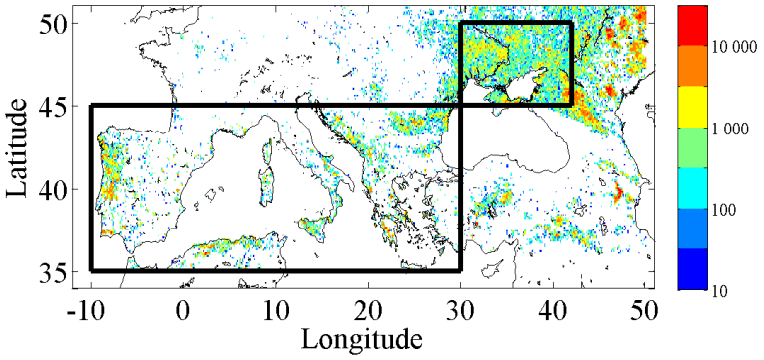

FIGURE 2.1: 10-years cumulated burnt area (in ha) for each 10-km-regridded MODIS MCD64A1 fire product grid cell over the Euro-Mediterranean region (in colors). The Mediterranean domain (MED) and central eastern Europe domain (EAST) are identified by black boxes.

The study domains of both sections is displayed in Figure 2.1. The Mediterranean domain, called MED in the following, encompasses all the Mediterranean Basin and is dominated by forests and chaparral. The Eastern Europe domain (EAST in Section 2.4) covers western Ukraine and here agricultural fields are prevalent. These two domains also differ by their aridity levels (the Mediterranean Basin is drier than the Eastern Europe area) and their orography, the landscape being much flatter in the Eastern Europe region.

In the first section of this chapter we investigate the synoptic conditions favorable to wildfires in the Mediterranean region, in terms of fire intensity and burnt area. As reported in the literature, Mediterranean large wildfires are associated with a blocking situation. However, this study shows the existence of two types of wildfires, controlled by the blocking high intensity: (1) fast build-up of a weak blocking produces intense wildfires associated with strong winds which allow propagation over long distances; (2) longer build-up of strong blocking situation produces less intense wildfires associated with weaker winds which also propagate over long distances. Another major step forward of this study in the understanding of the drivers of those wildfires, is the evidence of a perfect match between the period of wildfire activity and the persistence of the favorable synoptic conditions: the wildfire activity starts at the onset of the blocking situation and ends with the transition to less favorable synoptic weather pattern. Such strong control of the wildfire activity by the concomitant weather is a very promising result regarding fire risk management, especially considering the accidental nature of the Mediterranean wildfires.

In the second section, MODIS satellite observations of fire size and ERA-Interim meteorological reanalysis are used to derive a relationship between burnt area and wind speed over the Mediterranean region and Eastern Europe. As intuitively expected, the burnt area associated to the largest wildfires is an increasing function of wind speed in most situations. It is always the case in Eastern Europe. It is also the case in the Mediterranean for moderate temperature anomaly. In situations of severe heatwaves, the relationship between burnt area and wind speed displays a bimodal shape. Burnt areas are large for low 10-meter wind speed (lower than 2 m s^{-1}), decrease for moderate wind speed values (lower than 5 m s^{-1} and larger than 2 m s^{-1}) and increase again for large wind speed (larger than 5 m s^{-1}). To explain such behavior fire propagation is investigated using a probabilistic cellular automaton model. The observed relationship between burnt area and wind speed can be interpreted in terms of percolation threshold which mainly depends on local terrain slope and vegetation state (type, density, fuel moisture). In eastern Europe, the percolation threshold is never exceeded for observed wind speeds. In the Mediterranean Basin we see two behaviors. During moderately hot weather, the percolation threshold is passed when the wind grows strong. On the other hand, in situations of severe Mediterranean heatwaves, moderate wind speed values impair the propagation of the wildfire against the wind and do not sufficiently accelerate the forward propagation to allow a growth of wildfire size.

2.1 Context and introduction

Wildfire propagation is impacted by various conditions such as fuel moisture and load, human activities and short to long term weather (Flannigan et al., 2009). Wind speed is one of the main factors regarding the weather dependency, as it drives the rate of spread and direction of propagation (Rothermel, 1972).

Fuel moisture is also an important factor for the propagation of wildfires (Sharples, 2008). It depends on short (i.e. hour time scale) to medium (i.e. seasonal time scale) variability of temperature, precipitations and relative humidity.

The relationships between weather, vegetation and wildfire burnt area have been investigated in several works. Flannigan et al. (2001) link seasonal burnt area with weather at various time and spatial scales (several years to a few days; global to local) and show that warm, dry and windy days are correlated to higher burnt area, and that certain synoptic conditions such as the breakdown of an upper blocking ridge leads to particularly favorable conditions for wildfires. Flannigan and Harrington (1988) show the weather dependency of monthly burnt area with long sequences of dry and low precipitations days. These relationships have been extrapolated for forecasting future wildfire severity in a changing climate. The review by Flannigan et al. (2009) indicates with a high confidence that climate change should lead a positive trend of burnt area. This is already measurable in the western US, as suggested by Westerling et al. (2006) and Running (2006). Increase in the fire season duration, higher summer temperature, earlier melting of snowpacks and expansion of the areas susceptible to wildfires to elevated forests combine their effects, leading in this region to higher seasonal burnt area since the mid 1980s.

In the Mediterranean region the synoptic weather conditions favorable to Mediterranean wildfires are either blocking (Pereira et al., 2005) or trough (Levin and Saaroni, 1999). Weather on longer time-scales can also be of importance, as stated by Koutsias et al. (2013) who found a positive correlation between 2 years lagged precipitations and burnt area in Greece. This climatic driving of burnt area will be impacted by climate and land cover changes. In particular the combination of several factors including rural depopulation and increased fire frequency due to rising temperatures in southern Europe could lead to a general change in the dominant vegetation species, with a predominance of shrublands over forested areas (Moreira et al., 2011). Other studies suggest that the change in fire regime will be different whether the climate shifts towards warmer-drier (less fire activity) or warmer-wetter (more fire activity) conditions in the Mediterranean Basin (Batllori et al., 2013), a question which remains unanswered.

In this chapter we also focus on fire intensity. We cannot directly retrieve this intensity for a large number of fires. Instead we will use a related diagnostic, the fire radiative power (FRP). The FRP can be used for biomass combustion rate inference (Ichoku et al., 2008, Wooster et al., 2005), wildfire atmospheric emissions (Turquety et al., 2014). It is also part of the explanatory factors of their injection height (Val Martin et al., 2010). For intensity weather is also essential. Indeed, the wind speed determines the rate of spread of the fire and the fire-line intensity (Rothermel, 1972). Drought and heatwave-related fuel drying is also of critical importance for fire line intensity calculation (Mendes-Lopes et al., 2003).

In order to further these studies, our aim is to analyze the role of short and mid-term weather on the burnt area in the Euro-Mediterranean region, characterized by a variety of land-uses (natural forests, chaparral, agricultural fields), high exposure to heatwaves (Stéfanon et al., 2012b) and a high wildfire activity.

Wildfires in the Mediterranean region tend to be generally caused by accidents (Ganteaume et al., 2013, Silva et al., 2010a) and in eastern Europe they are mostly linked to agricultural practices (Turquety et al., 2014). Here we will not study the causes of wildfire activity but the dependency between fire size and weather, in particular wind speed and temperature anomaly. The first section furthers the works of Pereira et al. (2005) on linkage between synoptic weather and large or intense wildfire occurrence. The second section continues the work of Cardil et al. (2014) on the link between temperature anomalies and wildfire size and the work of Pausas and Paula (2012) and Loepfe et al. (2014) on threshold effects on wildfire propagation (e.g. threshold on aridity level) by analyzing the influence of wind speed on burnt area.

2.2 Fire and weather data

2.2.1 Data sources

Our weather database was built upon the ERA-Interim reanalysis of the European Center for Mean-range Weather Forecast (ECMWF) (Dee et al., 2011). For each day of detected wildfire, we use the surface wind speed and temperature, as well as the 500 hPa geopotential height and wind speed at 1200 UTC. These data allow the characterization of the synoptic weather conditions associated with the fire episode, as well as an indication of the meteorological environment of the fire at the surface. The horizontal resolution of the reanalysis does not allow the derivation of the small-scale weather conditions in the immediate vicinity of the fire. The detection of fires is performed using the fire products from MODIS (Moderate Resolution Imaging Spectroradiometer), an instrument carried on board of the Aqua and Terra polar heliosynchronous orbiting satellites. These products are the burnt area (BA) and the fire radiative power (FRP) which can be seen as a proxy of the fire intensity. The FRP is retrieved by using measured radiance of the 4 μm and 11 μm channels at nadir. Other spectral bands are used for assessing cloud masking, glint, bright surface and other sources of false alarms and disturbances. The FRP is provided at 1 km resolution by the MOD14 product. The BA is retrieved from the observed changes in land cover. Indeed, the albedo is modified by the deposition of charcoal and ash, the loss of vegetation and the change in fuel bed characteristics. Albedo alteration produces changes in surface reflectance which are processed to produce daily burnt area at a 500 m resolution in the MDC64 product (Giglio et al., 2010). Only the fraction of the detected burning pixel covered by vegetation is burned following Turquety et al. (2014). The FRP and BA products are then regridded at 10 km resolution which was chosen to be a good trade-off in order to keep detailed enough information on the fire location and facilitate the comparison with the ERA-Interim meteorological data. We use the first 10 years (2003-2012) of MODIS data. Figure 2.2 shows the total burnt area, mean fire intensity and associated fire counts for the 2003-2012 time period. We see that fire intensity and the associated number of fire have low interannual variability whereas burnt area is dominated by 4 extreme events, years 2003, 2005, 2007 and 2012. It should be noted that there are important uncertainties on the date of beginning of wildfires taken individually. The

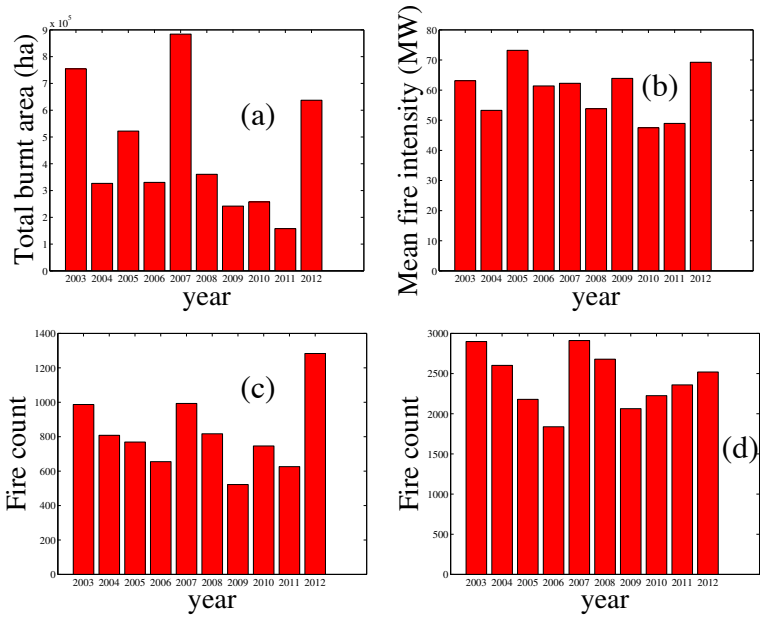

FIGURE 2.2: Total burnt area (a), mean fire intensity (b) and fire counts associated with BA (c) and FRP (d) detection for the 2003-2012 time period.

incertitude can be as large as 5 days and is caused by several factors such as cloud cover impairment of remote sensing and lack of detection of wildfires at the beginning of their development. As we deal with statistics (average, ...) on large number of such wildfires, the uncertainty is reduced. In the following we will call this burnt area data set MODIS. We also use the EFFIS (European Forest Fire Information System) Rapid Damage Assessment system, provided by the Joint Research Center (JRC) of the European Commission (European Commission, 2010). This set is built using 250-meter MODIS images. A first step of automated classification is used to isolate fire events and a post-processing using human visualization of the burnt scar is performed. A cross-analysis using the active fire MODIS product, land-cover data sets as well as fire event news collected in the EFFIS News module is finally done to ensure a low number of misclassifications (`http://forest.jrc.ec.europa.eu/effis/`). The system records burnt areas of approximately 40 ha and larger (Sedano et al., 2013). The JRC provided the data for the 2006-2012 time period. In this thesis we only take into account wildfires recorded in July and August, so as to focus on the summer period when most large wildfires can be found in the Mediterranean. We call this burnt area data set EFFIS in the following.

2.2.2 Processing

A 3-D (latitude, longitude and time) connected component algorithm is used to determine what are the distinct fire events in the MODIS data set. This algorithm aggregates the adjacent fire spots into larger fire events. The main interest of this method is that it allows for the detection of wildfires larger than 10,000 ha which are those expected to be most influenced by weather conditions (e.g. Pereira et al.,

2005). The main weakness is that it does not take into account cloud cover impairment of remote sensing. Indeed an absence of detection of 1 day between two detections could be caused by clouds. Another problem is that two independent fire event taking place close to one another (less than 20 km of distance and less than a day between the end of the first event and the beginning of the second) are considered the same by this method. Megafire events, such as defined by San-Miguel-Ayanz et al. (2013), could also grouped in clusters with this method of analysis. In this work we will often work using the date of beginning of the wildfires (t_0) and its duration (Δt). The date of beginning will be the date of first detection of the fire event and the duration the number of consecutive days of detection. For fires in the Mediterranean Basin (MODIS set) the mean duration is approximately 2.5 days.
The processing of the EFFIS data set is simpler. The data set provides the shape and time of beginning of all detected wildfires. We take as location of the centroid of this shape.
To link the weather data to the fire data, we take the ERA-Interim grid point nearest from the detected fire event. We then associate to this event the weather recorded at 1200UTC the day of first detection.
In this study we focus on the Mediterranean Basin. We therefore select the fires occurring within the box Lat $\in [35^o$ N,50^oN] and Lon $\in$ [-10^o E,50^oE].
Detection of smaller wildfires being quite hard with remote sensing techniques, we chose to eliminate $<25ha$ wildfires from our burnt area data sets. They correspond to wildfires burning less than one pixel in the MODIS data set and we have doubts about the completeness of the *BA* data sets below this value. We also retain only wildfires occurring during the months of July and August in order to focus on the core of the fire season in the study area (Ganteaume et al., 2013) and to avoid a seasonal change in driving factors. In the following sections it should therefore be stressed out that the obtained results only hold for such wildfires.
After these preprocessing steps we retain 5821 observations for the MODIS data set, 4840 for the EFFIS data set and 24273 wildfires for the FRP data set.

2.3 How much does meteorology control wildfire size and intensity ?

2.3.1 Fire and weather drivers

Figure 2.3 displays the variations of the 95^{th} quantile of the BA at the end of the fire and the FRP at the fire mature stage (first day) with respect to the 10-m wind speed at 1200 UTC on the first day of each fire over the whole Mediterranean region. The focus on the largest and most intense fires is justified as these fires are the most dependent on the meteorology (e.g. Pereira et al., 2005). The quantities BA and FRP are clustered in two categories of 2-m temperature anomaly with respect to the climatology (ΔT_2), i.e. $\Delta T_2 < 3°$C and $\Delta T_2 > 3°$C. A 3°C temperature anomaly represents the $75^t h$ percentile of the temperature anomaly CDF (Stéfanon et al., 2014). It thus includes all heatwaves among them the most severe ones. For each subfigure the data is separated in 7 bins of equal number of fires. The 95^{th} quantile and its corresponding 70% (BA) and 90% (FRP) confidence intervals are then computed using 1000 bootstrap

resamplings. Those confidence levels correspond to the maximum levels of significance possible for each subplot. Figure 2.3 shows a general growth with respect to the 2-m temperature anomaly in most

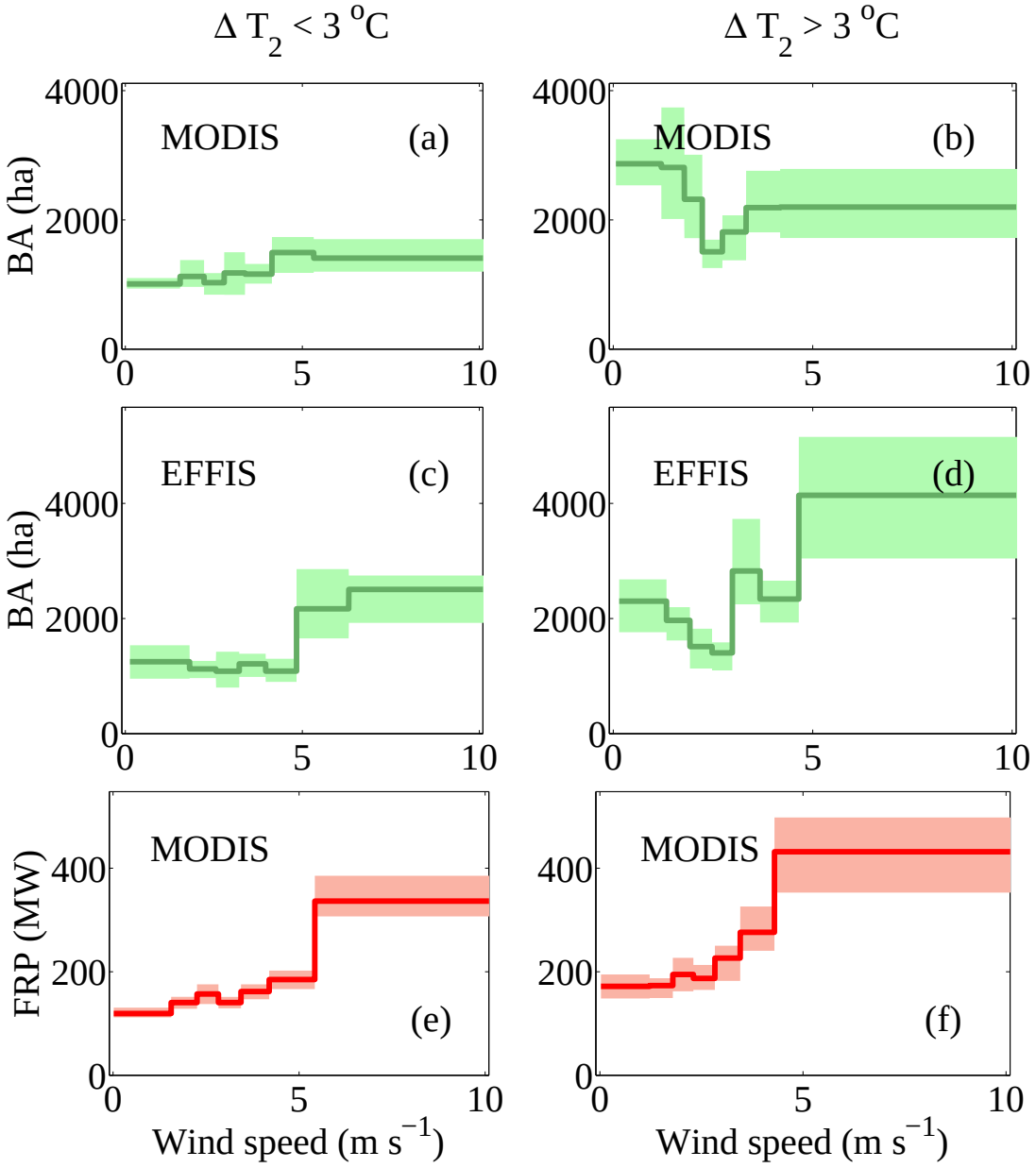

FIGURE 2.3: Burnt area (BA) at the end of the fire (upper and middle rows, a, b, c & d) and fire radiative power (FRP) at the fire mature stage (first day) (lower row, e & f) with respect to the 10-m wind speed at 1200 UTC on the first day of each fire over the whole Mediterranean region. For BA the upper row corresponds to the MODIS data set and the middle row to the EFFIS data set. The solid line represents the 95th quantiles (q_{95}) of BA (upper and middle row) and FRP (lower row). The green shaded area represents the 70% confidence intervals (BA) and the red shaded area the 90% confidence intervals (FRP). The quantities BA and FRP are clustered in two categories of 2-m temperature anomaly with respect to the climatology (ΔT_2), i.e. $\Delta T_2 < 3°C$ (left column) and $\Delta T_2 > 3°C$ (right column). For each subfigure the data is separated in 7 bins of equal number of fires.

cases. Indeed, BA ranges between 1,500 and 1,800 ha for $\Delta T_2 < 3°C$ and between 1,800 and 4,000 ha for $\Delta T_2 > 3°C$. This is explained by the fact that high values of ΔT_2 imply, during summer, the presence of a drought (Stéfanon et al., 2012b) and therefore strong fuel drying over large regions. Figure 2.3 also shows a peculiar dependence of BA with respect to wind speed in the Mediterranean region. For low temperature anomaly ($\Delta T_2 < 3°C$), BA increases with surface wind speed. Since the rate of fire spread is a growing function of the ambient wind, stronger winds should produce larger wildfires (Rothermel, 1972). Conversely, for high temperature anomaly ($\Delta T_2 > 3°C$), the evolution of BA as a function of wind speed is "bimodal". Large values of BA around 3,000 ha are found for low wind speed (< 2 m s^{-1} in ERA-Interim), followed by smaller values around 1,800 ha for intermediate wind speed (between 2 m s^{-1} and 4 m s^{-1} in ERA-Interim), followed by larger values again around 2,200 ha for large wind speed (between > 4 m s^{-1} in ERA-Interim). In the following, in case the temperature anomaly exceeds 3°C, the situation corresponding to a wind speed weaker than 2 m s^{-1} will be referred as the heatwave mode (HWM), whereas the situation corresponding to a wind speed stronger than 4 m s^{-1} will be referred as the wind forced mode (WFM). Such behavior in Section 2.4. As can be seen in Table 2.1, the HWM wildfires have a longer duration than the WFM wildfires, they can therefore burn over larger areas. Indeed, in the absence of strong wind speed, there is then no dominant direction of propagation. Thus those wildfires can, albeit more slowly than WFM wildfires, expand in all directions and burn a large area since they have a lower probability to be stopped in all directions than in one specific propagation direction. The local minimum for moderate values of wind speed can be interpreted as due to the strong reduction in back-propagation of the fires which is not compensated by the enhancement in forward propagation. More development on this topic will be done in Section 2.4. The behavior of FRP is

Parameter	Heat wave mode (HWM)	Wind forced mode (WFM)
Number of wildfires	98	67
Median size (ha)	2731 ± 255	2039 ± 223
Median duration (days)	8.36 ± 0.47	6.96 ± 0.27
Median propagation rate (ha day^{-1})	349 ± 34	385 ± 44

TABLE 2.1: Table of median BA values, duration and propagation rate of HWM and WFM wildfires. We take only the wildfires with a size in the top 10%.

simpler than that of BA since this quantity is the instantaneous response of the fire intensity with regards to its environment. Like BA, FRP also increases with the temperature anomaly. FRP ranges between 150 and 350 MW for $\Delta T_2 < 3°C$ and between 200 and 400 MW for $\Delta T_2 > 3°C$. This is due to the fact that dryer fuels mean higher fire intensity. Therefore the FRP is larger with these dryer fuels, as less energy is wasted for water evaporation. And since the rate of spread is also a growing function of the ambient wind, high surface winds mean higher fire intensity, hence higher FRP, with consequences on fire combustion emission injection height (Val Martin et al., 2010).

The synoptic conditions associated with these observed maxima of BA and FRP (Fig. 2.3) are shown in Fig. 2.4 for the Iberian Peninsula, as it represents more than half of the burnt area of the European Union (EFFIS, 2003, Silva et al., 2010b). Figure 2.4 represents composites of the 500-hPa geopotential height

anomaly and of temperature anomaly for initiating HWM and WFM wildfires. It clearly shows that the HWM wildfires are associated with synoptic blocking with a high pressure anomaly pattern located over Western Europe, which resembles to the pattern of Pereira et al. (2005) and Stéfanon et al. (2012b) (e.g. Western Europe cluster in their Fig. 2). The WFM wildfires are also associated with a blocking-like pattern with however a weaker anticyclonic anomaly elongated along a curved ridge. The difference of blocking patterns are not associated with a different phase of one identical fire episode. The HWM and WFM wildfires are totally distinct fire episodes as will be shown in the following section. One can eventually notice that the pattern are not sensitive to the fire diagnostic, i.e. BA or FRP, used to compute the composites. Finally, the favorable conditions corresponding to the extreme wildfires are similar to those found in Pereira et al. (2005). Student's T tests were performed on Fig. 2.4 to determine if these composites are statistically different from the climatology. We find that they are at the 99.9% confidence level. Composites of HWM and WFM are also statistically different at the 99.9% confidence level.

Figure 2.5 shows the total burnt area, mean fire intensity and associated fire counts for fires classified in either HWM or WFM. Over 2003-2012 period, the figure shows that on average, the number of fires associated with HWM is slightly larger than the number of fires associated with WFM. HWM mode fires contributed significantly more to the burnt area for years 2003 and 2005. Interestingly, year 2007 is remarkable in terms of total burnt area but it is well balanced between the 2 modes. Such behavior is not reproduced when looking at the fire intensity. For all years, the most intense fires are associated with WFM mode fires.
How strongly these favorable conditions control the life cycle of the fire episode is still an open question, especially considering that wildfires in the Mediterranean region are generally caused by accidents (Ganteaume et al., 2013, Le Houérou, 1987, Silva et al., 2010b).

2.3.2 Fire life cycle and weather variability

Figure 2.6 shows the time sequences of the composites over the Iberian Peninsula of the 500-hPa geopotential height anomaly for HWM and WFM wildfires. The composite charts are shown at time $t_0 - 3\Delta t$, $t_0 - \Delta t$, t_0, $t_0 + \Delta t$ and $t_0 + 3\Delta t$, with t_0 the fire starting date and Δt the fire duration. As shown before in Fig. 2.4, the patterns are identical when the FRP diagnostic is used and is thus not shown. This example for the Iberian Peninsula will be generalized in the following. In the HWM situation, Fig. 2.6 shows the build-up of the blocking high north of the Peninsula few days before the wildfire episode but still remains weak ($t_0 - 3\Delta t$ to $t_0 - \Delta t$). The anticyclonic anomaly strengthens very quickly at the time of the wildfire (t_0) and weakens quickly at the end ($t_0 + \Delta t$). The anomaly disappears few days after the episode ($t_0 + 3\Delta t$). The sequence for the WFM situation is very similar, except that the build-up of the blocking high is shorter (about Δt), weaker and further east compared to HWM situation. The anticyclonic anomaly has almost totally disappeared at the end of the wildfire episode ($t_0 + \Delta t$). The striking result here is that the time sequence is chosen based on the fire life cycle only (initiation date and fire

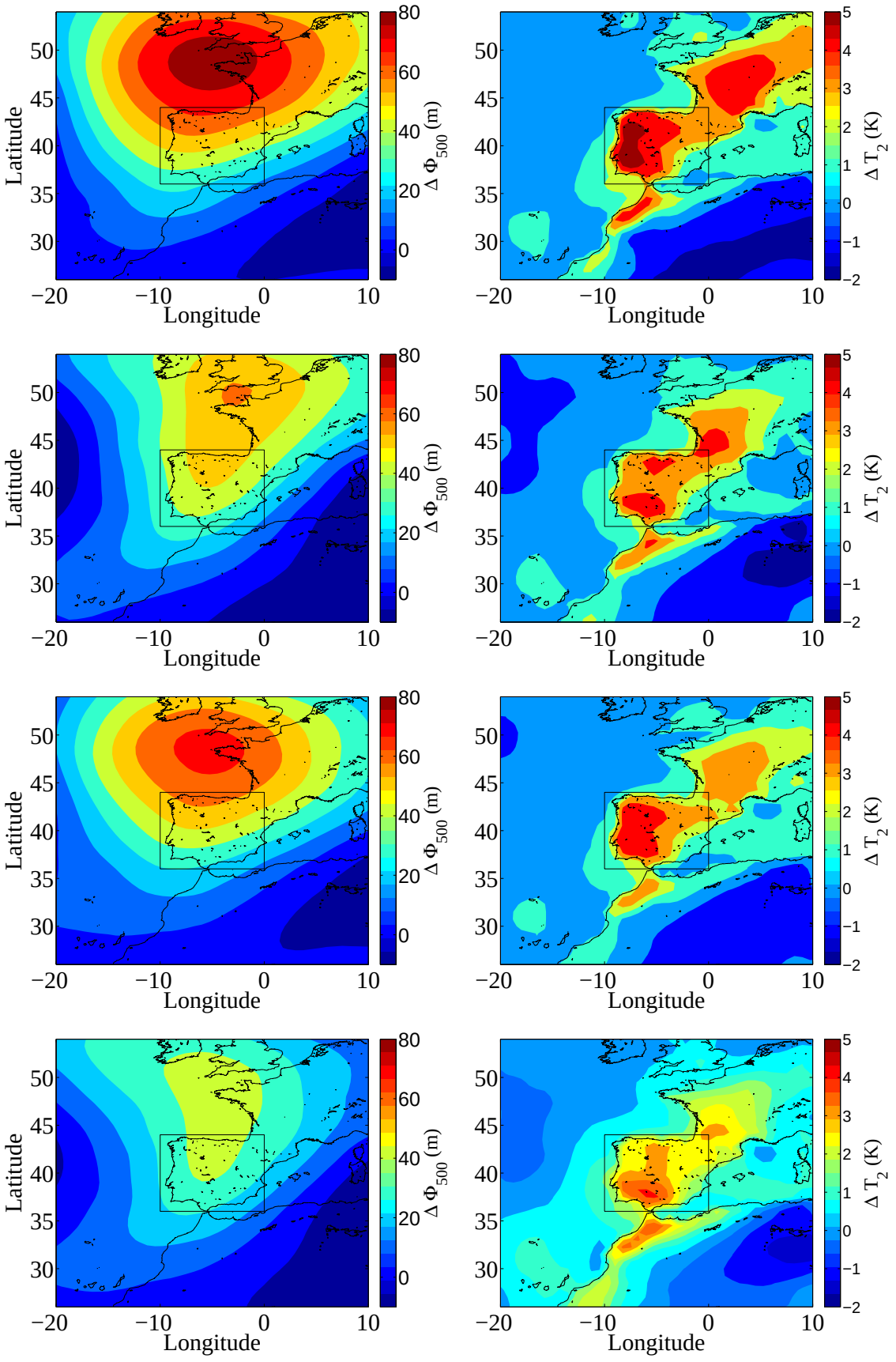

FIGURE 2.4: Composites over the Iberian Peninsula of the 500-hPa geopotential anomaly ($\Delta\Phi_{500}$) (left column) and the 2-m air temperature (ΔT_2) (right column) for BA diagnostic corresponding to HWM (first row from top) and WFM (second row from top) and for FRP diagnostic corresponding to HWM (third row from top) and WFM (fourth row from top).

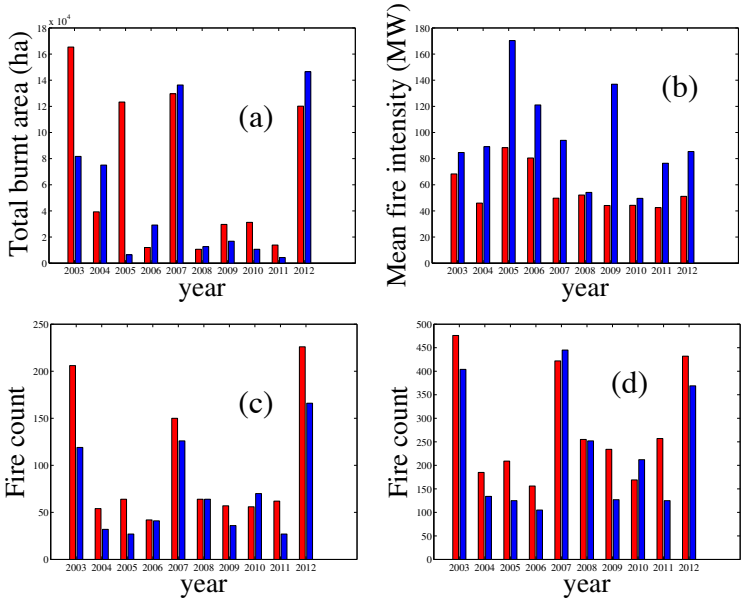

FIGURE 2.5: Total burnt area (a), fire intensity (b) and fire counts associated with BA (c) and FRP (d) detection for HWM (red) and WFM (blue).

duration). Figure 2.7 is similar to Fig. 2.6 the temperature anomaly. The sequence is very similar to that of the geopotential with a very fast build-up and disappearance in the WFM situation and a slightly longer anomaly in the HWM situation. The maximum temperature anomaly is found during the widlfire activity (between t_0 and $t_0 + \Delta t$). Student's T tests were performed on Figs. 2.6 & 2.7 to determine if the composites were different from the climatology and if composite maps from HWM and WFM were statistically different. We find that they are at the 99.9% confidence level. So despite the accidental or criminal nature of these wildfires, the correlation between the duration of the fire episode and of the synoptic favorable conditions is high and statistically significant.

Such finding is not specific to the Iberian Peninsula. Such behavior has been found in other sub-regions. To illustrate this point, Fig. 2.8 shows the time evolution of the wind speed at 10-meter and 500-hPa levels and the 2-meter air temperature anomaly for the whole Mediterranean region, based on the BA diagnostic (the results are similar with FRP and will not be shown for concision). We selected only wildfires which duration is longer than one day and shorter than ten days ($\approx 50\%$ of BA-detected wildfires and $\approx 20\%$ of FRP-detected wildfires). To compute a composite over the whole Mediterranean region, some normalization is needed. The normalized variables plotted in Fig. 2.8 are:

$$U_{500}^{\star} = \frac{\|U_{500}\|}{\overline{\|U_{500}\|}} \quad ; \quad U_{10}^{\star} = \frac{\|U_{10}\|}{\overline{\|U_{10}\|}} \quad ; \quad \Delta T_2^{\star} = \frac{\Delta T_2}{\overline{\Delta T_2}} \quad ; \quad t^{\star} = \frac{t - t_0}{\Delta t} \tag{2.1}$$

with $\overline{X} = mean(X)|_{t^{\star} \in [0\ 1]}$ and where U_{10}, U_{500} and ΔT_2 are the wind speed at 10-meter and 500-hPa levels and the 2-meter air temperature anomaly, respectively. So $t^{\star} = 0$ and $t^{\star} = 1$ are the starting and ending dates of the wildfire activity, respectively. Figure 2.8 shows the 99% confidence intervals

for $U^{\star}_{500}$ and $U^{\star}_{950}$ and the 90% confidence intervals for $\Delta T^{\star}_{2}$. As for Fig. 4.5 these confidence levels correspond to the maximum level of significance possible. They were determined using 5000 bootstrap resamplings. One can notice that $\Delta T^{\star}_{2}$ is positive well before and after the wildfire. HWM and WFM wildfires therefore happen during periods when the temperature is already anomalously high. Indeed, long periods of high temperatures in heatwaves in summer in the Mediterranean region are associated with droughts (Stéfanon et al., 2012b), which in turns tends to lower the fuel moisture content and kill some of the vegetation. Fire can therefore propagate more easily in these situations. The temperature anomaly increases very sharply at $t^{\star} = 0$ and gets back to its pre-fire value at $t^{\star} = 1$ for both HWM and WFM wildfires. Wildfire initiation and end "perfectly" match the duration of the heatwave episodes, characterized by extremely hot temperature anomalies. The mean value of Δt is 3.3 and 2.2 days for BA and FRP diagnostics, respectively, which are typical durations of mid-latitude weather regimes. As seen over the Iberian Peninsula, the surface temperature anomaly is strongly related to the 500-hPa geopotential height and thus the geostrophic wind speed at the 500-hPa pressure level ($\|U_{500}\|$). The 500-hPa air circulation slows down gradually, attains a minimum during the wildfire (roughly at the beginning) and this circulation accelerates back to its previous levels after the wildfire stops. The relative difference between the maximum and the minimum of the 500-hPa wind speed is slightly larger in HWM situation, indicating stronger deceleration. A similar evolution is found for the wind speed at the 10-meter level for the HWM wildfires. For WFM wildfires, the evolution is different. The wind speed at the 10-meter level does not evolve much with time. A weak decrease of the wind speed is visible during the wildfire activity followed by a weak increase but undoubtedly the blocking high associated to WFM wildfire is much weaker than for HWM wildfires.

2.4 Size of wildfires in the Euro-Mediterranean region

In Section 2.3 we saw that synoptic meteorology, in particular the presence of heatwaves and blocking highs, has a strong control over fire development. In this Section we will focus more deeply on the relationships between wind speed and fire size and develop a theoretical framework to analyze the two modes behavior seen in Fig. 2.3 for high temperature anomalies.

2.4.1 Burnt area observations: role of wind speed and heatwaves

Figure 2.9 is a modified version of Fig. 2.3 displaying only the fire size of extreme fires over EAST and MED. It shows the dependence of the 95^{th} quantile of burnt area (red) to the 10-meter wind speed for an anomaly of the 2-meter air temperature with respect to the climatology (1979–2012) (ΔT_2) smaller than 3°C and exceeding 3°C (heatwave). For consistency we also show the median (blue) and 75^{th} (green) quantiles. It can be noted that they do not show strong responses to the chosen meteorological parameters. We will therefore focus only on largest wildfires only. Large temperature anomalies are

generally associated with an anticyclonic anomaly, persisting heat waves (Barriopedro et al., 2011, Black et al., 2004, Cassou et al., 2005, Stéfanon et al., 2012b) and larger burnt area (Pereira et al., 2005). In the EAST domain, extreme wildfire size is nearly independent of the wind speed for $\Delta T_2 < 3\ K$ and slightly increases with wind speed for $\Delta T_2 > 3\ K$. In the MED domain, a totally different behavior is found. For $\Delta T_2 < 3\ K$, extreme wildfire burnt areas increase with wind speed, similarly to what is found in the EAST domain for larger temperature anomalies. For $\Delta T_2 > 3\ K$, a bimodal dependence is found. A large number of wildfires occur for low wind speed (i.e. weaker than 2 m s^{-1}) and for high wind speed (i.e. stronger than 4 m s^{-1}). The bimodal dependence of wildfire burnt areas to wind speed in the MED region for situations associated with heatwaves is counter-intuitive since the rate of spread is a growing function of wind speed (Rothermel, 1972). To understand these observations, a probabilistic cellular automaton model is adapted in Section 2.4.2 to include the impact of wind speed on fire propagation and derive the burnt area.

2.4.2 Burnt scar modelling

Fire propagation models are very diverse in terms of complexity. Among the simplest is the probabilistic cellular automaton (PCA), which relies on a stochastic fire propagation set by a probability of propagation which depends on wind speed and direction, terrain slope and vegetation state. Despite its simplicity, such model presents enough similarities with fire propagation dynamics to ensure accurate verification against observations and to allow in-depth analysis of fire propagation dynamics for a moderate computational cost (Alexandridis et al., 2008, Berjak and Hearne, 2002, Encinas et al., 2007a,b, Trunfio, 2004). Unlike coupled fire-atmosphere models such as FIRETEC (Linn et al., 2002), the PCA model does not rely on physical processes that govern the fire behavior. However its simple implementation allows easier theoretical analysis.

The PCA implements a grid of cells that can be in a finite number of states and a local rule that determines the probability of transition between states at each time step. In our case we use the most elementary form of PCA for fire simulation, taking into account only the effect of wind speed on fire spread. The grid is a regular square lattice of cells and we choose 3 different states for the cells.

- State 0 corresponds to an non-burnt cell;
- State 1 corresponds to the situation of a burning cell. The cells in this state can propagate the fire;
- State 2 corresponds to the situation of an already burnt cell.

The probability that a cell in state 1 can spread the fire to its neighbors is defined by Eq. (2.2):

$$p = min\left(\gamma p_0 f\left(V, \theta\right), 1\right) \tag{2.2}$$

with V the surface wind speed, θ the angle between the direction of propagation and the wind and γ a corrective factor for diagonal spread. The quantity p_0 is a constant and is the spreading probability in absence of wind. The function f of wind is defined in Alexandridis et al. (2008) as:

$$f(V,\theta) = \exp\left[V\left(c_1 + c_2(\cos\theta - 1)\right)\right] \tag{2.3}$$

The quantities c_1 and c_2 are empirical factors set respectively to 0.045 s m^{-1} and 0.131 s m^{-1} (Alexandridis et al., 2008). The shape of $f(V,\theta)$ is shown in Fig. 2.10 for various values of wind speed. Function f is isotropic with zero wind and gradually expands in the direction of the wind. The corrective factor γ is set at $\frac{1}{\sqrt{2}}$ such as the fire propagation is isotropic in absence of wind speed. Without such correcting factor the fire would take a square form in the absence of wind.

For details of the implementation of the PCA in MATLAB/C++, see Appendix A.

2.4.3 Burnt area simulations: parallel between the percolation threshold and the wildfire size

Figure 2.11 shows the fraction of burnt cells y_2^{final} - with y_i the fraction of cells in state i in the PCA grid - as a function of p_0 when the fire is extinct in a grid constituted of 101×101 cells. The quantity y_2^{final} is computed from a Monte Carlo simulation. Figure 2.11 displays a transition at $p_0 \sim 0.3$ between a mode where very few cells are burnt ($y_2^{final} \sim 0$) and another one where the fire spreads to nearly all the grid ($y_2^{final} \sim 0.9$).

This phenomenon of infinite spread of the fire in the PCA is called percolation and the limit in terms of propagation probability above which percolation can occur is called the percolation threshold.

2.4.4 Percolation threshold analysis

Above a certain value of the propagation probability p the fire can thus propagate indefinitely in the PCA. The critical value p_0^{crit} of the p_0 constant is shown in Fig. 2.11 for the zero wind case. This phenomenon is called percolation and can be analyzed theoretically. (Pak and Hayakawa, 2011) studied the percolation threshold for an elementary form of PCA, with no diagonal propagation or wind speed effect. They state with the help of a mean-field approximation that the fraction of cells in states 1 and 2 are governed by Eqs. (2.4), (2.5) and (2.6).

$$\frac{dy_1}{dt} = 4py_1y_0 - a_{12}y_1 \tag{2.4}$$

$$\frac{dy_2}{dt} = a_{12}y_1 \tag{2.5}$$

$$y_0 + y_1 + y_2 = 1 \tag{2.6}$$

with y_i the fraction of cells in state i in the PCA grid, p the probability of fire spread and a_{12} the probability that a cell in state 1 at time t goes to state 2 at time $t+1$. In our case, the quantity a_{12} is set to 1. In this Section, we adapt the PCA model to account for wind speed effect and diagonal propagation. Equation (2.4) is thus modified as follows:

$$\frac{dy_1}{dt} = C(V)p_0 y_1 y_0 - y_1 \tag{2.7}$$

with $C(V)$ a weighting coefficient which allows to account for fire spreading in various directions as a function of the wind speed. It writes:

$$\begin{aligned} C(V) \quad = \quad & \exp(Vc_1) + 2\exp[V(c_1 - c_2)] + \exp[V(c_1 - 2c_2)] \\ & + 2\gamma\exp\left\{V\left[c_1 + c_2\left(\tfrac{\sqrt{2}}{2} - 1\right)\right]\right\} \\ & + 2\gamma\exp\left\{V\left[c_1 - c_2\left(\tfrac{\sqrt{2}}{2} + 1\right)\right]\right\} \end{aligned} \tag{2.8}$$

The first term of the sum on the right-hand-side of Eq. (2.8) corresponds to a propagation along the wind direction, the second term to a propagation across the wind direction and the third to a propagation against the wind. The other terms correspond to diagonal propagation ($\sqrt{2}/2$ corresponds to $\cos(\pi/4)$). The details of the derivation of Eq. (2.8) is provided in Appendix B. Equation (2.8) can be simplified:

$$\begin{aligned} C(V) \quad = \quad & \exp(Vc_1) \times \Big\{[1 + \exp(-Vc_2)]^2 + \\ & \sqrt{2}\left(\exp\left[Vc_2\left(\tfrac{\sqrt{2}}{2} - 1\right)\right] + \exp\left[-Vc_2\left(\tfrac{\sqrt{2}}{2} + 1\right)\right]\right)\Big\} \end{aligned} \tag{2.9}$$

Following the methodology of Pak and Hayakawa (2011), we derive a relationship between p_0^{crit} and the wind speed-dependent coefficient $C(V)$:

$$p_0^{crit} = \frac{1.51552}{C(V)} \tag{2.10}$$

The value of the numerator comes from site percolation theory. For further insight, Pak and Hayakawa (2011) give an introduction to bond and site percolation theory. This equation is plotted in Fig. 2.12, along with the numerically derived p_0^{crit}. To compute this quantity numerically we consider that percolation occurs when a fire initiated in the middle of our 101×101 PCA grid, reaches the edges of the domain. The p_0 value increases from 0.2 with 0.001 increments. The critical value $p_0 = p_0^{crit}$ is set when more than 90% of a 300 simulation ensemble percolate. We can see that both the theoretical and computed values p_0^{crit} increase with wind speed for low wind values, reach a maximum and then decrease with wind speed. The difference between the theoretical and computed curves is methodology of derivation of p_0^{crit}. The shape of this curve will be essential in the analysis of our observations in Section 2.4.1. In the following, we refer to $p_{0,0}^{crit}$ as the value in the absence of wind and $p_{0,max}^{crit}$ as the maximum value reached by p_0^{crit}.

2.4.5 Discussion

The PCA gives us a theoretical framework to understand the results of Fig. 2.9. The mean fire size of the biggest wildfires (above the 95^{th} quantile) is a growing function of wind speed in most cases, excepted in the Mediterranean Basin for large temperature anomalies. It is also dependent of the slope of the local topography but this has no consequence on the observed behavior of the burnt area. A proposed expression of p_0 is described in Alexandridis et al. (2008):

$$p_0 = p_h(1+p_{den})(1+p_{veg})p_s(\theta_s) \tag{2.11}$$

where p_h is a constant used for homogeneous fuel beds, p_{den} and p_{veg} are factors depending on vegetation density and type, respectively. The quantity θ_s is the local slope in degrees and the expression of $p_s(\theta_s)$ is given by:

$$p_s(\theta_s) = \exp(a\theta_s) \tag{2.12}$$

This formulation is very simple and other factors such as fuel moisture could be taken into account for more realistic simulations. We do not consider the effect of slope in this study. It may be a differentiating factor between EAST and MED, which could lead to quantitative differences between fire sizes in the two regions but for a given region the slope value is the same whatever the wind speed, vegetation state or temperature and soil moisture anomaly. The main cause for such behavioral differences is the value of p_0 relative to p_0^{crit}. The final burnt area can vary drastically because of percolation as seen in Fig. 2.11. Figure 2.13 displays the fraction of burnt cells (normalized to its value after 50 time steps in the absence of wind speed and for $p = 1$, see Fig. 2.13) as a function of wind speed for 3 different values of p_0. Three p_0 values are chosen in the 3 different domains : $p_{0,1}$ set at 0.26, below the 0 wind percolation threshold, $p_{0,2} = 0.3$ between $p_{0,0}^{crit}$ and $p_{0,max}^{crit}$ and $p_{0,3} = 0.35$ above the maximum of the percolation threshold. (Fig. 2.12 & Fig. 2.13). The saturation for strong winds visible is due to the fact that $p = 1$ in the direction of the wind so has always the same shape after 50 time steps and the fraction of burnt cells saturates. For p_0 values smaller than $p_{0,0}^{crit}$, percolation is only possible for high winds so the burnt area increases with wind speed similarly to what is observed over the EAST domain and over the MED domain for low temperature anomaly ($\Delta T_2 < 3°$C). For intermediate p_0 values ranging between $p_{0,0}^{crit}$ and $p_{0,max}^{crit}$, large burnt area are simulated for low wind values (smaller than about 5 m s^{-1}) and large wind speed values (larger than about 15 m s^{-1}) (Fig. 2.13). Conversely, smaller burnt area are simulated for intermediate wind ranging between 5 and 15 m s^{-1} (Fig. 2.13). For p_0 values larger than $p_{0,max}^{crit}$, similar qualitative results are obtained with however larger burnt area.

We can therefore analyze Fig. 2.9 as if each subfigure corresponds to a different value of p_0. The value of p_0 corresponding to the EAST domain and MED domain for low temperature anomaly should be lower than $p_{0,0}^{crit}$, so that the burnt area increases with wind speed. The rate of burnt area increase with respect to wind speed is a function of the departure of p_0 from $p_{0,0}^{crit}$. Over the EAST domain, the value of p_0 is expected to be farther below $p_{0,0}^{crit}$ than over the MED domain. It may also explain why a change

of propagation regime is observed over the MED domain when shifting from low to high temperature anomalies. Indeed, for large temperature anomalies corresponding to severe heatwaves ($\Delta T_2 > 3°C$) over the MED domain, a value of p_0 exceeding $p_{0,0}^{crit}$ is expected. A simple way to understand such behavior is to consider the probability of extinction of a fire occupying one cell. Let p be the spread probability. The cell has 8 neighbors on a square grid. In the absence of wind, the extinction probability is $(1-p)^8$. When wind blows, the fire spreads in the direction of the wind and diagonally. The probability of extinction becomes $(1-p)^3$. Let us consider very weak wind speed values for which isotropic spreading can be assumed and p increases with wind speed. Then the extinction probability $(1-p)^8$ drops very quickly. When isotropic spreading does not stand anymore, then the probability of extinction transitions to $(1-p)^3$ and increases as 3 is a lower exponent than for the isotropic spreading. With increasing wind speed, the probability of extinction decreases again. So instead of enhancing wildfire propagation, moderate winds produce smaller wildfires by cutting off the propagation against the wind. Such analysis explains the 2 modes observed in the MODIS and EFFIS data over the MED domain.

The function of wind $f(V,\theta)$ in the calculation of p is critical in the explanation of the observed behavior [see Eq. (2.10)]. The choice of this function by Alexandridis et al. (2008) was done empirically to match with the behavior of the rate of spread of real wildfires as a function of the wind and the angle between the wind direction and the direction of propagation. Its shape is coherent with real wildfire propagation but concerns can be raised (Fig. 4.3). The backpropagation is very small and the overall shape is non-elliptical. This last point could be due to the indirect impact of factors that alter the normally elliptical shape of small wildfires, such as the small variations in wind direction that make the wildfire slightly conical. Despite such concerns, this function has been efficient in the simulation with PCA of the 1990 burnt scar in the Spetses island in Greece (Alexandridis et al., 2008) and thus does fairly well for burnt scar modeling purposes.

Another concern is that the propagation speed in the direction of the wind tends to grow very quickly with the wind speed. With the expression of $f(V,\theta)$ used in this study, the propagation speed only becomes very high when the wind speed exceeds 15 m s^{-1} which is much too high compared to observed wildfires. Tests have been performed by using other expressions of $f(V,\theta)$, such as the elliptical form and varying the c_1 and c_2 coefficients of Eq. (2.3), and no qualitative difference in the behavior of p_0^{crit} has been evidenced (not shown). In detail, the choice of c_1 and c_2 coefficients can be questioned, as it was only validated on one case study. A key issue is to know if $p_{0,max}^{crit}$ is reached for a positive value of the wind speed, which conditions the existence of the "2 modes" regime. Figure 2.14 shows the value of the ratio $\left(p_{0,max}^{crit} - p_{0,0}^{crit}\right)/p_{0,0}^{crit}$ as a function of c_1 and c_2 calculated from Eq. (2.10). For a value of c_2 larger than about $1.25c_1$ this property is verified. This condition can be interpreted as the backpropagation of the wildfire being impaired in a sufficiently large angle domain by the wind.

A possible reason for the burnt area to decrease with wind speed for moderate wind speed over the MED domain is that in order to reach a p_0 value larger than $p_{0,0}^{crit}$, higher flammability of the fuel bed or a more fire-prone environment are needed. This could be caused by the lower precipitation amounts in the

MED region, which would lead to lower fuel moisture. This could also be due to different vegetation type between the EAST and MED regions.

Our analysis reveals the critical role of the percolation threshold in wildfire propagation. Here we focused our work on the dependency between burnt area and wind speed but other studies found threshold behaviors related to other explanatory variables such as the Drought Code of the Canadian Fire Weather Index (Loepfe et al., 2014) and fire season aridity (Pausas and Paula, 2012). These variables relating to fuel moisture, it could be possible a similar percolation threshold behavior with a PCA incorporating a propagation probability decreasing with fuel moisture.

2.5 Conclusions

This chapter shows that in the Mediterranean large wildfires are associated with a blocking situation as already reported in the literature (Pereira et al., 2005). In detail, the intensity of the blocking defines two types of wildfires. Fast build-up of a weak blocking produces intense wildfires associated with strong winds which allow propagation over long distances. Statistically, these wildfires, referred as wind forced mode (WFM) wildfires in this study, are shorter than those occurring in the absence of strong winds, called heatwave mode (HWM) wildfires in this study. The HWM wildfires are associated to a stronger blocking high which build-up extends over a slightly longer time period, which eventually end-up with burnt area similar to those cause by WFM wildifres. This study also goes one step further with respect to the determination of the favorable synoptic conditions associated with the Mediterranean wildfires. Indeed, this study shows a near perfect match between the period of wildfire activity and the persistence of the favorable synoptic conditions. In other words, statistically, the wildfire activity starts at the onset of the blocking situation which intensity controls the type of wildfire (HWM or WFM) and ends with the transition to less favorable synoptic weather pattern. So despite the accidental and criminal nature of the wildfires in the Mediterranean, there is an extremely strong control of the concomitant weather on the wildfire, whether it be on its extension or intensity. Such result is very promising regarding fire risk forecast and management in the Mediterranean region.

The behavior of the burnt area with temperature anomaly and wind speed was analyzed with the help of MODIS observations and ERA-Interim reanalysis. In the EAST region and in MED for low temperature anomalies, the burnt area is a growing function of wind, which is rather intuitive. For large temperature anomalies in the MED region, corresponding to severe heatwaves, the burnt area behaves differently. It displays a ”2 modes” shape with a minimum value of burnt area for medium values of the wind speed. The possible cause of such counter-intuitive behavior has been investigated theoretically by means of probabilistic cellular automata (PCA). It was found that when the wind speed is moderate, the backpropagation is impaired when the forward propagation is not sufficiently fast to compensate the loss in burnt area. Therefore if the wind is not strong enough to make the propagation along the wind direction ”sure enough”, percolation does not happens in the PCA resulting in smaller wildfires. The

percolation threshold is never reached in the EAST region. It is only exceeded for very low or high wind speeds in the MED region. Such shift between 2 regimes of propagation may be caused by the favorable occurrence of severe heatwaves in the MED region.

A natural follow-up would be to model the impact of fuel moisture on the propagation probability by adapting the known variations of the rate of spread of the fire with this quantity (Sharples 2008). It could be complemented by a thorough analysis of the behavior of dead and live fuel moisture in Mediterranean ecosystems with respect to air temperature anomaly and the incorporation of such relation in the expression of the probability of fire propagation. However, fuel moisture is a quantity which is hard to assess. Live fuel moisture depends on the plant species and dead fuel moisture on the size of the fuel particle. For a more holistic approach, a more realistic fire propagation modelling framework such as FIRETEC would be needed to better identify and quantify the processes driving fire propagation. Finally, conducting observational studies on other hotspots of wildfire activity (e.g. Australia, USA) in order to see whether the 2 modes exists in other parts of the world would be of interest.

This chapter helped us discover the critical role of wind speed and temperature anomaly in the short-term meteorological driving of fire size and intensity. In doing so we completed the first research objective. In the next chapter, using these results, we will develop a methodology to retrieve the conditional distribution of fire size and intensity with respect to weather.

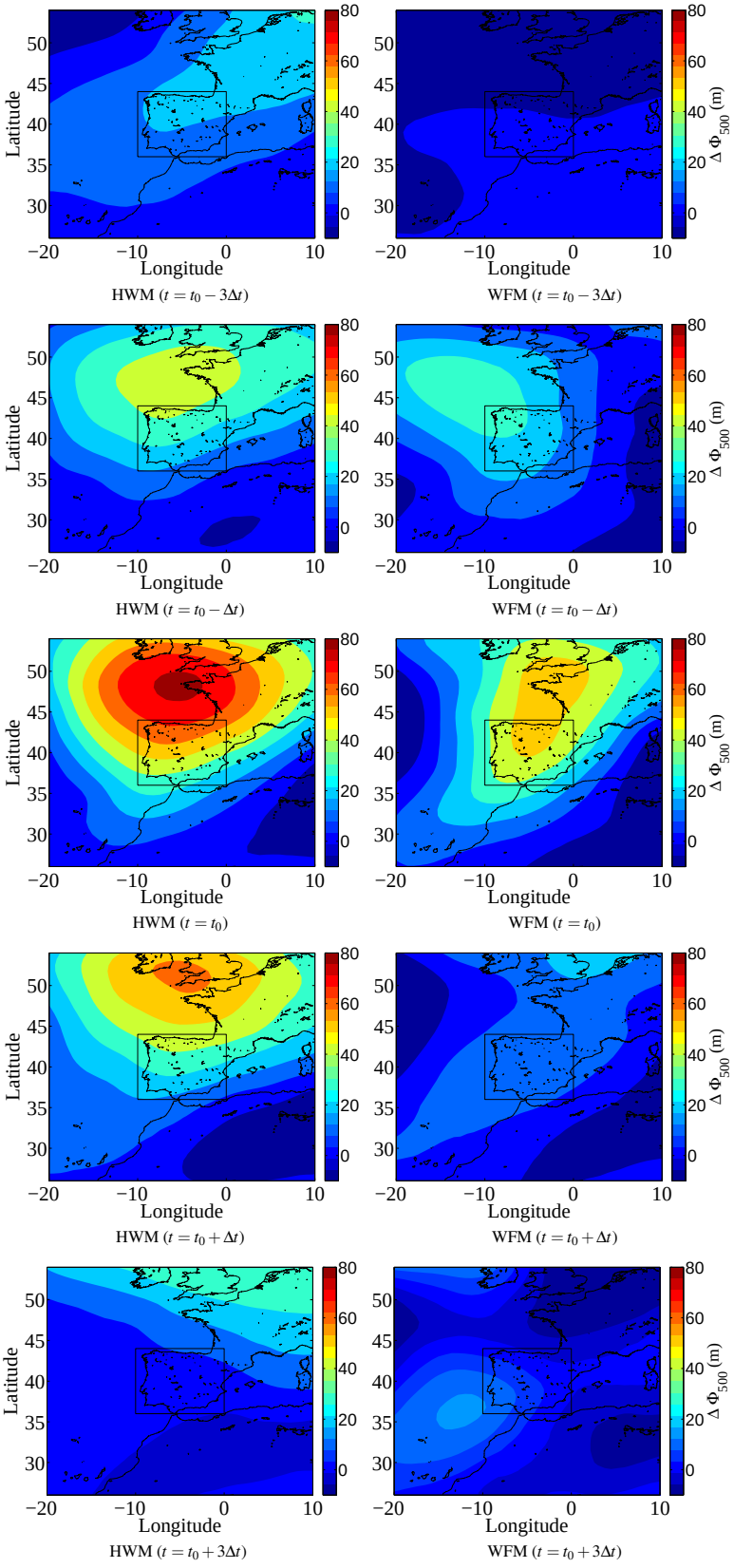

FIGURE 2.6: Composites over the Iberian Peninsula of the 500-hPa geopotential anomaly ($\Delta\Phi_{500}$) for HWM (left column) and WFM (right column) wildfires at time $t_0 - 3\Delta t$ (first row from top), $t_0 - \Delta t$ (second row from top), t_0 (third row from top), $t_0 + \Delta t$ (fourth row from top) and $t_0 + 3\Delta t$ (fifth row from top). The composites are computed using the BA diagnostic.

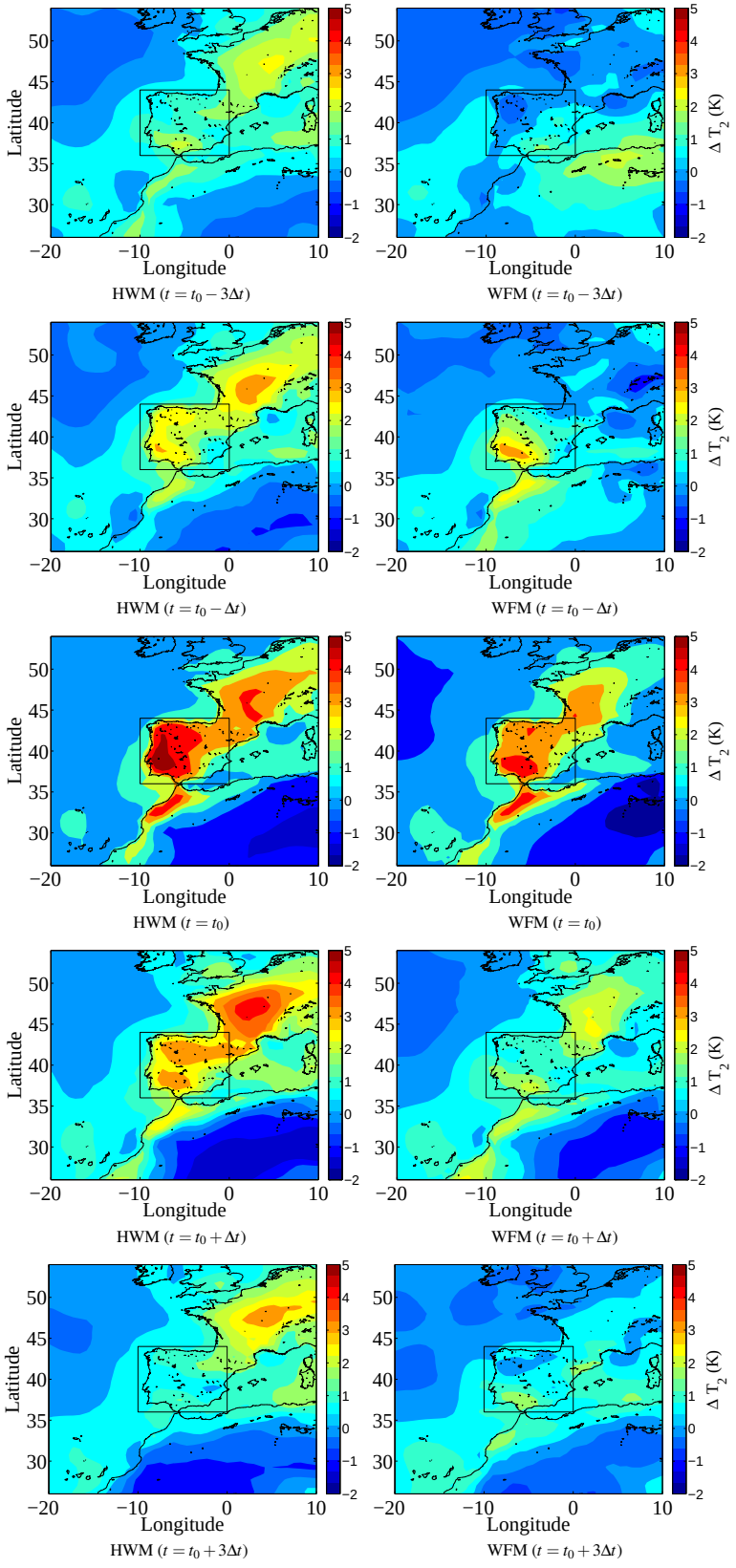

FIGURE 2.7: Same as Fig. 2.6 for the 2-meter air temperature anomaly (ΔT_2).

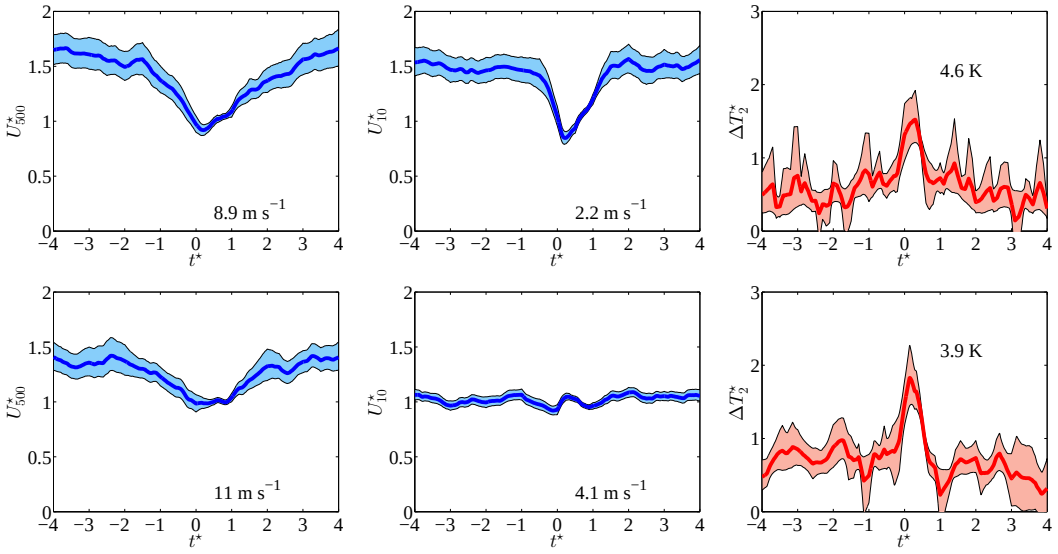

FIGURE 2.8: Composite of the time evolution of the wind speed at 500-hPa and 10-meter levels and the 2-meter air temperature anomaly for the whole Mediterranean region, based on the BA diagnostic for the HWM (upper row) and WFM (lower row) wildfires. The plotted values are normalized according to Eq. (2.1). Normalized time $t^\star = 0$ and $t^\star = 1$ correspond to the starting and ending dates of the wildfire activity, respectively. The value of $\overline{\|U_{500}\|}$, $\overline{\Delta T_2}$ and $\overline{\|U_{10}\|}$ are indicated in each sub-panel. Blue figures are plotted with their 99% confidence intervals and red figures with their 90% confidence intervals.

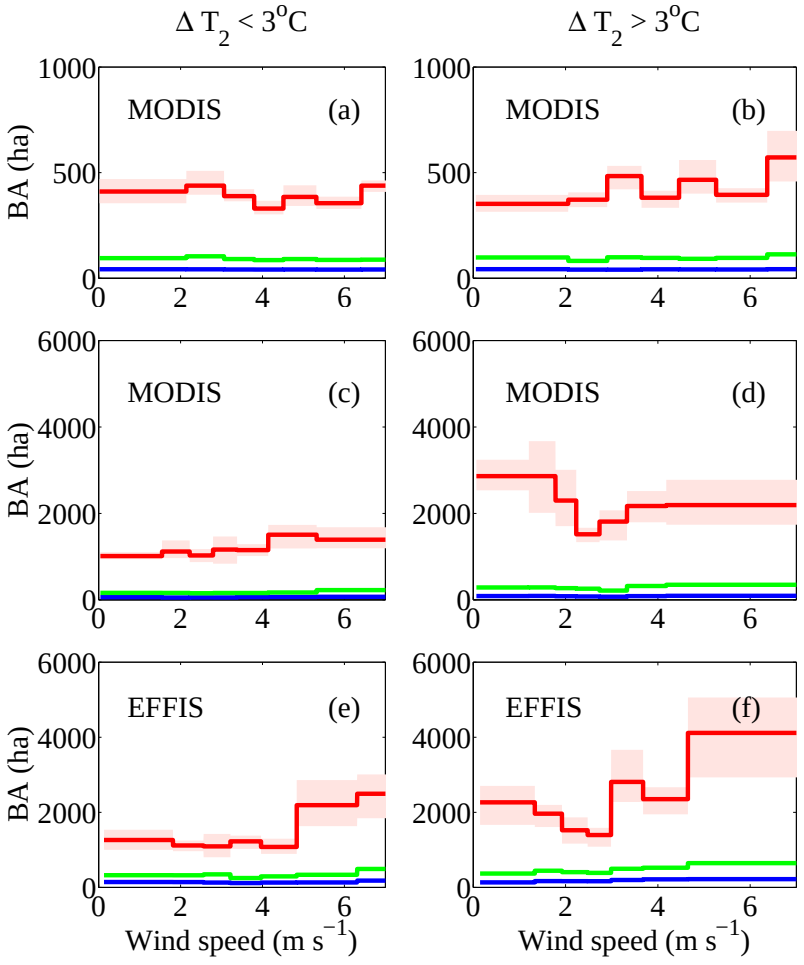

FIGURE 2.9: Wildfire burnt areas (BA) (i.e. 50^{th} (blue), 75^{th} (green) and 95^{th} (red) quantiles of the local probability density function) as a function of 10-m wind speed for the EAST (top row) and MED domains (middle and bottom row) for $\Delta T_2 < 3°C$ (left column) and $\Delta T_2 > 3°C$ (right column). The pink shaded area shows the 70% confidence intervals for the 95^{th} quantile. For the MED region we display the quantiles derived with the MODIS (middle row) and EFFIS (bottom row) data sets.

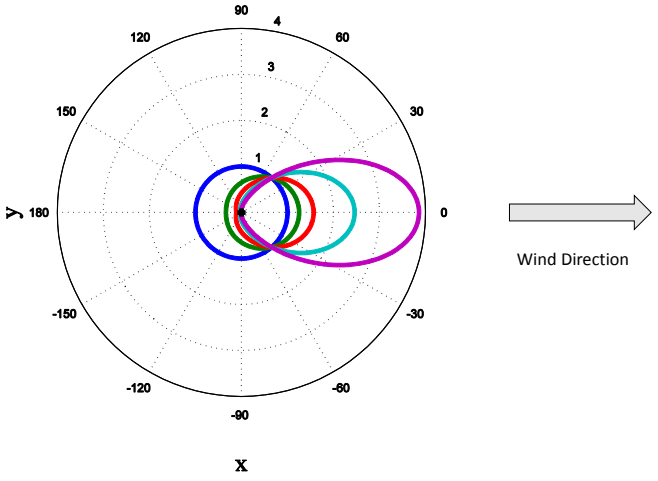

FIGURE 2.10: Polar plot of the function $f(V,\theta)$ for values of wind speed V equal to 0 (blue), 5 (green), 10 (red), 20 (cyan) and 30 m s^{-1} (purple). The f function expresses the dependency of the local fire propagation probability to wind speed and angle of propagation. Here the wind follows the x-axis direction.

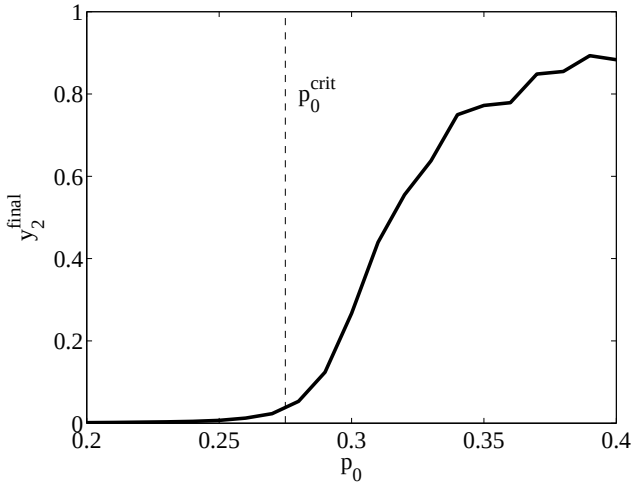

FIGURE 2.11: Evolution of the fraction of burnt cells y_2^{final} with y_2 the fraction of cells in state burnt in the PCA grid as a function of p_0 when the fire is extinct in a grid constituted of 101×101 cells. The simulation is performed in the absence of wind. The quantity p_0 is the constant part of the local fire propagation probability, which can be seen as a proxy of fuel density, type and moisture. The quantity p_0^{crit} is the percolation (infinite propagation in the PCA) threshold.

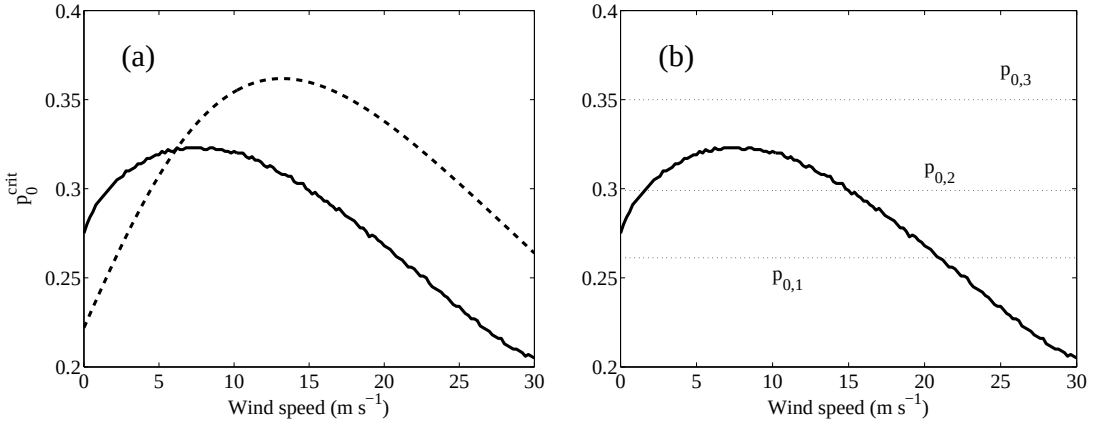

FIGURE 2.12: p_0^{crit} the percolation (infinite propagation in the PCA) threshold as a function of wind. Dashed curve is the theoretical value found using mean-field approximation and the full curve is the numerically derived value. Dotted lines ($p_{0,1}$), ($p_{0,2}$) and ($p_{0,3}$) correspond to the curves plotted in Fig. 2.13.

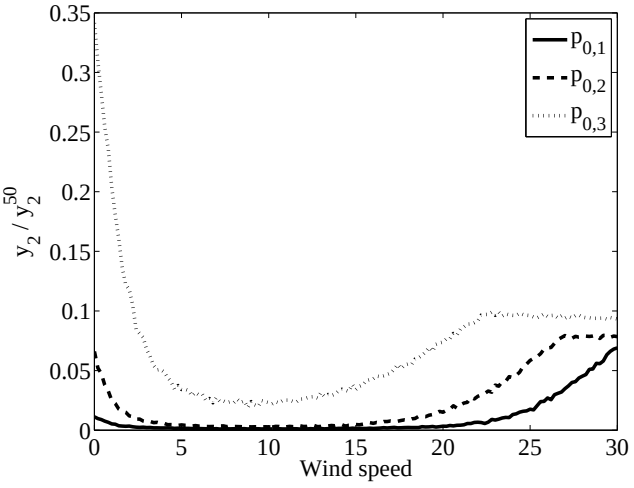

FIGURE 2.13: Fraction of burnt cells y_2/y_2^{50} (normalized to its value after 50 time steps in the absence of wind speed and for $p = 1$) as a function of wind speed for p_0 values set at $p_{0,1} = 0.26$ (solid line), $p_{0,2} = 0.3$ (dashed line) and $p_{0,3} = 0.35$ (dotted line) in Fig. 2.12.

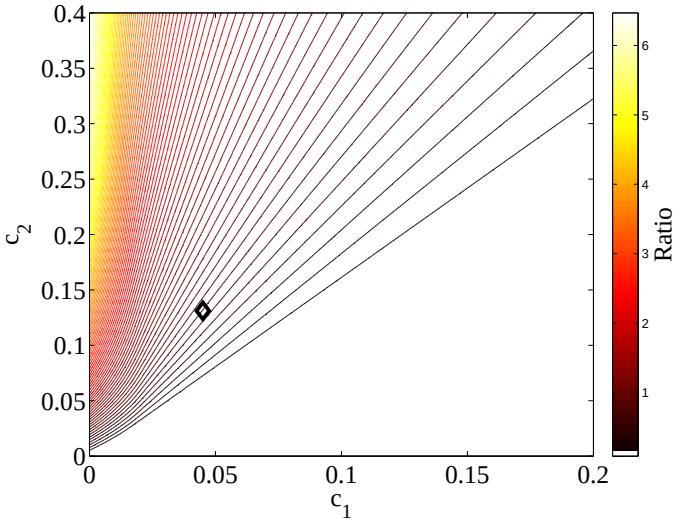

FIGURE 2.14: Ratio $\left(p_{0,max}^{crit} - p_{0,0}^{crit}\right) / p_{0,0}^{crit}$ for different values of the c_1 and c_2 parameters governing the function of local fire propagation probability. $p_{0,max}^{crit}$ is the maximum of the percolation threshold for increasing wind speeds and $p_{0,0}^{crit}$ is its value for 0 wind. The black diamond shows the (c_1, c_2) pair chosen by Alexandridis et al. (2008). A strictly positive value indicates that p_0^{crit} has a maximum value for a non-zero wind speed, which ensures that the burnt area has a local minimum for moderate values of wind speed.

Chapter 3

Statistical estimation of fire size and intensity distributions

This chapter stems from the collaboration with Mrs. Christine Keribin from the Laboratoire de Mathmatiques of the Orsay University. The findings shown hereafter are published as a scientific article in Natural Hazards and Earth System Sciences (Hernandez et al., 2015d).

In this chapter we investigate the use of statistical methods for wildfire risk assessment in the Mediterranean Basin using three meteorological covariates, the 2-meter temperature anomaly, the 10-meter wind speed and the January-June rainfall occurrence anomaly. We focus on two remotely-sensed characteristic fire variables, the burnt area (BA) and the fire radiative power (FRP), which are good proxies for fire size and intensity respectively. Using the fire data we determine an adequate parametric distribution function which fits best the logarithm of BA and FRP. We reconstruct the conditional density function of both variables with respect to the chosen meteorological covariates. These conditional density functions for the size and intensity of a single event give information on fire risk and can be used for the estimation of conditional probabilities of exceeding certain thresholds. By analyzing these probabilities we find two fire risk regimes different from each other at the 90% confidence level: a background summer fire risk regime and an extreme additional fire risk regime, which corresponds to higher probability of occurrence of larger fire size or intensity associated with specific weather conditions. Such a statistical approach may be the ground for a future fire risk alert system.

3.1 Context and introduction

In order to better manage fire risk, several methods have been investigated. Among the first are the fire risk indices, such as the Canadian Fire Weather Index (Van Wagner et al., 1985, 1987, 1974). This index relates to the expected intensity of the fire line, expressed in energy output rate per unit length of fire front. It is currently used as a fire risk indicator by the European Forest Fire Information System (EFFIS) of the Joint Research Center (JRC) of the European Commission. The Haines Index (Haines et al., 1983) is another indicator of dangerous fire development that focuses of atmospheric stability. It can be used in conjunction with the Canadian Fire Weather Index but is deemed less informative. These indices are empirically calibrated for predicting whether the atmospheric and hydrological conditions are prone to fire development. However one of their main drawback is that they lack temporal contrast: they identify correctly fire-prone seasons but fail to provide short-term variability in fire risk (e.g., San-Miguel-Ayanz et al., 2013, Figs. 7 , 8, 12 & 15). Other approaches exist, based on different criteria of fire risk. Using probabilistic cellular automata fire propagation models, simulations of multiple starting points can lead to risk maps than can be helpful for fire suppression forces deployment (Russo et al., 2014). The main weak point of this method is the lack of strong validation for the calibration of the propagation model. More in-depth simulations, using fully physical models such as FIRETEC (Linn et al., 2002), can provide accurate predictions of the propagation of a fire. This method can be very demanding computation-wise and requires a precise knowledge of the initial and boundary conditions. Using a probabilistic framework, a preliminary risk assessment study was conducted (Preisler et al., 2004). The aim of the study was to reconstruct the probabilities of fire occurrence and large fire propagation using meteorological and geographical covariates. The results, although encouraging, gave only mitigated quality in the estimation of monthly fire occurrence. Modeling accumulated seasonal burnt area time series using meteorological predictors gave satisfying results, with adjusted R^2 of 68% for the July-August time period and north-western region of Iberia (Sousa et al., 2015).

Besides fire size or fire occurrence, another important factor of risk regarding wildfires is the intensity of the fire front. The propagation of particularly intense wildfires is indeed very hard to control and can trigger very severe pollution episodes. However large data sets do not exist for this quantity, so we focus instead on the fire radiative power (FRP), a remotely-sensed variable strongly linked with the fire intensity.

The general framework of this study is the estimation of fire size and intensity of individual fires in the Mediterranean Basin using parametric statistical methods. Several studies focusing on the estimation of fire size exist, proposing to derive this quantity based on meteorological and geographical covariates. Their authors mainly use statistical learning techniques in order to give a quantitative or qualitative insight on fire size (Alonso-Betanzos et al., 2003, Cortez and Morais, 2007, Sakr et al., 2011). In some cases this analysis is extrapolated to future weather in the context of climate change (Amatulli et al., 2013). However one can reproach to these studies their lack of performance. An examination of Cortez and Morais (2007) lead to the observation that the estimation of fire size done by the best tested method

was only very marginally better than the mean of the observations. For fire intensity no studies of this kind were conducted.
Our approach will be to provide parametric estimations of both single-event fire size and intensity distribution functions conditionally to weather covariates. We take a multi-time-scale approach for the choice of our weather covariates, with seasonal and immediate weather information. Using these conditional distribution estimations we can then compute probabilities that a given fire grows particularly large or becomes very intense. Because of our methodology, these probabilities would be both sensitive to seasonal trends and immediate weather. These estimations would be much more informative than a conditional mean of fire size of intensity with respect to weather.
In Section 2.2 we describe the data we use. After presenting our fire variables, we show our weather covariates and explain their relevance. In Section 3.2 we find an adequate parametric distribution to model fire size and intensity of individual events. Using this result, we develop in Section 3.3 a methodology of fire risk assessment that focuses on the use of probabilities of large/intense wildfires.

Our weather database was built upon the ERA-Interim reanalysis of the European Center for Medium-range Weather Forecast (ECMWF) (Dee et al., 2011). The horizontal resolution of the reanalysis does not allow the derivation of the small-scale weather conditions in the immediate vicinity of the fire. To link the weather data to the fire data, we take the ERA-Interim grid point nearest from the detected fire event. We then associate to this event the weather recorded at 1200UTC the day of first detection.
We extract the following meteorological covariates:

- ΔT_2 (in K): the 2-meter air temperature anomaly, the difference between the 1200UTC 2-meter air temperature and its climatological daily mean;
- WS_{10} (in ms^{-1}): the 10-meter wind speed;
- ΔN_{precip} (in days): the anomaly with respect to the climatology of the number of days when precipitations $\geq$ 0.5 mm occur during the January-June time period preceding of the year of the fire.

ΔN_{precip} is mostly impacted by spring drought occurrence but positive winter precipitation anomaly has also been linked to the 2003 Portugal megafire event (Trigo et al., 2006). However, as shown in Vautard et al. (2007) and Stéfanon et al. (2012a), anomalies of precipitation during spring are favorable to summer heatwave conditions. Stéfanon et al. (2012b) also shown that deficit of precipitation during spring, can trigger early vegetation growth, providing abundant fire fuels in summer. Positive winter precipitation anomalies may amplify this mechanism.
Our choice of covariates was done to retain a broad range of time-scales. We go from the hourly to daily time-scales (ΔT_2, WS_{10}) to seasonal time-scales (ΔN_{precip}). We also settled on covariates with proven impact on wildfire activity. Wind speed accelerates the propagation of the fire (Rothermel, 1972) in the direction of the wind and blocks backpropagation. The temperature anomaly ΔT_2 is an indicator

of heatwave occurrence. Pereira et al. (2005) showed that in Portugal wildfires often co-occurred with synoptic blockings and heatwaves. In Sardinia, Cardil et al. (2014) showed that large fire occurrence, daily burnt area and daily number of fires were higher on high temperature days. Hernandez et al. (2015a) and Hernandez et al. (2015c) further this work by showing that heatwaves and surface wind control wildfire size and duration strongly. Dimitrakopoulos et al. (2011) emphasized the link between drought and wildfire activity (wildfire occurrence and area burnt) in Greece. We chose ΔN_{precip} as indicator of drought occurrence preceding the wildfire. Low values of ΔN_{precip} indicate both low precipitation amount and low overall cloudiness in the January-June time period. Intuitively, we could say that more arid preceding seasons could lead to lower values of soil and fuel moisture during summer. Zampieri et al. (2009) showed that this quantity is linked to drought occurrence in summer. Additionally Vautard et al. (2007) and Stéfanon et al. (2012b) showed that summer heatwave occurrences were also impacted by rainfall deficit in previous months.

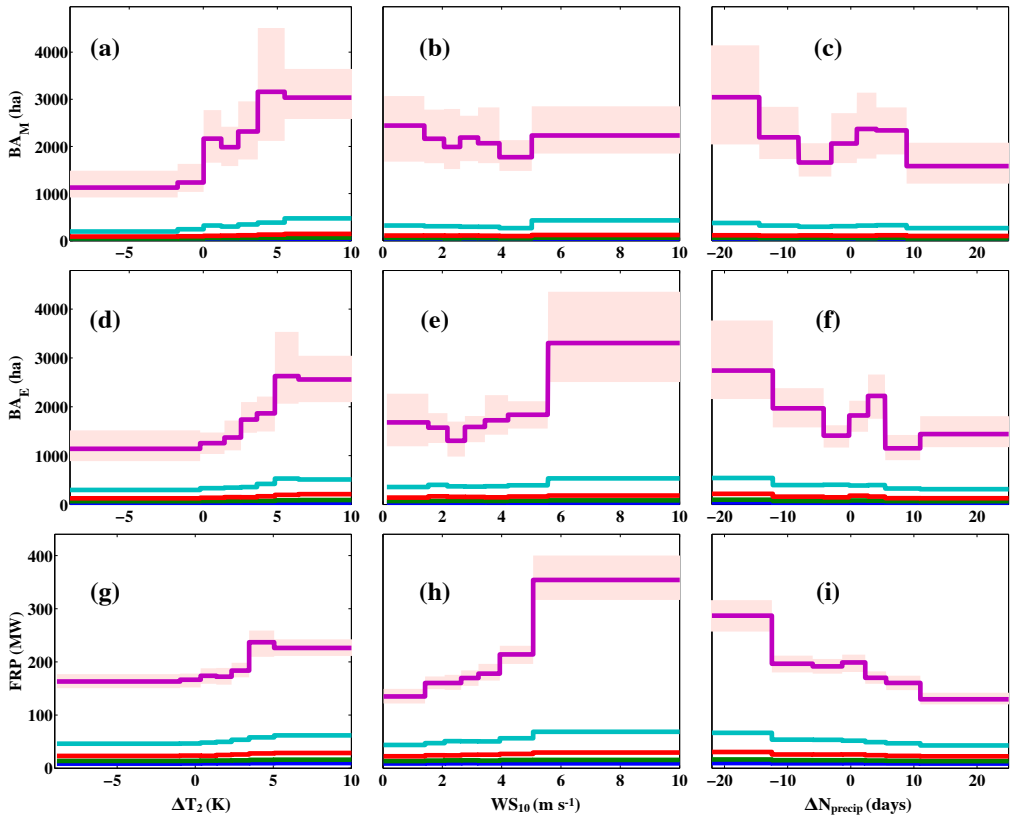

FIGURE 3.1: Evolution of 5^{th} (blue), 25^{th} (green), 50^{th} (red), 75^{th} (cyan) and 95^{th} (purple) quantiles of BA (data set BA_M and BA_E) and FRP (FRP data set) with ΔT_2, WS_{10} and ΔN_{precip}. Top row corresponds to BA_M, middle to BA_E and bottom to FRP. The red shaded area corresponds to 90% confidence intervals for the 95^{th} quantile.

Our first attempt at linking fire and weather data used regression techniques to forecast the conditional mean. This approach failed, with maximum R^2 of 0.10 and 0.05 for the FRP and BA data sets respectively using artificial neural networks. We therefore chose to focus our analysis on the variability of the

distributions of *BA* and FRP with respect to weather, and at first on the variations of the quantiles of these distributions. Figure 3.1 shows the variations of the 5^{th}, 25^{th}, 50^{th}, 75^{th} and 95^{th} quantiles of *BA* and FRP for data sets BA_M, BA_E and FRP with respect to the selected covariates. The methodology consists in splitting the data sets into 7 subsets containing an equal number of points. This allows comparable uncertainties for each subset. The number of bins was chosen as a trade-off between the smoothness of the curve and the significance of the curve fluctuations. These statistics were bootstrapped 1000 times, allowing an accurate estimation of each quantile and of the associated confidence intervals.
First, we can see that these variations depend heavily on the selected quantile. In particular the 5^{th} quantile seems roughly constant whereas the 95^{th} is more variable. *BA* and FRP show strong responses to ΔT_2, with general growth of fire size and radiative power. For the BA_E and FRP data sets, *BA* and FRP are growing functions of WS_{10}. This is not seen for the BA_M data set. However Hernandez et al. (2015c) show that by conditioning on ΔT_2 significant variations of *BA* and FRP can be observed at the 70% and 90% confidence levels respectively. We observe that *BA* and FRP decrease with increasing ΔN_{precip}.
In the following we use ΔT_2, WS_{10} and ΔN_{precip} to reconstruct the conditional distribution functions of *BA* and FRP.

3.2 *BA* and FRP distributions

Figure 3.1 shows that the variability of *BA* and FRP is very high, and a proper way to build a risk metric would be to compute probabilities of large fire size or large intensity using these variations. A way of doing so would be to model the conditional distributions of *BA* and FRP with respect to weather. To achieve this goal we want to find a parametric distribution which fits these variables well. In this section we proceed to this task independently of the weather covariates in order to provide good models for the distributions of *BA* and FRP. The meteorological covariates will be reintegrated at the beginning of Section 3.3.

As *BA* and FRP have very skewed distributions it becomes easier to study their logarithm. We therefore from this point onward only discuss the modeling of $\log_{10}(BA)$ and $\log_{10}(FRP)$. We also substract a threshold to each variable ($\log_{10}(25)$ for the *BA* data sets and $\log_{10}(4)$ for the FRP data set), so as the data starts approximately at 0 and is always non-negative.

The parametric forms that are tested for the distributions of the transformed fire variables are the following:

- the Exponential distribution, $f(x;\beta) = \beta e^{-\beta x}$, $x \in \mathbf{R}^+$;
- the Normal distribution, $f(x;\mu,\sigma) = \dfrac{1}{\sigma\sqrt{2\pi}} e^{-\dfrac{(x-\mu)^2}{2\sigma^2}}$, $x \in \mathbf{R}$;

Criterion	Data set	Normal	Exponential	Cauchy	Gamma	Logistic	Log-Normal	GEV
AD2R	BA_M	190	370	394	20.0	58.3	103	**20.3**
	BA_E	51.4	648	355	23.6	16.5	83.5	**3.45**
	FRP	674	4951	1626	**15.2**	121	124	17.8

TABLE 3.1: AD2R values for all different distributions and for all data sets. The AD2R values for the chosen distributions are in bold.

- the Cauchy distribution, $f(x;x_0,a) = \dfrac{1}{\pi a\left(1+\left(\dfrac{x-x_0}{a}\right)^2\right)}$, $x \in \mathbf{R}$;
- the Gamma distribution, $f(x;\alpha,\beta) = \dfrac{\beta^\alpha}{\Gamma(\alpha)} x^{\alpha-1}e^{-\beta x}$, $x \in \mathbf{R}^+$;
- the Logistic distribution $f(x;\mu,s) = \dfrac{e^{-\frac{x-\mu}{s}}}{s\left(1+e^{-\frac{x-\mu}{s}}\right)}$, $x \in \mathbf{R}$;
- the Log-Normal distribution, $f(x;\mu,\sigma) = \dfrac{1}{x\sigma\sqrt{2\pi}} e^{-\frac{(\log x-\mu)^2}{2\sigma^2}}$, $x \in \mathbf{R}^+$;
- the Generalized extreme value (GEV) distribution,
$f(x;\mu,\sigma,\xi) = \dfrac{1}{\sigma}[1+\xi\left(\dfrac{x-\mu}{\sigma}\right)]^{-1/\xi-1} e^{-[1+\xi\left(\frac{x-\mu}{\sigma}\right)]^{-1/\xi}}$, $x \in \mathbf{R}$, $x \geq \mu-\sigma/\xi$, $\xi > 0$.

Here f denotes the corresponding probability density function.

If Y is a random variable, the Truncated Exponential distribution for $\log Y$ correspond to the Truncated Pareto distribution for Y. As the Truncated Pareto distribution was shown alongside with the Tapered Pareto distribution to be a good fit for the distribution of *BA* (Schoenberg et al., 2003), we included the Exponential distribution in our possible forms for $\log_{10}(BA/25)$ and $\log_{10}(FRP/4)$.

We fitted all these distributions for each data sets (BA_M, BA_E and FRP) using the minimization of the AD2R goodness-of-fit criterion (Anderson and Darling, 1954) as fitting method. The AD2R criterion is defined as follows:

$$\text{AD2R}(F) = \int \left(\hat{F}_n(x) - F(x)\right)^2 \Psi(x)\mathrm{d}x, \text{ with } \Psi(x) = (1-F(x))^{-2}$$

with $\hat{F}_n$ is the empirical, step-wise cumulative density function of the data to fit and F the cumulative density function for which the AD2R criterion is calculated. The choice of the function Ψ gives more weight to the quality of the fit for the right tail of the distribution. If $F(x)$ and $\hat{F}_n(x)$ were to have different asymptotic behaviors for large values of x the AD2R criterion would be very large. The minimization of the AD2R criterion then has the theoretical advantage of making a better fitting of the distribution for

larger values of the selected variable.
All the AD2R values found for each distribution and data set are available in Table 3.1. Computations were done in R (R Core Team, 2013) using the fitdistrplus package (Delignette-Muller and Dutang, 2015). We see that for the *BA* data sets there are two distributions selected, Gamma and GEV. We will continue using only the GEV distribution since the difference seen for the BA_M data set between these two distribution is very small (AD2R values of 20.3 for the GEV distribution and 20.0 for the Gamma distribution), whereas for the BA_E data set the difference is much larger (AD2R values of 3.45 for the GEV distribution and 23.6 for the Gamma distribution). For FRP the Gamma distribution is selected.
Surprisingly the Exponential distribution fits the *BA* data sets poorly. This could be due to the absence of the < 25 *ha* wildfires in our BA_M and BA_E data sets, whereas they are taken into account in Schoenberg et al. (2003).

Figure 3.2 shows the normalized histograms and modeled densities of BA and FRP with accompanying QQ-plots for all considered data sets. The QQ-plots were computed using the car package (Fox and Weisberg, 2011). For values of BA smaller than 40 *ha*, the QQ-plots depart from the 95%-level confidence intervals. Conversely, the QQ-plots are within the confidence intervals for larger values. The distribution fits better the BA_E data set than the BA_M. It may be due to the methodology of construction of this data set, which considers burned only the fraction of the burning MCD64A1 pixels of surface 25 *ha* covered by vegetation. A preference for multiples of 25 *ha* arises and it is detrimental for the accuracy on the distribution tails of *BA*, and especially the lower percentiles. However, the fit is still accurate enough for our purpose. As only the largest wildfires are controlled by the weather conditions (Hernandez et al., 2015a), having an accurate fit of the high values of *BA* and FRP is enough for our modeling framework. Caution should therefore be taken when trying to interpret these distributions for low values of *BA*. For FRP, the QQ-plot remains within the 95%-level confidence intervals for all values. Besides the AD2R criterion, Fig. 3.2 shows that the GEV and Gamma models fit the data accurately and can be considered suited for our model.
In the following, we will take the strong hypothesis that the observations coming from the *BA* and FRP data sets have respectively GEV and Gamma distributions conditionally to the weather. This hypothesis was tested on large subsets of the data sets corresponding to particularly favorable or unfavorable weather conditions. We take as favorable conditions $\Delta T_2 \geq 5\ K$ and $WS_{10} \geq 6\ ms^{-1}$ and as unfavorable conditions $\Delta T_2 \leq 0$ and $WS_{10} \leq 3\ ms^{-1}$. We find that the hypothesis holds well for the BA_E and FRP data sets, but that there are more discrepancies with the BA_M data set, which is coherent with the deviations seen in Fig. 3.2.
This hypothesis is used to obtain the conditional distribution of *BA* and FRP with respect to ΔT_2, WS_{10} and ΔN_{precip}.

3.3 Fire risk assessment using meteorological covariates

3.3.1 Methodology

The general framework of our methodology is the parametric estimation of the conditional probability density function of *BA* or *FRP* with respect to ΔT_2, WS_{10} and ΔN_{precip}. In other words we seek $f_{Y|\mathbf{X}}(y) = f_Y(y|\mathbf{X} = \mathbf{x})$ with y the fire variable, with $\mathbf{X}$ the meteorological covariates and $\mathbf{x}$ a specific value taken by the covariates. We made the hypothesis in the previous section that $f_{\log_{10}(BA/25)} \sim \text{GEV}(\mu,\sigma,\xi)$ and $f_{\log_{10}(FRP/4)} \sim \text{Gamma}(\alpha,\beta)$ for all subsets of our data sets. Therefore to approximate the values of the parameters of these distributions we need to compute the distribution of y near the point $\mathbf{X} = \mathbf{x}$. To do so we choose to retain the 10% of our data sets nearest of the point $\mathbf{X} = \mathbf{x}$ and to estimate the parameters of the distribution by minimizing the AD2R criterion. The fraction of nearest neighbors was chosen to be sufficient to estimate a distribution function. The calculation of these nearest neighbors was done in R using the FNN package (Beygelzimer et al., 2013).
It must be noted that due to the curse of dimensionality taking a larger number of covariates would lead to a very large inaccuracy on $\mathbf{x}$ (Hastie et al., 2009, pp 22-23).
For computation purposes we choose not to estimate $f_{Y|\mathbf{X}}$ at each possible value of $\mathbf{x}$. Instead we take the values of $\mathbf{x}$ corresponding to the 1^{st} to 9^{th} deciles of each of its components. This makes 9^3 = 729 values of $\mathbf{x}$ for which each conditional distribution parameters are estimated.
In order to obtain asymptotic confidence intervals for our estimates of the conditional distribution parameters and of the probability of large or intense events we perform 500 bootstrap estimations of these parameters using the determined nearest neighbors. Bootstrap estimation was done using the bootstrap R package (Leisch and Tibshirani, 2014).

3.3.2 Results

Figures 3.3, 3.4 and 3.5 show the estimated probability contours of particularly large or intense fire events computed from our method. These events are defined by the wildfire exceeding the 2000 *ha* or 200 *MW* thresholds in *BA* or *FRP* respectively. These thresholds correspond approximately to the 95^{th} quantiles of each variable. The values of each class of ΔN_{precip} corresponds to the mean of the ΔN_{precip} of each decile. Each panel displays the mean distribution of the corresponding ΔN_{precip} class. The uncertainty of the distribution can be inferred from Table 3.2 which displays the average standard deviation of each covariate.
The probability of large *BA* occurring is a growing function of ΔT_2 (Figs. 3.3 & 3.4). The two modes of higher *BA* commented and analyzed in Hernandez et al. (2015c) are visible in Fig. 3.3. There is a clear significant increase in large *BA* probabilities with increasing ΔT_2 and WS_{10} for low values of ΔN_{precip}. The role of WS_{10} is significantly damped when ΔN_{precip} rises (wetter January-June time period) and ΔT_2

becomes the main driving factor for the BA_M data set (Fig. 3.3). Accounting for the confidence intervals of the estimated probabilities (not shown) shows that WS_{10} has no explanatory value in the pattern of the probability at the 90% confidence level. The variations between the minima and maxima of the estimated probabilities are significant at the 90% confidence level. However the two modes are hard to distinguish statistically because of the low number of points in our *BA* data sets (5821 for BA_M and 4840 for BA_E). The difference of results between the BA_M and BA_E probabilities is due to the BA_E data set spanning over the 2006-2012 time period, therefore missing the 2003 and 2005 megafire events which are present in the BA_M data set (San-Miguel-Ayanz et al., 2013). Regarding fire intensity, FRP is a growing function of WS_{10}, ΔT_2 and a decreasing function of ΔN_{precip}, which is significant at the 90% confidence level. The variability linked to ΔT_2 and WS_{10} is discussed in Hernandez et al. (2015a) and found back on this figure.

Because we use a meteorological covariate depending on past weather (ΔN_{precip}), a seasonal preconditioning of high fire risk can be assessed. When a drought occurs in the past months ($\Delta N_{precip} \leq -7$ days) the highest probabilities of large *BA* can be found for high values of both ΔT_2 and WS_{10} (Fig. 3.3). For higher values of the past months precipitation anomaly ($\Delta N_{precip} \geq 7$ days), the highest risk corresponds to heatwaves, with high ΔT_2 and low WS_{10}. This difference could be exploited to adapt fire mitigation strategies and take into account seasonal weather information.

The absence of the 2003 and 2005 megafire events (San-Miguel-Ayanz et al., 2013) limits the number of observations used to derive the parameters of the distributions, therefore explaining the absence of significant discrimination between situations of spring drought and the others in the BA_E data (Fig. 3.4).

Let us illustrate the information provided by our method by focusing on the 2003 megafire event in Portugal. We take the largest wildfire event of the BA_M data set (262520 ha BA, 731 MW FRP). It is recorded at [-7.65E,40N] and the considered weather is that of the [-7.50E,39.75N] ERA-Interim grid point.

Figure 3.6 shows the time evolution of the probability of large *BA* and FRP with the corresponding 90% confidence intervals. Two black lines show the beginning and the end of the fire event. During the wildfire the probability of large *BA* peaks to 7 %, whereas it stays at about 3 % (BA_M) or 2% (BA_E) the rest of the time. The probability of large FRP behaves the same way, going from 3% to more than 6%. The variations of these estimated probabilities are significant at the 90% confidence level. The "background" probability refers to the background fire risk of large or intense fire events during summer. We also see a secondary peak before the fire event, even though no fire occurred. Our method can be used to identify time periods when fire risk is especially high. When a fire occurs during one of these "extreme" periods, the fire event has large odds of being catastrophic.

Regarding the uncertainties of the method the mean standard deviation of the meteorological covariates have been calculated (Table 3.2). They stem from our nearest neighbors approach. The uncertainties on the meteorological features are fairly small and, with the exception of ΔN_{precip}, fall within measurement

Data set	ΔT_2 (K)	WS_{10} (ms^{-1})	ΔN_{precip} (days)
BA_M	1.41	0.74	4.4
BA_E	1.22	0.83	3.9
FRP	1.17	0.74	4.4

TABLE 3.2: Mean values of the standard deviations calculated from the nearest neighbors search (ΔT_2, WS_{10} and ΔN_{precip}).

error.

Figure 3.7 shows the normalized histograms of the estimated probabilities and of the confidence intervals lengths for all July-August time periods everywhere a fire is detected. We also quantify the mean and standard deviation of the background and extreme fire risk regimes. To do this, the densities of the estimated probabilities are fitted with a mixture of two gaussians, representing the background and extreme fire risk regimes. The model can be written as follows:

$$PDF(x;\mu_1,\sigma_1,\mu_2,\sigma_2,\alpha) = \frac{\alpha}{\sigma_1\sqrt{2\pi}} \times \exp\{-\frac{(x-\mu_1)^2}{2\sigma_1^2}\} + \frac{1-\alpha}{\sigma_2\sqrt{2\pi}} \times \exp\{-\frac{(x-\mu_2)^2}{2\sigma_2^2}\} \qquad (3.1)$$

For BA_E data set, the distinction between background and extreme is more difficult than for BA_M due to the absence of major megafires in the data set (2003 and 2005). Otherwise, the mean probability that a fire exceeds 2000 *ha* is around 4% for background summer fire risk conditions with a standard deviation of 0.5% and increases to 5% in extreme weather conditions favorable to larger fires. A similar behavior is found for fire intensity with an even more distinguishable two mode distribution. The mean probability that a fire exceeds 200 MW is around 2.4% for background summer fire risk conditions with a standard deviation of 0.3% and increases to 3.6% in extreme weather conditions favorable to intense fires. The 90%-level confidence interval lengths remain large for the BA data sets, with typical values of 2% and 1.8% for the BA_M and BA_E data sets respectively. For the FRP data set these lengths are smaller because of the larger number of data points, with a mean value of approximately 1%.

3.4 Conclusions

Statistical modeling of burnt area (BA) and fire radiative power (FRP) was investigated in this chapter. Using maximum goodness-of-fit techniques the density functions of $\log_{10}(BA)$ and $\log_{10}(FRP)$ were found to be well represented by GEV and Gamma distributions respectively. Using the hypothesis that this result holds for the conditional distribution of the fire variables with respect to meteorological covariates, a methodology for its estimation with three weather parameters was designed. Surface wind speed, 2-meter air temperature anomaly and rainfall occurrence anomaly in January-June were selected to fit BA and FRP. The statistical model proved to be efficient in associating large fire risk with previous fire events, and so with rather low uncertainties. Such a model would be useful for the design of a data-driven wildfire alert system in the Mediterranean Basin taking into account seasonal trends and weather

forecasts.

- Our model allows to discriminate accurately jumps between background summer fire risk regime and an extreme additional fire risk regime, corresponding to higher probability of occurrence of larger fire size or intensity associated with specific weather conditions;

- our model provides information for both the fire size and the fire intensity;

- our model provides an estimation of the probability of risk to exceed given values of fire size and fire intensity each time meteorological forcing data are available, that is typically on an hourly to 6-hourly basis;

- our model includes enhanced fire risk preconditioning by precipitation occurrence anomaly during the preceding months.

However, this work must be seen as a first step towards fire risk forecasting and a thorough analysis is required to assess the model performance in forecast mode.
In this study we use parametric distributions as they provide a simple framework to model fire risk with a limited number of coefficients, which can be of interest for the implement of a fire risk forecast system. Non parametric estimations of the conditional distributions of the fire variables with respect to the meteorological covariates could be performed (Brunel et al., 2010). This would lead to longer computation times but probably more accurate estimations of the conditional distributions and associated probabilities. More complete data sets for *BA* would allow a better estimation of the conditional distribution for this particular variable and help further reduce the uncertainties.
Finally the developments shown in this chapter lead to an answer to our second research objective. To improve fire danger forecasting meteorological driving factors of fire size and intensity can be used to reconstruct a conditional distribution function of either variable. Such method provides much more information than commonly used fire risk indicators (e.g. the Canadian Fire Weather Index) as one gets the distribution of all possible fire sizes and intensities given the meteorological covariates rather than an estimation of the fire intensity alone. The method also allows a multi-time-scale analysis of the fire risk level as it accounts for preconditioning build-up by spring drought and the instantaneous wind speed and temperature anomaly with respect to the climatology. It thus produces a contrasted day-to-day probability of large fire size and intensity which can be combined into a single fire risk indicator.

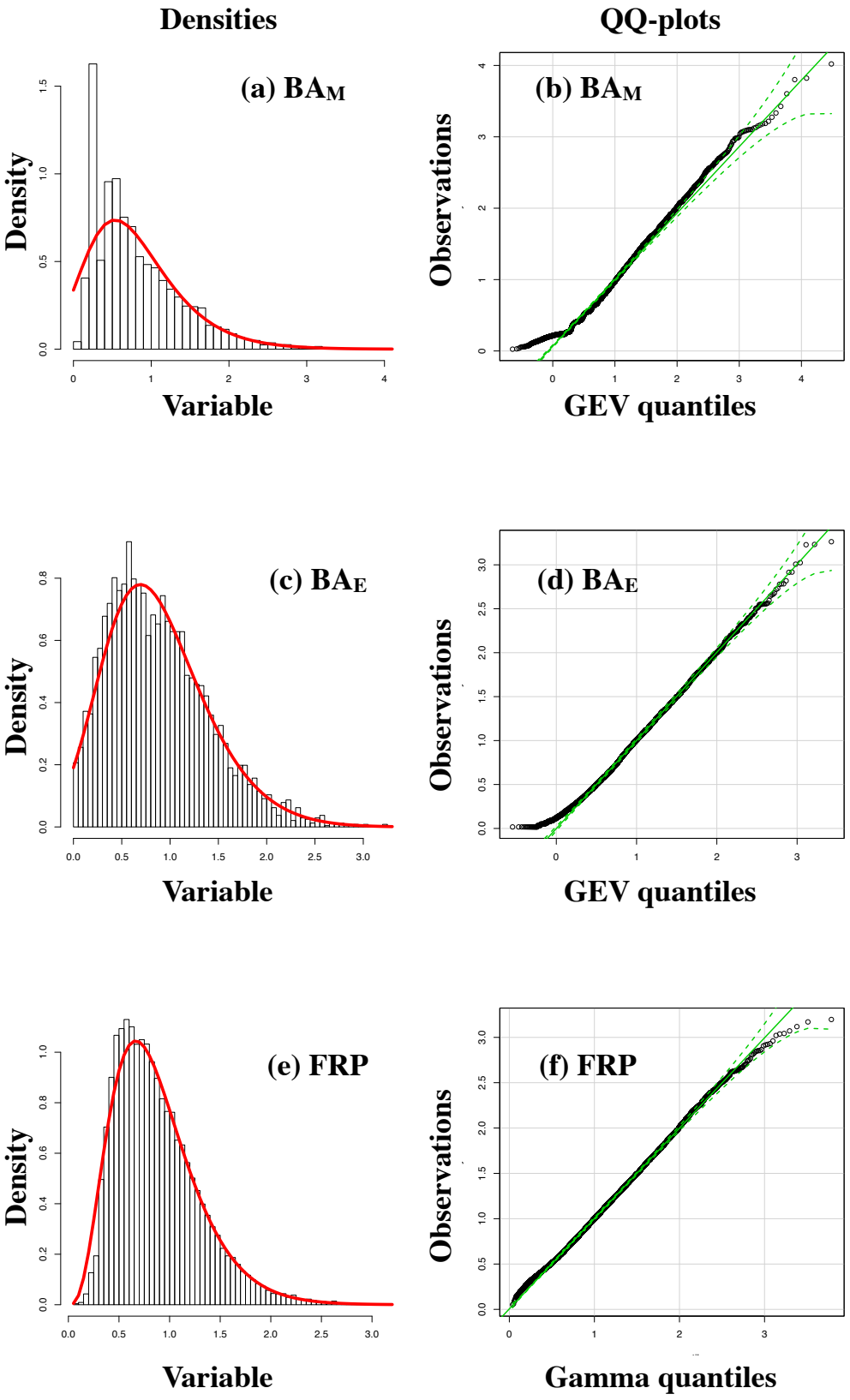

FIGURE 3.2: Normalized histograms, modeled densities (a,c,e) and QQ-plots (b,d,f) for the GEV and Gamma distributions for the *BA* and *FRP* data sets respectively. The fitting method used is the AD2R criterion minimization. On the densities panels the normalized histograms are in black and the modeled distribution in red. The dashed green lines on the QQ-plots are the 95% confidence envelopes.

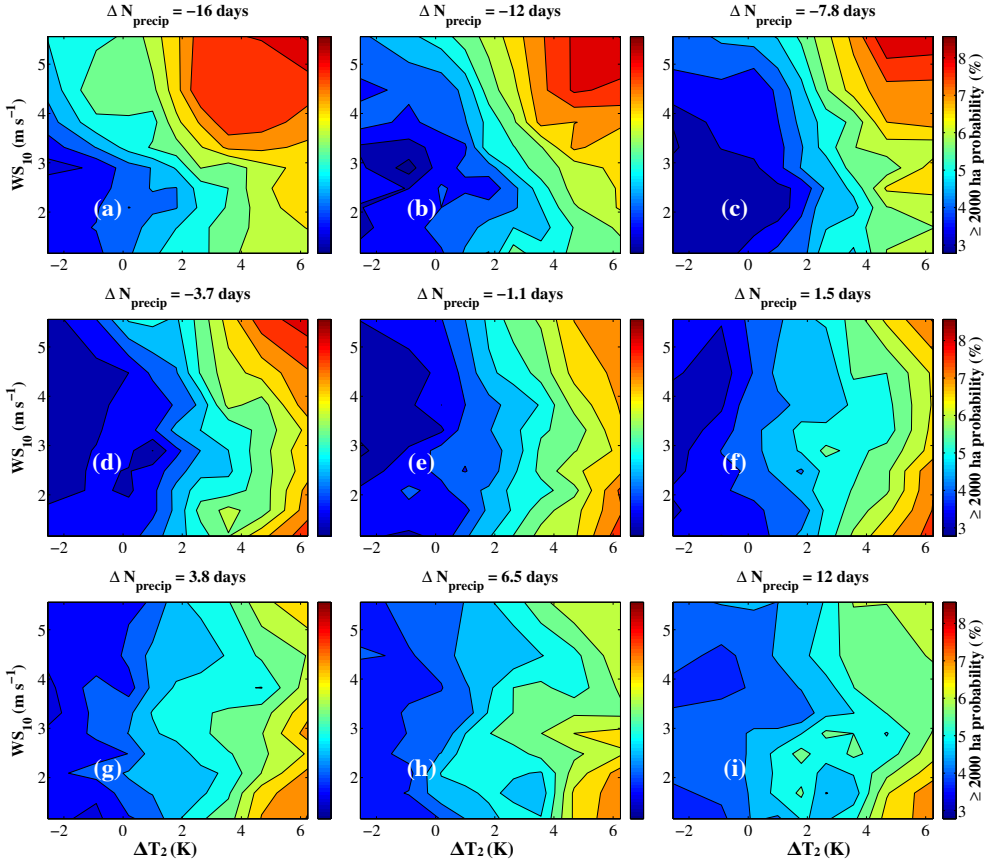

FIGURE 3.3: Estimated probabilities of fire size (*BA*) exceeding the 2000 *ha* threshold (BA_M data set). The x-axis is the 2-meter air temperature anomaly (ΔT_2), the y-axis the 10-meter wind speed (WS_{10}) and each panel stands for values of January-June precipitation days anomaly (ΔN_{precip}) centered on the given value on the panel titles.

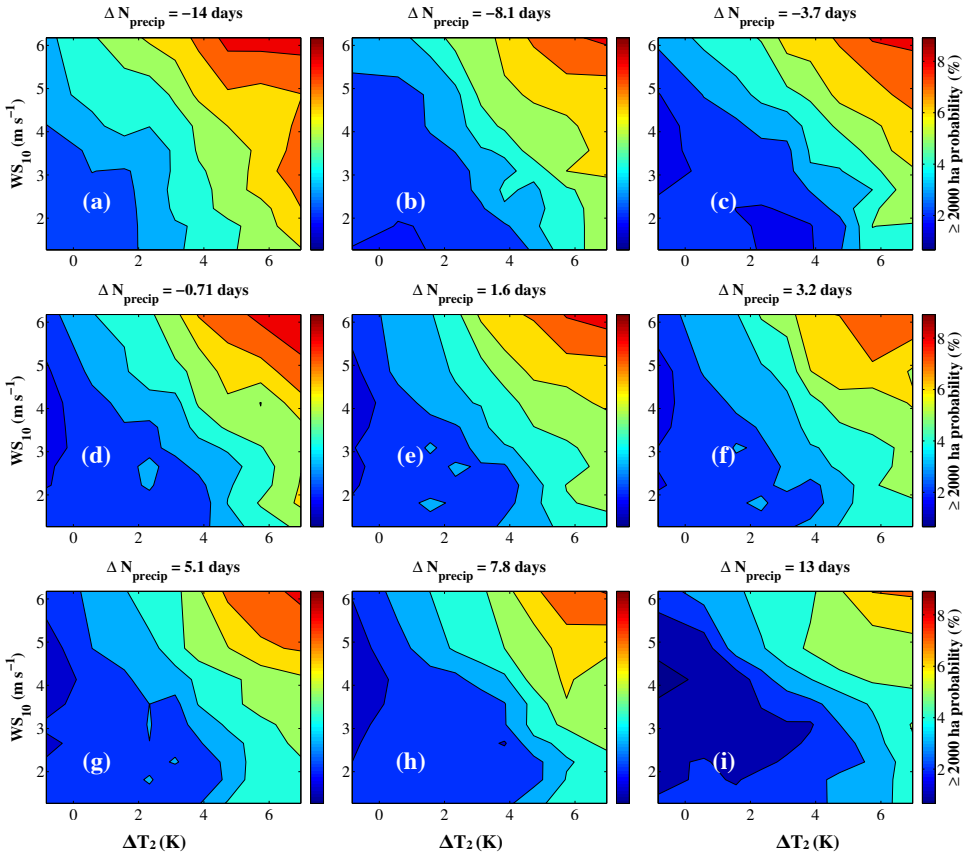

FIGURE 3.4: Estimated probabilities of fire size (*BA*) exceeding the 2000 *ha* threshold (BA_E data set). The x-axis is the 2-meter air temperature anomaly (ΔT_2), the y-axis the 10-meter wind speed (WS_{10}) and each panel stands for values of January-June precipitation days anomaly (ΔN_{precip}) centered on the given value on the panel titles.

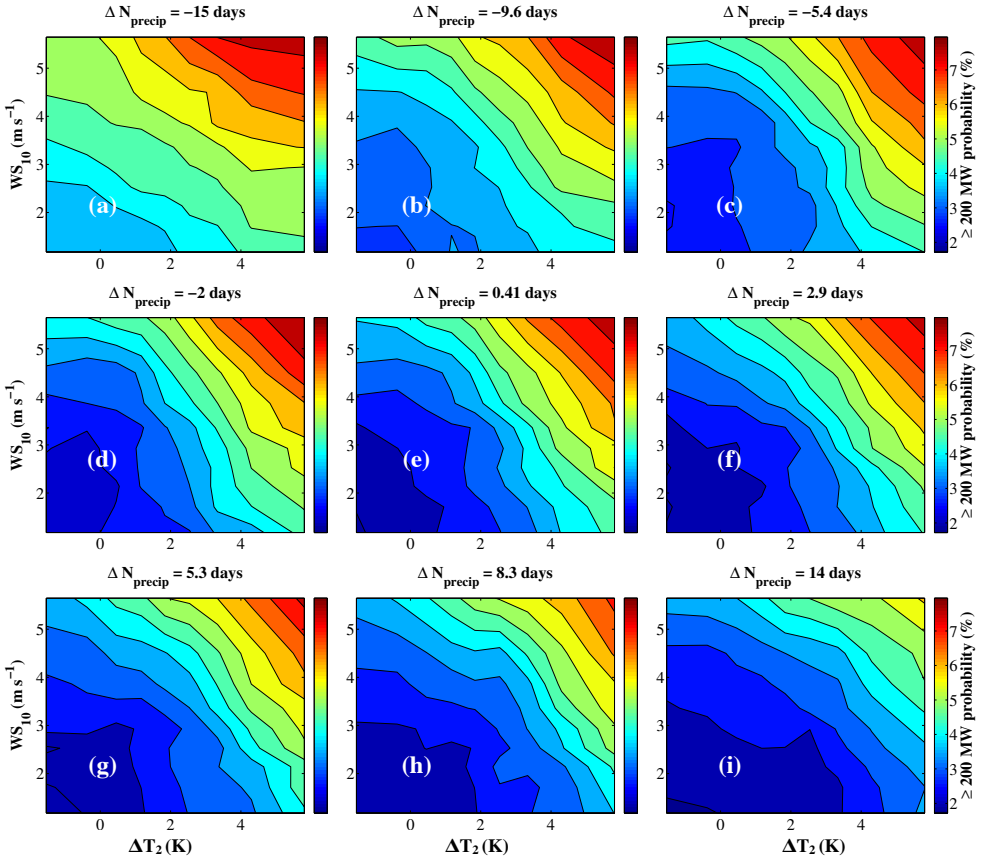

FIGURE 3.5: Estimated probabilities of fire intensity (FRP) exceeding the 200 *ha* threshold. The x-axis is the 2-meter air temperature anomaly (ΔT_2), the y-axis the 10-meter wind speed (WS_{10}) and each panel stands for values of January-June precipitation days anomaly (ΔN_{precip}) centered on the given value on the panel titles.

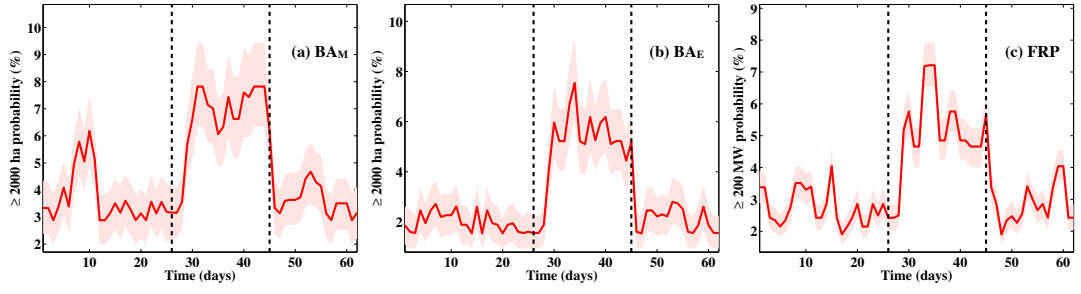

FIGURE 3.6: Probabilities of observing a $\geq$ 2000 *ha* wildfire calculated from the BA_M (a) and BA_E (b) data sets and probabilities of observing a $\geq$ 200 *MW* wildfire calculated from the FRP data set (c) as a function of time for the 2003 July-August period nearest the largest wildfire occurring in Portugal this season. Black dashed lines show the beginning and the end of the wildfire event. In light shaded red are the 90% confidence intervals.

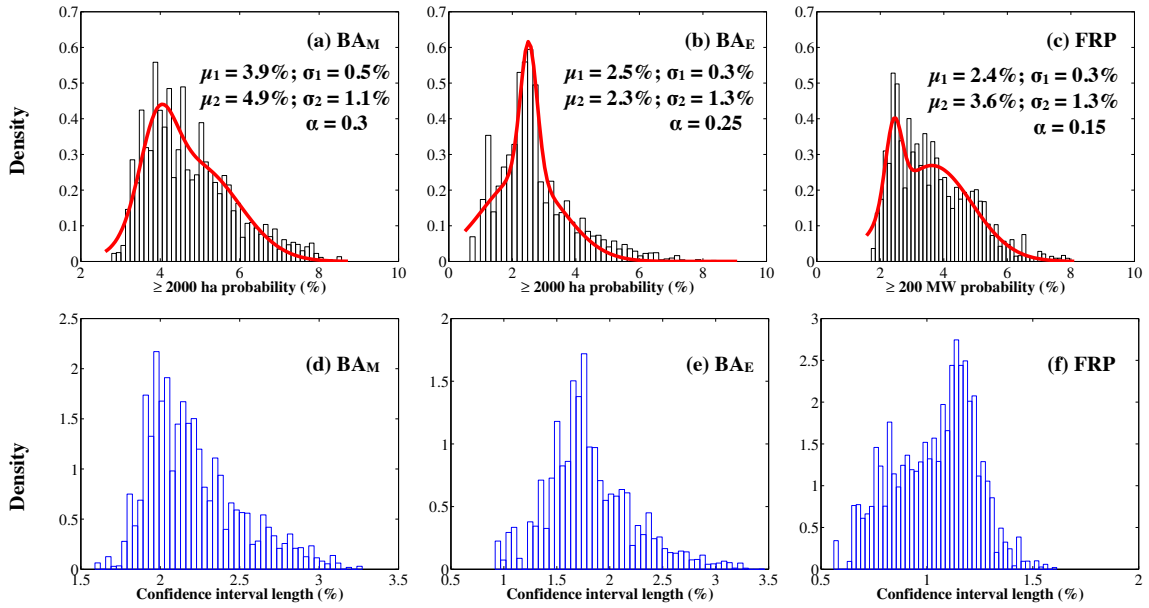

FIGURE 3.7: Normalized histograms of the estimated probabilities (black), PDFs of the mixture model (red) and normalized histograms of the 90%-level confidence intervals lengths (blue). (a,d) are for BA_M, (b,e) for BA_E and (c,f) for FRP. The data set is made of each July-August time period everywhere a fire is detected. The parameters of the gaussian mixture model (Eq. 3.1) are displayed on each panel of the top row.

Chapter 4

Impact of wildfire-induced land cover modification on local meteorology

This chapter stems from the article Hernandez et al. (2015b), published in Atmospheric Research.

Wildfires alter land cover creating changes in dynamic, vegetative, radiative, thermal and hydrological properties of the surface. However, how so drastic changes induced by wildfires and how the age of the burnt scar affect the small and meso-scale atmospheric boundary layer dynamics are largely unknown. These questions are relevant for process analysis, meteorological and air quality forecast but also for regional climate analysis. Such questions are addressed numerically in this study on the case of the Portugal wildfires in 2003 as a testbed. In order to study the effects of burnt scars, an ensemble of numerical simulations using the Weather Research and Forecasting modeling system (WRF) have been performed with different surface properties mimicking the surface state immediately after the fire, few days after the fire and few months after the fire. In order to investigate such issue in a seamless approach, the same modeling framework have been used with various horizontal resolutions of the model grid and land use, ranging from 3.5 km, which can be considered as the typical resolution of state-of-the art regional numerical weather prediction models to 14 km which is now the typical target resolution of regional climate models.

The study shows that the combination of high surface heat fluxes over the burnt area, large differential heating with respect to the preserved surroundings and lower surface roughness produces very intense frontogenesis with vertical velocity reaching few meters per second. This powerful meso-scale circulation can pump more humid air from the surroundings not impacted by the wildfire and produce more cloudiness over the burnt area. The influence of soil temperature immediately after the wildfire ceases is mainly seen at night as the boundary-layer remains unstably stratified and lasts only few days. So the intensity of the induced meso-scale circulation decreases with time, even

though it remains until full recovery of the vegetation. Finally all these effects are simulated whatever the land cover and model resolution and there are thus robust processes in both regional climate simulations and process studies or short-time forecast. However, the impact of burnt scars on the precipitation signal remains very uncertain, especially because low precipitation are at stake.

4.1 Context and introduction

These wildfires have become over the past ten years an active research field in geophysics and ecology (DeBano, 2000, Westerling et al., 2006). Large forest or bush fires cause dramatic changes in atmospheric composition by the release of gaseous and solid combustion products that in turn alter the local (Davies and Unam, 1999) and global (Seiler and Crutzen, 1980) atmospheric composition. The large release of heat and cloud condensation nuclei (Petters et al., 2009) modifies deeply the meteorology during the fire event, as seen in the fire propagation models (Clark et al., 1996, Morvan and Dupuy, 2004). At the catchment level, the water cycle is also impacted by fire. For example the response time of the topsoil moisture can be significantly lowered by wildfires, inducing quicker drying after rainfall (Stoof et al., 2012). Local meteorology can also be impacted after the fire ceases. Mölders and Kramm (2007) showed that in boreal regions fires tend to thaw the permafrost layer of the soil, blacken the surface and decrease the roughness length. Their numerical experiment showed an increase over the burnt areas and a decrease downwind of cloud-water, rain-water and graupel mixing ratios. A rearrangement of precipitation pattern is also simulated over the burnt area due to modifications of surface flux and buoyancy. Such effects are similar to anthropogenic or natural modifications of the landscape which can change in return the surface heat budget and therefore the surface-atmosphere coupling. These surface heterogeneities induce meso-scale circulations (Avissar and Schmidt, 1998, Pielke et al., 1991, Segal et al., 1988) which can have consequences on the local meteorology (Kilinc, 2007, Wendt et al., 2007). Tryhorn et al. (2008) also showed evidence of the link between flash floods that occurred in the Alpine Shire, Australia with 37.2 mm recorded precipitation. The numerical experiment showed that without accounting for the fire occurrence the simulated precipitation were 3.9 mm versus 31.7 mm when accounting for the fire occurrence. At a larger time scale, Görgen et al. (2006) showed by using a fire/regrowth scheme in a climate model, that the vegetation regrowth time scale depends on the intensity of the fire. The impact of fires on landscape dynamics and their possible impact on global climate make them an interesting field of research for more accurate future climate forecasting (Trouet et al., 2010). Burnt scars and wildfires have not yet been incorporated into climate simulations, but their contributions to vegetation dynamics (Mouillot et al., 2002), carbon balance (Schimel and Baker, 2002) and aerosol concentrations (Spracklen et al., 2009) in a context of climate change have been investigated. These study did not focus on the Mediterranean region, which has however a long record of large wildfire events.

However, several questions remain unanswered in the current literature, which will be addressed in the present chapter. We do not know precisely what is the magnitude of the changes in small and meso-scale atmospheric dynamics that occur above large fire burnt scars. The change in energy budget being drastic compared to what is observed usually in studies about land-cover contrasts, large modification of the boundary layer dynamics should be expected. How the age of the burnt scar impacts the boundary-layer dynamics is also largely unknown. These questions are relevant for process analysis, meteorological and air quality forecast but also for regional climate analysis. In order to investigate such issue in a seamless approach, the same modelling framework will be used with various horizontal resolutions of the model grid and land use. It will range from 3.5 km, which can be considered as the typical resolution of state-of-the art regional numerical weather prediction models (Davies et al., 2005, Seity et al., 2011), to 14 km which is now the typical target resolution of regional climate models (Flaounas et al., 2013, Jacob et al., 2014). The 2003 Portuguese fire season is used as a testbed for such sensitivity study experiment (Fig. 4.1). The study uses the Weather Research and Forecasting model WRF for the sensitivity analysis and the Moderate Resolution Imaging Spectroradiometer (MODIS) observations for the description and map of the burnt area.

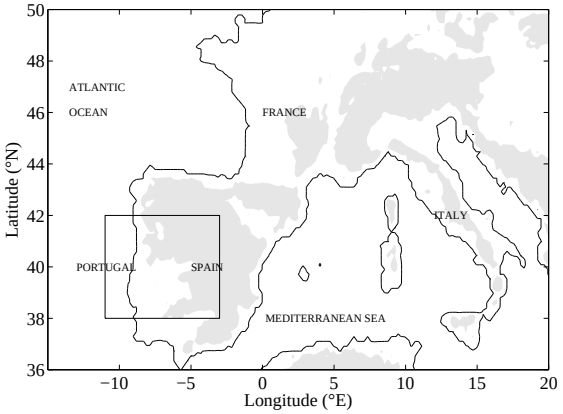

FIGURE 4.1: Map of the western Mediterranean region with shaded area indicating topography higher than 500 m. The rectangle indicates the simulation domain for this study.

4.2 Numerical experiments with WRF

4.2.1 Model setup

Version 3.1 of the Weather Research and Forecasting model (WRF) of the National Center of Atmospheric Research (NCAR) (Skamarock and Klemp, 2007) is used, with a simulation domain covering the western region of the Iberian Peninsula with horizontal resolutions of 3.5, 7 and 14 km. The corresponding time steps are 15 s, 30 s and 60 s. The model has 28 sigma-levels in the vertical. Initial and lateral conditions are taken from the European Center for Medium-range Weather Forecast (ECMWF)

ERA-interim reanalysis provided every 6 hrs with a 0.75° resolution (Simmons et al., 2006). To avoid unrealistic departure from the driving fields, indiscriminate nudging is applied with a coefficient of 5×10^{-5} s^{-1} for temperature, humidity and velocity components above the planetary boundary layer (Omrani et al., 2013, Salameh et al., 2010) (even though the small domain size damps the effect of nudging with strong control by lateral boundaries; Omrani et al., 2012, 2013). A complete set of physics parameterizations is used with the WRF Single-Moment 5-class microphysical scheme (Hong et al., 2004), the new Kain-Fritsch convection scheme (Kain, 2004), the Yonsei University (YSU) planetary boundary layer (PBL) scheme (Noh et al., 2003) and a parameterization based on the similarity theory (Monin and Obukhov, 1954) for the turbulent fluxes. The radiative scheme is based on the Rapid Radiative Transfer Model (RRTM) (Mlawer et al., 1997) and the Dudhia (1989) parameterization for the longwave and shortwave radiation, respectively. For the land surface, the NOAH land-surface model is used (Ek et al., 2003). It uses four soil layers of respective depths from top to bottom 10 cm, 30 cm, 60 cm and 100 cm. The geographical data are from 30 second resolution USGS (United States Geophysical Survey) data. The output time interval for all simulations is 1 hour.

4.2.2 Performed simulations

Reference simulations (hereafter referred as REF) have been run at 3.5, 7 and 14 km horizontal resolutions with the standard land use characteristics from the USGS database, i.e. without accounting for the wildfire impact. Additional simulations have been performed by modifying the land use characteristics (albedo, emissivity, roughness, and vegetation) and initial state (soil temperature and moisture) to account for the fire impact (Fig. 4.2):

- Simulations FIRE-ST include modified soil temperature and moisture in the uppermost layer in the initial state (+300 K additional temperature and 0.05 $m^3.m^{-3}$ soil moisture at the beginning of the simulations) as well as modified land-cover (see hereafter for details). These simulations performed at 3.5, 7 and 14 km horizontal resolutions mimic the situation when the fire has ended at the beginning of the simulation and so the ”short-term” response of the atmosphere (”ST” in ”FIRE-ST” standing for short-term).

- Simulations FIRE-MT include modified soil moisture in the uppermost layer in the initial state (0.05 $m^3.m^{-3}$ soil moisture at the beginning of the simulations) as well as modified land-cover (see hereafter for details). These simulations performed at 3.5, 7 and 14 km horizontal resolutions mimic the situation when the fire has ended few days before the beginning of the simulation and so the ”mid-term” response of the atmosphere (”MT” in ”FIRE-MT” standing for mid-term).

- Simulations FIRE-LT include modified land-cover only (see hereafter for details). These simulations performed at 3.5, 7 and 14 km horizontal resolutions mimic the situation when the fire has ended fews months before the beginning of the simulation and so the ”long-term” response of the atmosphere (”LT” in ”FIRE-LT” standing for long-term).

Simulations FIRE-ST are the most similar regarding the actual summer 2003 wildfire in Portugal. Simulations MT and LT allow to analyze the longer term atmospheric response to a wildfire all others things being equal (i.e. synoptic atmospheric conditions).

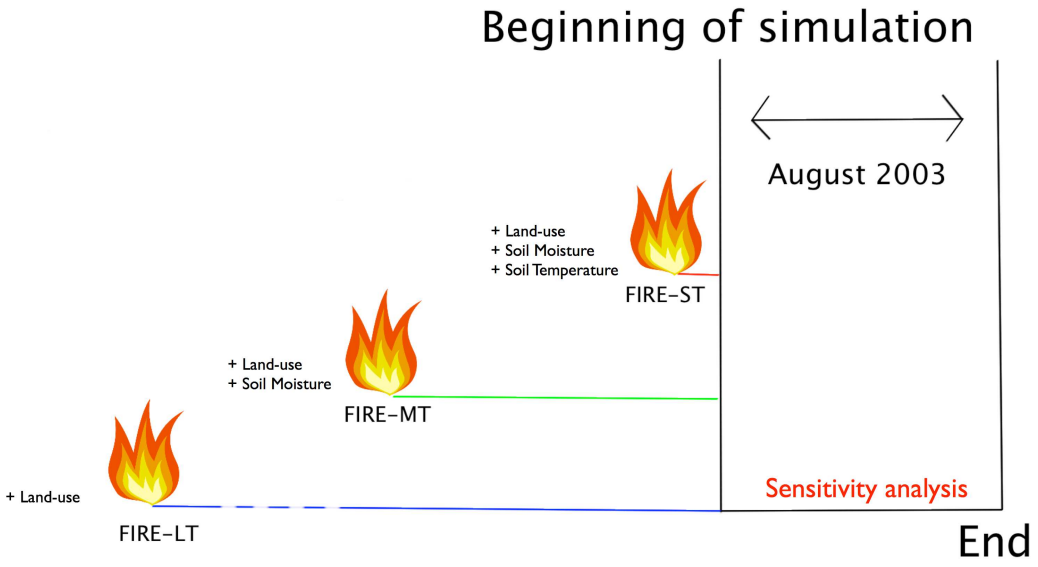

FIGURE 4.2: Sketch of the numerical sensitivity experiment.

To identify the burnt regions and the dates of the corresponding fires, we use the MCD64 burnt area product from the spaceborne instrument MODIS (Moderate Resolution Imaging Spectroradiometer). This product provides such information on a 500 m horizontal grid. We concatenate the burnt pixels over the wildfire duration in July 2003 to obtain the map of the burnt scar at the beginning of August 2003. To modify the land-cover characteristics of WRF over the burnt area, we consider that a WRF grid cell corresponds to a burnt landscape if more than 20% of its area is burnt according to the MCD64 product. Figure 4.3 shows the burnt area for the simulations performed at 3.5, 7 and 14 km. However, in order to delineate the effect of the horizontal resolution on the atmospheric dynamics from that of the shape of the burnt area, an additional set of simulations has been produced. Simulations performed at 3.5 and 7 km horizontal resolution with the consistent land use (i.e. computed with 3.5 and 7 km-grid cells, respectively; simulations referred as ”HR” for ”high resolution” land use description) have also been run with a modified land use computed with 14-km resolution grid cells (simulations referred as ”LR” for ”low resolution” land use description). Table 4.1 summarizes the simulations performed for the sensitivity analysis.

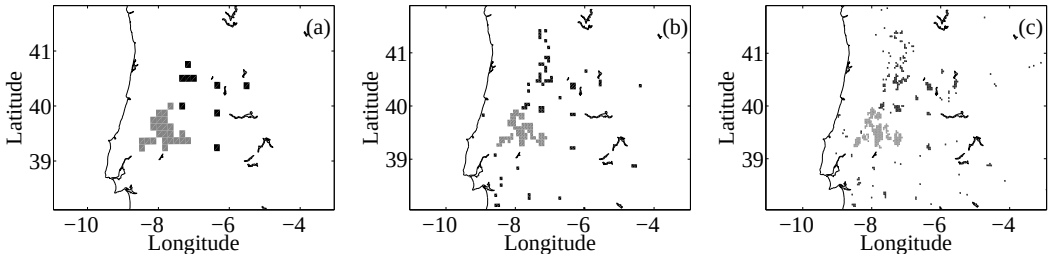

FIGURE 4.3: Maps of burnt area for 14-km-resolved (a), 7km-resolved (b) and 3.5km-resolved land-use (c). Gray is for the large patches and black the small ones.

Group	Changes in surface properties	Abbreviation	Grid resolution	land-cover resolution
REF	None	REF-14	14 km	14 km
		REF-7-LR	7 km	14 km
		REF-7-HR	7 km	7 km
		REF-3.5-LR	3.5 km	14 km
		REF-3.5-HR	3.5 km	3.5 km
FIRE-LT	land-cover	FIRE-LT-14	14 km	14 km
		FIRE-LT-7-LR	7 km	14 km
		FIRE-LT-7-HR	7 km	7 km
		FIRE-LT-3.5-LR	3.5 km	14 km
		FIRE-LT-3.5-HR	3.5 km	3.5 km
FIRE-MT	land-cover + Soil moisture	FIRE-MT-14	14 km	14 km
		FIRE-MT-7-LR	7 km	14 km
		FIRE-MT-7-HR	7 km	7 km
		FIRE-MT-3.5-LR	3.5 km	14 km
		FIRE-MT-3.5-HR	3.5 km	3.5 km
FIRE-ST	land-cover + Soil moisture + Soil temperature	FIRE-ST-14	14 km	14 km
		FIRE-ST-7-LR	7 km	14 km
		FIRE-ST-7-HR	7 km	7 km
		FIRE-ST-3.5-LR	3.5 km	14 km
		FIRE-ST-3.5-HR	3.5 km	3.5 km

TABLE 4.1: List of all performed simulations.

4.2.3 Burnt land cover class in WRF "FIRE" simulations

Regarding the modeling of the burnt surfaces in the WRF simulations, a "burnt area" land cover class has been added with modified parameters such as albedo, emissivity, leaf-area index, leaf transpiration parameters (stomatal resistance, radiation stress factor and coefficient for vapor pressure deficit) and roughness length.

The radiative properties of the land surface are altered by the combustion of the pre-existing vegetation cover. Fires burn the leaves, blacken the branches and trunks and produce ash and soot. Results from the BOREAS flight experiments conducted in Canada showed lowered albedo for recently burnt forest areas (Amiro et al., 1999). The same behavior was observed using flux tower measurements in the northern Australian savanna. In this region, the albedo decreases from 0.11 to 0.06 and 0.12 to 0.07 for low and moderate fire intensities, respectively (Beringer et al., 2003). Similar behavior has also been reported for African savanna (Scholes and Walker, 1993). Other tower measurements conducted in Alaska show a decrease from 0.09 to 0.07 and 0.19 to 0.05 for black spruce and tundra ecosystems,

respectively (Chambers et al., 2005). This is also consistent with values of 0.05 in Knowles (1993) and 0.08 in Tryhorn et al. (2008). Consequently an albedo of 0.10 is chosen in this study for both forest and plain-like landscapes in order to account for the observed darkening of the land surface.

There are comparatively very few studies about emissivity changes resulting from wildfires. Kremens et al. (2003) experimentally derived a land-cover dependent emissivity, corresponding to no change for bare soil and an increase from 0.75 to 0.90 for grass. In our study, we choose a value of 0.95 to account for such small increase with respect to non-burnt land cover.

Burnt vegetation leads to a massive destruction of leaves, which in turn has an important impact on plant evapotranspiration. The atmosphere then absorbs less moisture and the Bowen ratio rises. We will consider for the purpose of our experiment that all the hydrological processes related to the vegetation mantle are nearly stopped, and we associate a leaf area index (LAI) value of 0.10 for all modified land-covers. This is consistent with the study of Californian chaparral response to wildfire held by McMichael (2004), in which it is considered that the LAI is near-zero after burning and recovers pre-fire values in the lapse of ten years. Additionally, in order to stop the vegetation-related hydrological processes taking place right after the fire, we choose very high values of stomatal resistance, radiation stress factor and coefficient for water vapor deficit, which induces extremely low transpiration in our numerical simulations. Furthermore, the low evapotranspiration means that when a precipitation event occurs, the water can go deep within the soil without being pumped out by vegetation processes.

To our knowledge, the modification of aerodynamical properties of the land surface is not thoroughly discussed in the literature. Experimental studies over Australian savanna showed very low increase in roughness length, from 0.46 m for unburnt savanna to 0.49 m for the burnt site (Wendt et al., 2007). In boreal regions, a 7-8 fold decrease in roughness length is observed for burnt forest (from 0.70 to 0.09 m) and a 4-fold decrease for tundra (from 0.04 to 0.01 m) (Chambers et al., 2005). Some land-cover classifications incorporating burnt scars show the same decrease in roughness length, an example of these would be CORINE with a 0.75 m value for broad-leaf forests to 0.50 m for the land-cover cluster of burnt areas, green urban areas and transitional woodland/shrubland. The same tendency to lowering roughness length can be found in already existing numerical studies. While some researchers implement a time and fire intensity dependent change in roughness length, with quasi-complete removal of roughness for highly energetic fires to a small decrease for low intensity events (Görgen et al., 2006), others impose a constant roughness for all fire events. For example in Tryhorn et al. (2008) a change from 2.65 to 0.10 m was chosen. For the purpose of our study, we chose to halve the roughness length. This allows variability according to initial land cover.

4.2.4 Soil temperature and moisture initial conditions in WRF "FIRE" simulations

The release of heat from the combustion alters the water content and temperature of the shallowest layers of the soil. To account for this we choose an initial soil moisture of 0.05 $m^3.m^{-3}$ for the first land-surface

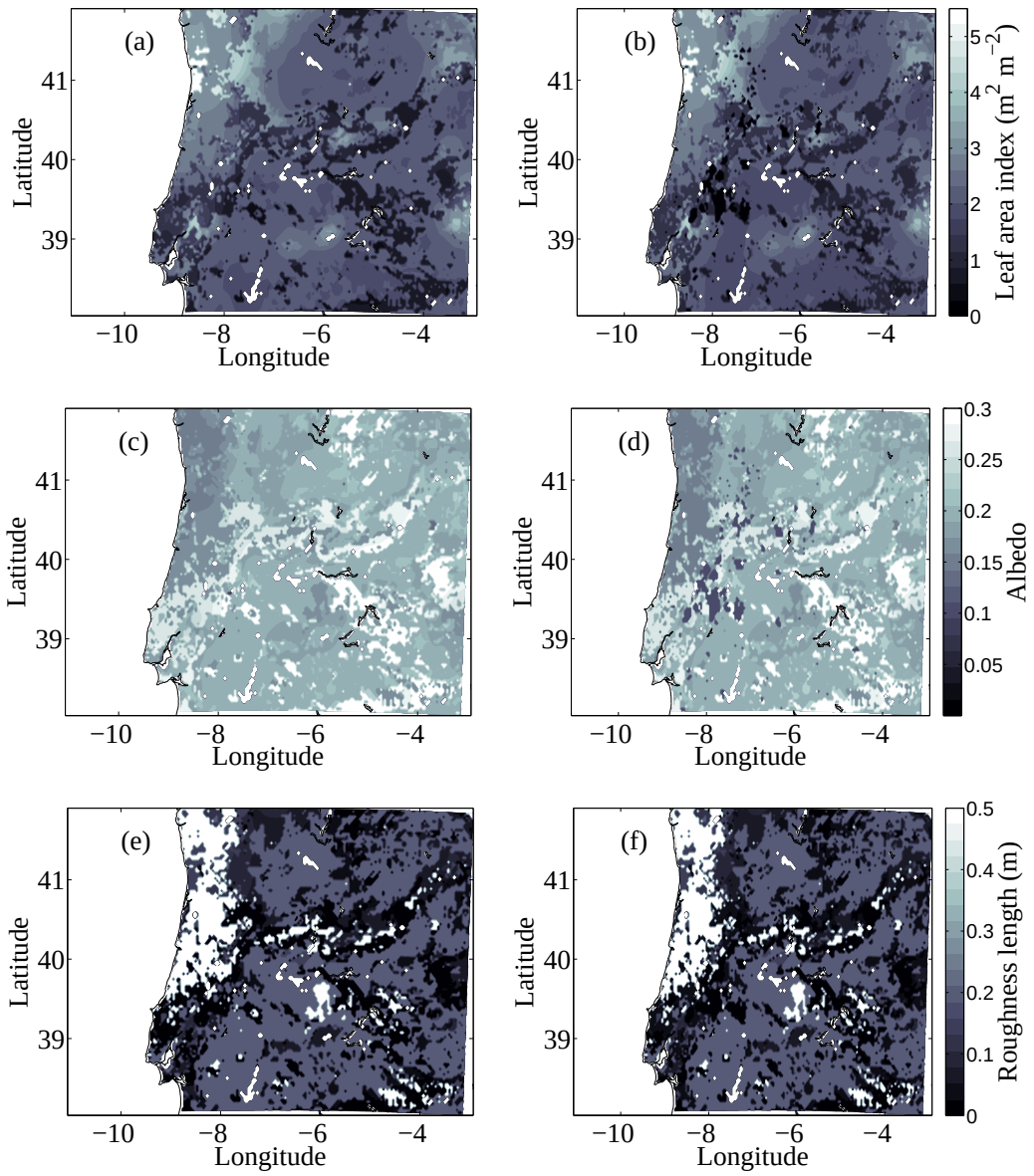

FIGURE 4.4: Maps of leaf area index (a,b), albedo (c,d) and roughness length (e,f). The left column is for the reference simulations (REF) at 3.5km, the right one for all the FIRE simulations at 3.5km resolution.

model (LSM) layer, relatively small compared to the average value of 0.15 $m^3.m^{-3}$ available from ERA-Interim for the domain and time span of interest. This value is consistent with precedent studies (Görgen et al., 2006, Mölders and Kramm, 2007). The choice of initializing soil moisture at a value that does not depend on the local fire intensity and the pre-fire state of the ground is an approximation. The modification of soil temperature is more complex to take into account since it does not last long after the wildfire (Mölders and Kramm, 2007). We chose an extreme initialization with an increase of 300 K of the temperature of the first LSM layer for burnt area, as if all area was burnt at the same moment

land-cover	Status	Sh	N	RS	RGL	HS	LAI^{min}	LAI^{max}	ε^{min}	ε^{max}	α^{min}	α^{max}	Z_0^{min}	Z_0^{max}
Dryland cropland and pasture	Initial	.80	3	40.	100.	36.25	1.56	5.68	.920	.985	.17	.23	.05	.15
	Burnt	.01	3	999.	999.	999.0	0.10	0.10	.950	.950	.10	.10	.025	.025
Cropland/woodland mosaic	Initial	.80	3	70.	65.	44.14	2.00	4.00	.930	.985	.16	.20	.20	.20
	Burnt	.01	3	999.	999.	999.0	0.10	0.10	.950	.950	.10	.10	.10	.10
Mixed Shrubland/Grassland	Initial	.70	3	170.	100.	39.18	0.60	2.60	.930	.950	.22	.30	.01	.06
	Burnt	.01	3	999.	999.	999.0	0.10	0.10	.950	.950	.10	.10	.005	.005
Burnt unspecified soil	Burnt	.01	1	999.	999.	999.0	0.10	0.10	.950	.950	.10	.10	.01	.01

TABLE 4.2: Changes on land-cover parameters operated in all FIRE simulations. Sh is the green vegetation fraction, N is the number of vegetation root levels, RS is the stomatal resistance (sm^{-1}), RGL is a parameter used in radiation stress function, HS is a parameter used in vapor pressure deficit, LAI^{min} is the minimal leaf area index in the year, LAI^{max} the maximum, ε^{min} is the minimum emissivity, ε^{max} the maximum, α^{min} the minimum albedo, α^{max} the maximum, Z_0^{min} the minimum roughness length and Z_0^{max} the maximum.

preceding the simulation. The meteorological impact of such a high-scale high-amplitude modification is presumed to be an upper bound of the actual effect of soil temperature modification in the post-fire period.

The evolution of the albedo, roughness length and vegetative parameters is not considered for this study since our simulations are made over one month and the vegetation recovery process takes years. Soil temperature and moisture are initialized at previously discussed values and their evolution is calculated by the model with respect to atmospheric and soil heat and water transport. Table 4.2 summarizes the changes made on the land-cover and shown in Fig. 4.4.

4.2.5 Synoptic conditions during the simulation period

The time period during which the numerical simulations are conducted extends from 1 to 31 August 2003. One of the most intense heat waves known in Southern Europe occurred during that summer, with an important blocking of a mid-latitude high causing weak wind, high temperatures and drought. The heat wave starts on August, 2 and ends on August, 16 and includes 12 days exceeding the 99th percentile of the 1950-2009 period (Stéfanon et al., 2012a). The temperature anomaly pattern of the 2003 heatwave was very similar to the "Western Europe" pattern, as classified in Stéfanon et al. (2012b). After mid-August, the synoptic atmospheric circulation transitioned to a more classical west-flux synoptic flow. In the following, a distinction will be made between these two time periods and they will be referred as period P1 and period P2, respectively.

4.3 Fire impact in 14-km resolution simulations

The changes of our surface boundary condition modify significantly the energy budget in all our simulations. Figure 4.5 shows the time evolution of the sensible heat flux, evaporative fraction, 2-m temperature, 10-m wind speed, downward solar flux at the surface and precipitations throughout August

averaged over the large patches (4700 km^2). The results for the smaller patches (1800 km^2), being qualitatively similar to those of the large patches, are not shown here. First, changing the surface properties increases the sensible heat flux (Fig. 4.5a) and decreases the latent heat flux and the evaporative fraction (Fig. 4.5b). The time evolution of the downward solar flux shows sequences of different behaviors corresponding to the two different synoptic conditions (Fig. 4.5e). During the first two weeks of August which correspond to the strong anticyclonic condition associated with the summer heatwave, the downward solar radiation averaged between 1400 and 1600 UTC is high ($\simeq$ 880 W.m^2) and quasi constant with time. During the last two weeks of August, the westerly flow conditions bring moisture and synoptic perturbations associated with clouds over Portugal which produce larger temporal variability of the downward solar radiation. The sensible surface heat flux responds directly to the incoming downward solar radiation, so its temporal variability is strongly correlated to that of the downward solar radiation (Fig. 4.5a), whereas its amplitude is modulated by the surface properties. However, one can note that the first hours of the FIRE-ST-14 simulation differ significantly from the other simulations. During the first hours of the FIRE-ST-14 simulation, the sensible heat flux decreases from 600 W m^{-2} to 500 W.m^{-2}, which remains approximately constant until mid August, as for FIRE-MT-14 simulation. Therefore we call P1a the first 72 hours of August, P1b the time period ranging from 6 to 13 August during which the afternoon temperatures reach values as high as 39°C (anticyclonic conditions) and P2 the period between 15 and 31 August corresponding to the westerly flux situation.

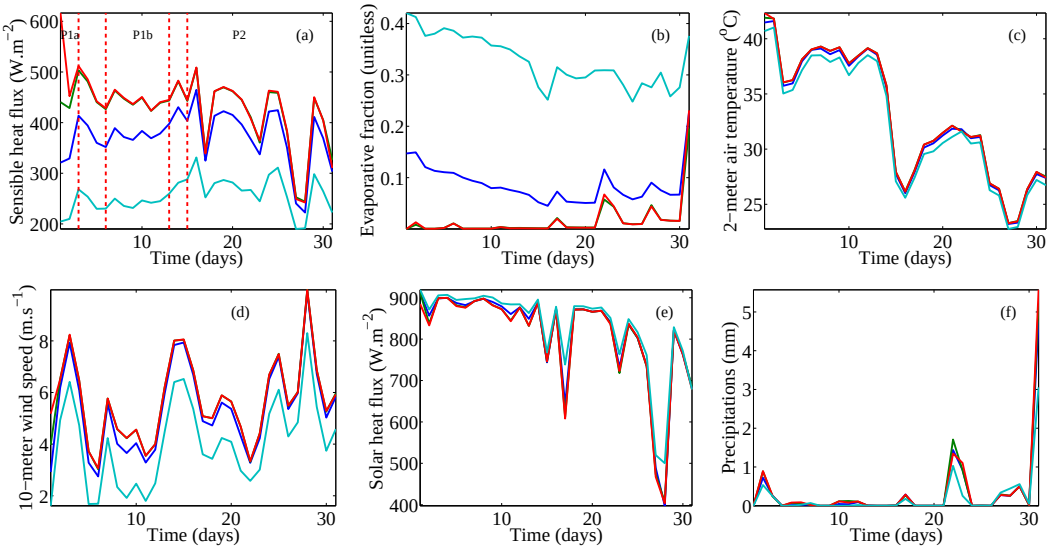

FIGURE 4.5: Monthly history of meteorological parameters above the large burnt patch at a 14km resolution during August. (a) is the sensible heat flux between 1400 UTC and 1600 UTC, (b) is the evaporative fraction on the same period, (c) is the 2-m air temperature on the same period, (d) is the module of 10-m wind speed between 1400 UTC and 1600 UTC, (e) is the downward shortwave heat flux between 1400 UTC and 1600 UTC and (f) is the daily precipitation anomaly with respect to the reference simulation REF-14. For (a) to (e), cyan is for REF-14, blue is for FIRE-LT-14, green is for FIRE-MT-14 and red is for FIRE-ST-14. For (f), blue is for FIRE-LT-14 - REF-14, green is for FIRE-MT-14 - REF-14 and ref is for FIRE-ST-14 - REF-14.

4.3.1 Analysis of P1a

Period P1a corresponds to the period of time where the effect of an initial extremely hot soil layer (i.e. situation that mimics the very short term impact after the end of the fire) is significant with respect to the case of significant soil moisture deficit only (i.e. situation that mimics the medium term impact after the end of the fire). We thus only compare here simulation FIRE-ST-14 with simulation FIRE-MT-14. The initial steep rise of the sensible heat flux corresponds to the spin-up which peaks after few hours to about 600 W.m^{-2}, i.e. 120 W.m^{-2} larger than in FIRE-MT-14 (Fig. 4.6a). This causes the near surface air temperature to rise significantly up to 14 K warmer than in FIRE-MT-14 (Fig. 4.6b).

The temperature difference between FIRE-ST-14 and FIRE-MT-14 is mainly seen at night, when it is mainly controlled by the release of heat from the hot first soil layer which becomes weak after about 70 hours (Fig. 4.6c). Indeed considering that surface heat flux balances the surface longwave radiative heating at night, a difference of about 100 W.m^{-2} during the first hours of the simulations (Fig. 4.6a) is consistent with a near surface temperature difference of 14 K (Fig. 4.6b), according to Stefan-Boltzmann law. Let us now assume that δT is the temperature anomaly and T_0 the homogenous and constant background soil temperature. At $t = 0$, δT = +300 K. The thermal diffusion equation writes:

$$\frac{\partial(\delta T + T_0)}{\partial t} = k\frac{\partial^2(\delta T + T_0)}{\partial z^2}$$

where k is the heat diffusivity coefficient. Let us consider silty clay loam which corresponds to the dominant soil type in our simulations so that $k = 2 \times 10^{-6}\ m^2\ s^{-1}$. A dimensional analysis of this equation gives:

$$\frac{\delta T + T_0}{\tau} = \frac{k}{\Delta_e^2}(\delta T + T_0)$$

where τ is characteristic response scale, Δ_e an effective depth of heat transport. This leads to $\tau = \Delta_e^2/k$. For $\Delta_e = 38$ cm which is a value consistent with the depth of the first two soil layers of WRF land-surface model NOAH, $\tau = 20$ hr. This response time value is consistent with the exponential decay of the nighttime near surface air temperature (Fig. 4.6b) and soil temperature (Fig. 4.6c). At night, a near-surface temperature difference of 14 K between FIRE-ST-14 and FIRE-MT-14 simulations lead to strongly convective conditions at night in FIRE-ST-14 compared to slightly stable conditions in FIRE-MT-14. This leads to a very deep nighttime planetary boundary layer in FIRE-ST-14 with respect to FIRE-MT-14. Indeed, Fig. 4.6d shows that the nighttime planetary boundary layer depth is about 2000 m deeper in FIRE-ST-14 simulation than in FIRE-MT-14 simulation. The time evolution of the PBL depth as a function of the potential temperature vertically averaged over the PBL depth θ is given by:

$$\frac{\partial z_i}{\partial t} = \frac{1}{\gamma}\frac{\partial \bar{\theta}}{\partial t}$$

where γ is the local potential temperature lapse rate above the PBL top. Considering a constant lapse rate, integrating the equation between night and day and differentiating between the two simulations, we

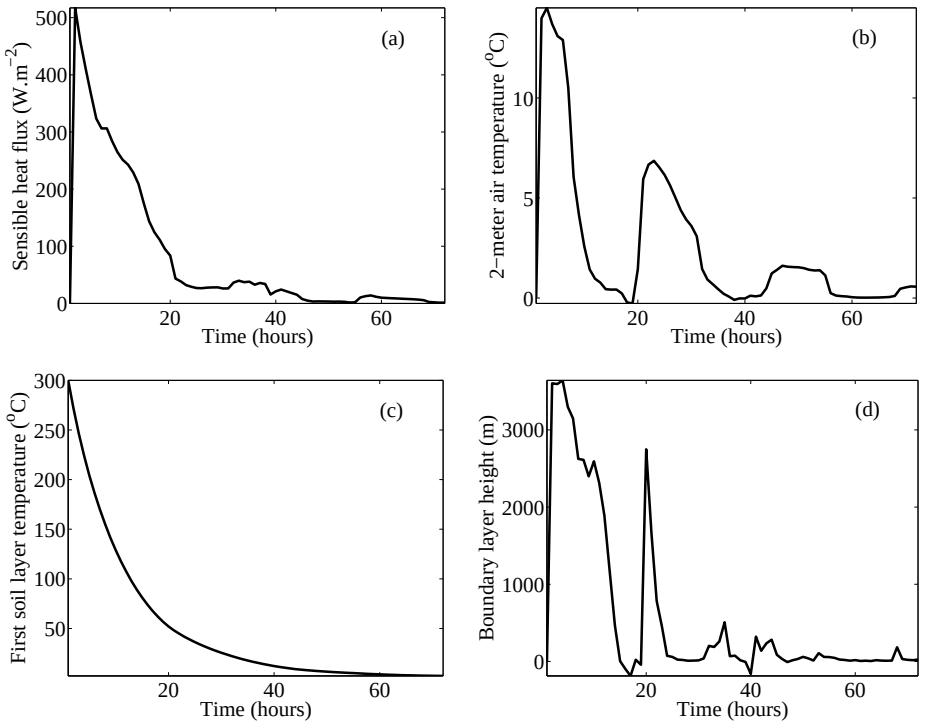

FIGURE 4.6: Difference between FIRE-ST-14 and FIRE-MT-14 simulations for sensible heat flux (a), 2-m air temperature (b), temperature of uppermost soil layer (c), and PBL depth (d) averaged over the large burnt patches during the first three days of the simulations performed at 14 km resolution.

obtain:

$$\Delta z_i^{day} - \Delta z_i^{night} = \frac{1}{\gamma}\left(\Delta\theta^{day} - \Delta\theta^{night}\right)$$

From Fig. 4.6b, we have $\Delta\theta^{day} \simeq 0$ K and $\Delta\theta^{night} \simeq 14$ K (in Fig. 4.6b, only the 2-m temperature is shown but the results is still valid for the vertically integrated potential temperature; not shown). With a typical tropospheric lapse rate $\gamma \simeq 7\times10^{-3}$ K.m^{-1}, we have $\Delta z_i^{day} - \Delta z_i^{night} \simeq$ -2000 m, which is consistent with the simulations (Fig. 4.6d). This is possible if daytime solar heating and induced convection in FIRE-MT-14 is strong enough to partially attenuate the very large differences found at night. The large differences at night between FIRE-ST-14 and FIRE-MT-14 simulations quickly disappear as the uppermost soil layer loses its initial additional heat in a matter of days (Fig. 4.6d). However there is a remnant temperature difference of approximately 7 K by the beginning of the fourth day for the uppermost soil layer and this anomaly disappears very slowly by the end of August with an approximate decay time of 100 h. By the end of the month the temperature difference between FIRE-ST-14 and FIRE-MT-14 simulations reaches 0.5 K for the first layer and approximately 1 K for the lower layers. Part of the added energy is therefore stored in the deeper layers of soil and seeps slowly to the atmosphere during the following months. These results are verified for both large and small patches (not shown). This low release of energy is not powerful enough to create significant differences in the atmospheric response but fire-induced soil heating does create long lasting effects on the soil temperature profile.

The atmospheric response to such strong surface heating is illustrated in Fig. 4.7 which displays the mid-boundary-layer vertical wind speed on 1 August. Strong updrafts, with values reaching +1.2 m.s^{-1}, are organized in bands along the dominant direction of the elongated burnt areas. These regions of strong updraft are associated with larger regions of weaker downdrafts. The regions of updrafts correspond to the front of inland breeze which form in response of the very large horizontal differential heating between the burnt and non-burnt regions and converge over the burnt areas (Courault et al., 2007, Drobinski and Dubos, 2009).

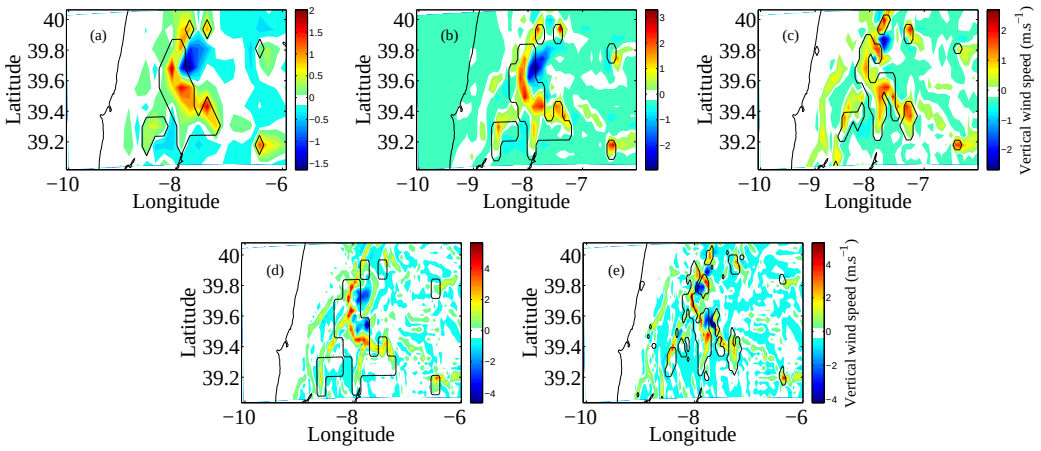

FIGURE 4.7: Mid-boundary-layer vertical wind speed at 1600 UTC for the 1 August 2003 (P1a period) for FIRE-ST-14 (a), FIRE-ST-7-LR (b), FIRE-ST-7-HR (c), FIRE-ST-3.5-LR (d), FIRE-ST-3.5-HR (e). The black contours indicate the limits of the burnt area.

The distribution of the mid-boundary-layer vertical velocity over the large burnt patches is shown in Fig. 4.8a on 1 August 2003. One must have in mind that due to the short duration of P1a period, the number of grid points used to compute the probability density function (PDF) of the vertical velocity is rather low and so only the significant differences are discussed. The REF-14 simulation produces a peaked, narrow and rather symmetric distribution around 0 m.s^{-1}. The standard deviation is 0.13 m.s^{-1}. Such symmetrical PDF suggests the simulation of updrafts and downdrafts associated with PBL shallow convection even though the horizontal resolution of 14 km is the upper limit for their explicit simulation. When the land surface properties are modified to account for the fire occurrence, the PDF becomes asymmetrical and displays positive skewness. With respect to REF-14, the longer the right tail, the larger the number of modified land-surface properties. Indeed, a secondary "peak" is visible around 0.9 m.s^{-1} for FIRE-LT-14, 1.2 m.s^{-1} for FIRE-MT-14 and 1.8 m.s^{-1} for FIRE-ST-14. This persistent updraft associated with the positive vertical velocity corresponds to the updraft produced by convergence of the inland breeze over the burnt area.

Figure 4.9 shows the difference of surface downward solar radiation at 1600 UTC averaged over P1a period between FIRE-ST and REF simulations. It reveals the impact of the mesoscale inland breeze converging over the burnt area on cloud formation. Indeed, there is a significant decrease of surface

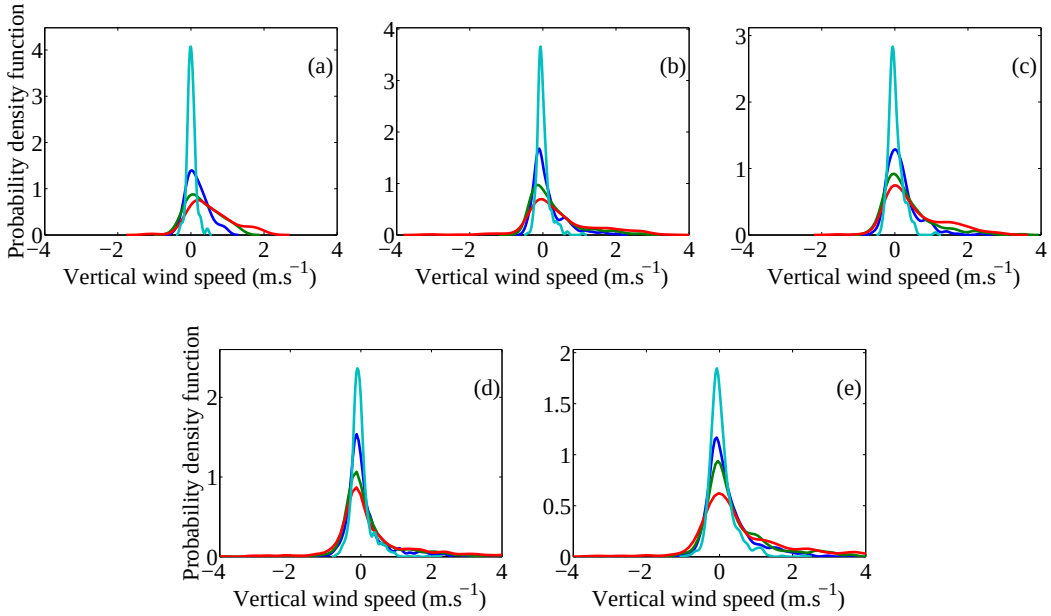

FIGURE 4.8: Probability density functions (PDF) of vertical wind speed above the large burnt patches at $z/z_i = 0.5$ for all grid and land-cover resolutions during the P1a period. Cyan is for REF simulations, blue for FIRE-LT, green for FIRE-MT and red for FIRE-ST. (a) corresponds to FIRE-14 simulations, (b) to FIRE-7-LR, (c) to FIRE-7-HR, (d) to FIRE-3.5-LR and (e) to FIRE-3.5-HR.

downward solar radiation by about 60 W.m^{-2} in FIRE-ST-14 simulation with respect to REF-14 simulation. The radiation anomaly is quasi-perfectly co-located with the burnt areas.

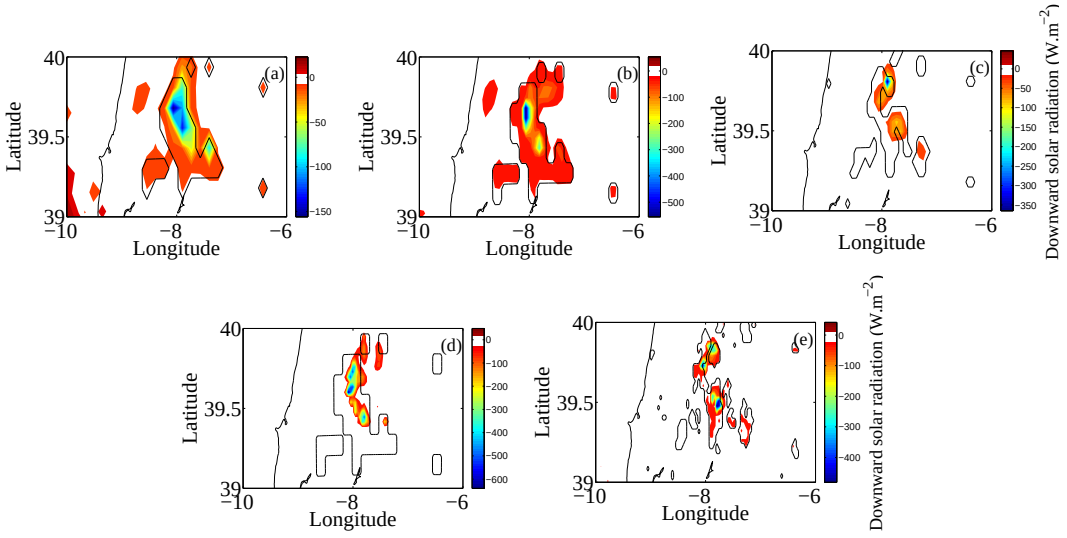

FIGURE 4.9: Difference of surface downward solar radiation at 1600 UTC averaged over the P1a period between FIRE-ST-14 (a), FIRE-ST-7-LR (b), FIRE-ST-7-HR (c), FIRE-ST-3.5-LR (d), FIRE-ST-3.5-HR (e) and REF simulations.

4.3.2 Analysis of P1b

After the first days of the P1 period, referred as period P1a, FIRE-ST-14 and FIRE-MT-14 become very similar and therefore only the FIRE-MT-14 simulation will be discussed. The horizontal pattern of mid-boundary-layer vertical velocity is shown in Fig. 4.10 on 11 August 2003, during the P1b period. The pattern is similar to Fig. 4.7, with updrafts in the middle of the burnt area organized in bands along the elongated burnt area. The updrafts are about 3-4 times weaker than during period P1a (about 0.5 m.s^{-1}). This is due to the much lower sensible heat fluxes over the burnt areas which thus produce weaker horizontal differential heating between the burnt and non-burnt regions and thus weaker inland breezes and convergence. One can note a long elongated band of inland upward motion at about 50 km form the coast. This corresponds to the sea-breeze front, the magnitude of which is similar to the inland breeze convergence over the burnt area. In Fig. 4.7, the sea-breeze front was less visible because it was of much smaller magnitude than the fronts produced over the burnt areas.

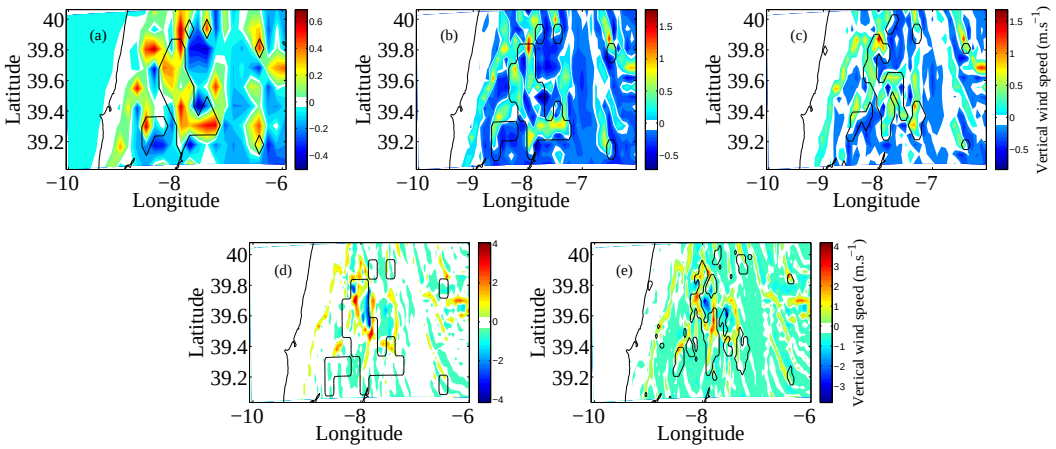

FIGURE 4.10: Same as Fig. 4.7 for 11 August 2003 (P1b period).

To compare the simulated wind convergence over the burnt area in FIRE-MT-14 and FIRE-LT-14 with respect to REF-14, the PDF of the mid-PBL vertical velocity are displayed in Fig. 4.11. Since the surface sensible heat flux is larger in FIRE-LT-14 and FIRE-MT-14 with respect to REF-14, the PBL depth is deeper. Indeed, the average PBL depth above the large patch around 1600 UTC is 4000 m in FIRE-MT-14 and FIRE-ST-14, 3800 m for FIRE-LT-14 and 3250 m for REF-14. Between periods P1a and P1b, only the PDFs computed from FIRE-ST-14 simulation differ significantly. The PDFs computed from the other simulations are nearly identical, the PDFs computed for period P1b being much better sampled than for period P1a. This shows that the synoptic situation remains the same for the two periods. During period P1b, the PDFs computed from FIRE-ST-14 and FIRE-MT-14 simulations are not distinguishable, therefore showing the absence of long-term impact of the initial very hot soil on the atmospheric circulation. The long right tail of the PDF from FIRE-ST-14 is shorter for period P1b than for period P1a advocating for a weakening of the inland-breeze circulation converging over the

burnt areas due to the weaker differential heating between the burnt and non-burnt areas. As for period P1a, the PDFs of FIRE-ST-14, FIRE-MT-14 and FIRE-LT-14 simulations are wider than the PDF from REF-14 simulations. It is not only true because of the presence of breeze circulations which generate the positive skewness but also because of more powerful thermals caused by larger sensible heat flux which also enlarge the symmetric part of the PDF around 0 m.s^{-1} (see left part of the PDF). For a more

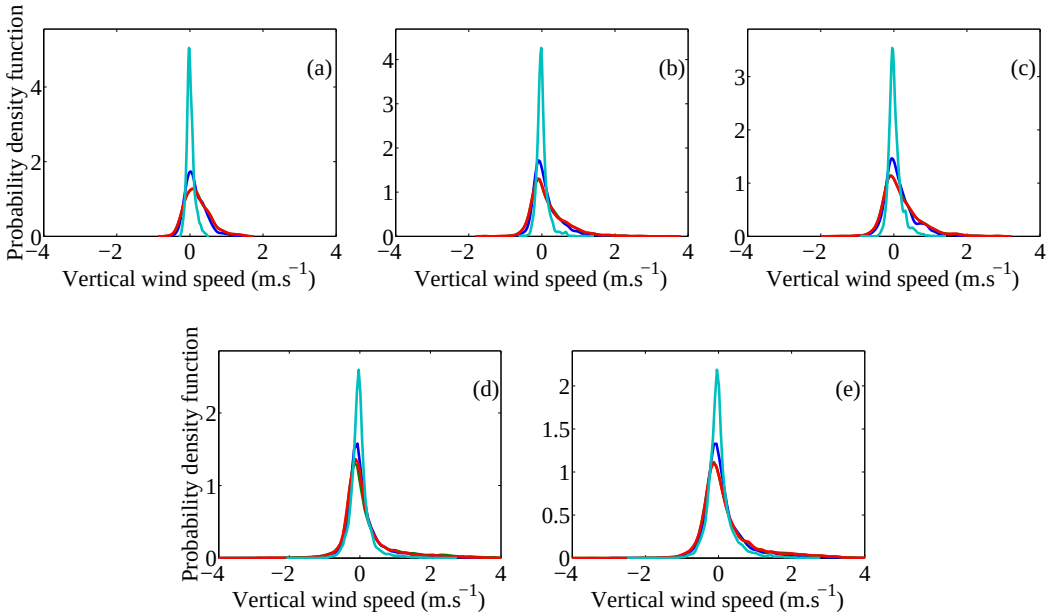

FIGURE 4.11: Same as Fig. 4.8 for the P1b period (the FIRE-ST and FIRE-MT curves are not distinguishable).

quantitative analysis, let us consider that the PDFs are a sum of the contributions of the thermals and the mesoscale inland breeze circulations, and that the PDF p of the mid-boundary-layer vertical velocity can be modeled as

$$p(w) = a_1 \exp\left(-\frac{w^2}{\sigma_1^2}\right) + a_2 \exp\left(-\frac{(w-\mu_2)^2}{\sigma_2^2}\right) \tag{4.1}$$

The first zero-mean Gaussian distribution is associated with the thermals and the second Gaussian distribution with the mesoscale convergence. In order to compare the relative weight of the two Gaussian distributions, we consider $\omega_2 = \frac{a_2\sigma_2}{a_1\sigma_1+a_2\sigma_2}$. We assume that σ_2 represents the breeze-induced vertical wind speed variability and μ_2 its mean. Table 4.3 shows these parameters computed over the large burnt patches for all simulations. The values computed for period P1a are less accurate because of the limited number of samples (3 days only). Compared to REF-14 simulation, all FIRE simulations exhibit larger σ_1 values (twice as large for FIRE-LT-14 simulation and three times larger for FIRE-MT-14 and FIRE-ST-14 simulations). The parameter σ_1 is a good proxy of the strength of the thermals produced by convection. We can also see that the parameters relative to mesoscale breeze convergence increase between FIRE-LT-14 and FIRE-MT-14 (and FIRE-ST-14). Not only the strength of the updraft at the convergence location increases with $\mu_{2,LT}$=0.35 m.s^{-1} for FIRE-LT-14 simulation and $\mu_{2,MT}$=0.44 m.s^{-1})

Period	Simulation	ω_2 (%)	σ_1 ($m\ s^{-1}$)	σ_2 ($m\ s^{-1}$)	μ_2 ($m\ s^{-1}$)
P1a	REF-14	(none)	0.13	(none)	(none)
	FIRE-LT-14	40	0.27	0.40	0.37
	FIRE-MT-14	51	0.36	0.64	0.59
	FIRE-ST-14	69	0.34	0.92	0.51
P1b	REF-14	(none)	0.12	(none)	(none)
	FIRE-LT-14	37	0.22	0.31	0.35
	FIRE-MT-14	41	0.29	0.40	0.44
	FIRE-ST-14	41	0.28	0.39	0.44
P2	REF-14	(none)	0.06	(none)	(none)
	FIRE-LT-14	42	0.08	0.12	0.10
	FIRE-MT-14	44	0.09	0.21	0.12
	FIRE-ST-14	44	0.09	0.17	0.12

TABLE 4.3: Coefficients of the gaussian decomposition of the mid-boundary-layer probability distribution functions. Results are for the large patch at 14 km grid resolution only.

for FIRE-MT-14 and FIRE-ST-14 simulations, but its variability also. Indeed, σ_2 increases by a factor 1.6 and 2.3 with respect to FIRE-LT-14 for FIRE-MT-14 and FIRE-ST-14 simulations, respectively.

The impact of the breeze convergence over the burnt area on the PBL structure and dynamics is illustrated in Fig. 4.12. Indeed, due to larger surface sensible heat flux and stronger thermals, the PBL is warmer and deeper in FIRE-LT-14 and FIRE-MT-14 simulations. Figure 4.12 shows that the PBL in FIRE-MT-14 simulation deepens more quickly than in REF-14 simulation and the maximum difference is about 1800 m and is reached around 1200 UTC, which corresponds approximately to 1200 local solar time. The warmer PBL in FIRE-MT-14 simulation generates mesoscale inland breeze which converge over the burnt patches as shown in Fig. 4.10 for one instant on 11 August 2003. Figure 4.12a displays the wind divergence averaged over the large burnt patches and over period P1b. We clearly see wind convergence (negative values) in the first levels of the PBL up to 1000 m height at 1600 UTC, and wind divergence (positive values) at the PBL top. Wind convergence displays a pronounced diurnal cycle, with nearly no low level convergence/upper level divergence at night, and low level convergence/upper level divergence in phase with the evolution of solar radiation, with a maximum reached at 1200 UTC. The depth of the low level convergence increases as the PBL deepens and the altitude of the upper level divergence follows the evolution of the PBL top. The enhanced low level convergence is associated with stronger wind speed over the burnt area by about 2 $m.s^{-1}$ and slightly lower wind speed at the height of the upper level divergence (Fig. 4.12b). The stronger low level jet is caused by both the reduced roughness length caused by vegetation burning and by the inland breeze system due to enhanced surface sensible heat flux over the burnt area. For relative humidity (Fig. 4.12c), the dilution effect by turbulent mixing adds up to the reduced and evapo-transpiration in FIRE-MT-14 simulation to generate a dryer PBL with respect to REF-14 simulation. However, at the PBL top, the relative humidity is higher by 20% above the large patches (8% above the smaller patches) in FIRE-MT-14 simulation with respect to REF-14 simulation. The physical explanation of this behavior comes from an interplay of the effect of reduced evaporation, that tends to reduce relative humidity, and of entrainment of cold air from the boundary layer top that can increase it by lowering the saturation threshold. The value of the relative humidity at the PBL top in REF-14 simulation is about 60% (not shown). Under conditions of low instability, the second effect

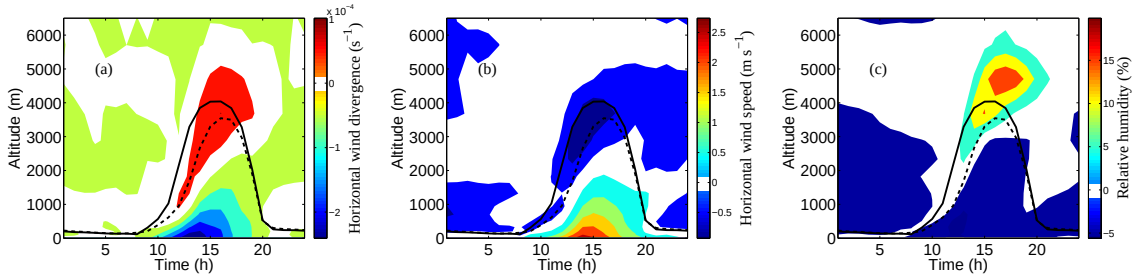

FIGURE 4.12: Diurnal cycle of the difference between FIRE-MT-14 and REF-14 simulations for wind divergence (a), wind speed (b) and relative humidity (c) averaged over the large burnt patches and over period P1b. The solid and dashed black lines display the mean PBL depth in FIRE-MT-14 and REF-14 simulations, respectively.

prevails, and the air column is in a regime of so-called dry advantage and shallow clouds can be favored (Ek and Holtslag, 2004, Gentine et al., 2013, Stéfanon et al., 2014). Indeed, the downward shortwave radiation is slightly weaker at the surface in the FIRE simulations, as seen in Fig. 4.5e and in Fig. 4.13 which shows the quasi perfect co-location between the burnt patches and the solar radiation anomaly.

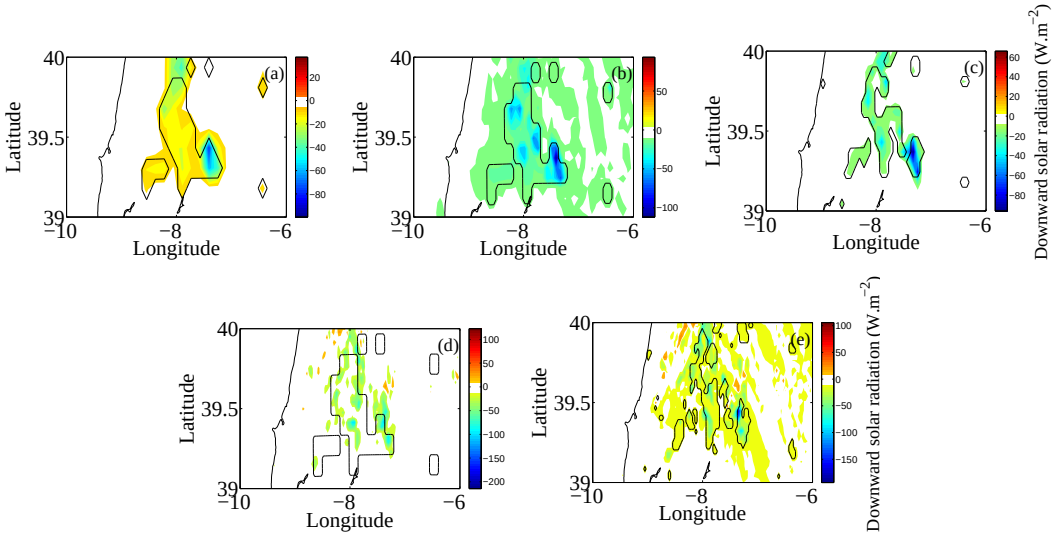

FIGURE 4.13: Same as Fig. 4.9 for P1b.

4.3.3 Analysis of P2

During P2 period, the synoptic westerly flow interacts with the thermally induced mesoscale circulation. As the westerly flow blows in the same direction as the sea-breeze, it advects cold air over land and thus inhibits the rise in the temperature. The sea-breeze flow weakens with the temperature gradient, but even if the onshore-synoptic wind induces weaker sea breeze, the resulting flow is slightly stronger (Bastin et al., 2005, Drobinski et al., 2006, Estoque, 1962). Figure 4.14 illustrates the absence of sea-breeze front on 20 August 2003, during P2 period because of the westerly flow. Over the burnt patches, the low

level convergence is also weakened but still visible with updrafts reaching 0.25 m.s^{-1}, i.e. about four times weaker than during P1a period (Fig. 4.7) and two times weaker than during P1b period (Fig. 4.10).

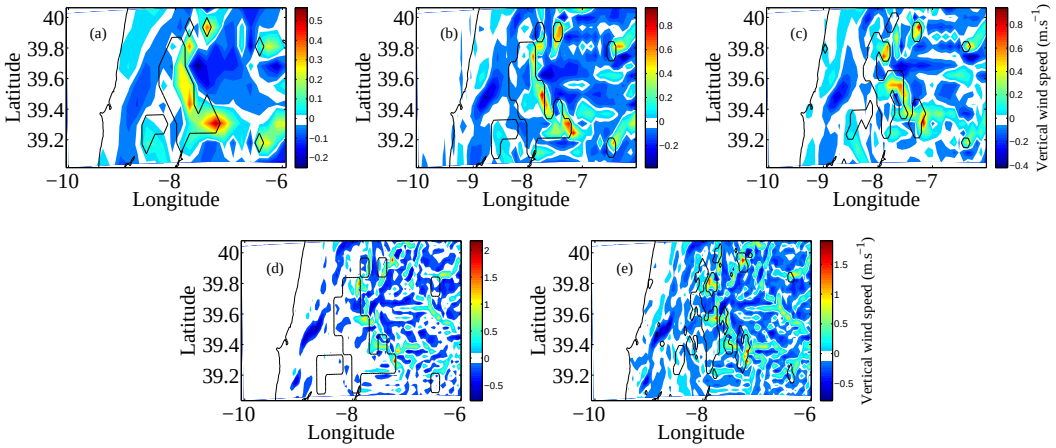

FIGURE 4.14: Same as Fig. 4.7 for 20 August 2003.

This is visible in the PDFs of the vertical velocity over the burnt area in Fig. 4.15. The PDFs from FIRE simulations are much narrower for P2 period than those computed for P1a and P1b periods (Table 4.3).

During P2, the temperature is lower than during the heat wave and the synoptic conditions induce a westerly flow regime. In this weather regime, the boundary layer is shallow and peaks at approximately 2000 m versus 4000 m during P1b. The thermals are weaker (Table 4.3), therefore the relative humidity anomaly between FIRE-MT and REF is lower (+8% during P2 period above the large patch, versus nearly +20% during P1b period with a background humidity of 75% in REF simulation) (Fig. 4.12). The convergence of surface winds is also lower confirming the weaker vertical velocities over the burnt patches. However the higher background mean relative humidity, brought from the Atlantic ocean by the westerly winds, brings additional cloudiness and a succession of positive rain anomalies during P2, which we will study in the following paragraphs. Albeit lower, the surface horizontal wind convergence still brings moisture from the non-burnt surrounding lands to above the atmospheric boundary layer.

Clouds identified in Fig. 4.16 with negative downward solar radiation anomalies, are either transported away by the westerly winds or trigger precipitation. Therefore precipitation events are more intense above both large (Fig. 4.5f) and smaller patches (not shown). The precipitation excess above the burnt area can reach values of 0.7 to about 2 mm during P2, for total precipitations of about 9 mm. Therefore the precipitation pattern is modified by the burnt area so as precipitations tend to be triggered preferentially above the drier burnt area. This is consistent with the observations of Vidale et al. (1997) made in the boreal region. Knowles (1993) and Pielke et al. (2007) show the cumuli tend to develop downwind of recent burnt areas in boreal forest landscapes. Here since our burnt patches can be large, precipitation tend to occur where mesoscale ascendance occurs, i.e. above the patches.

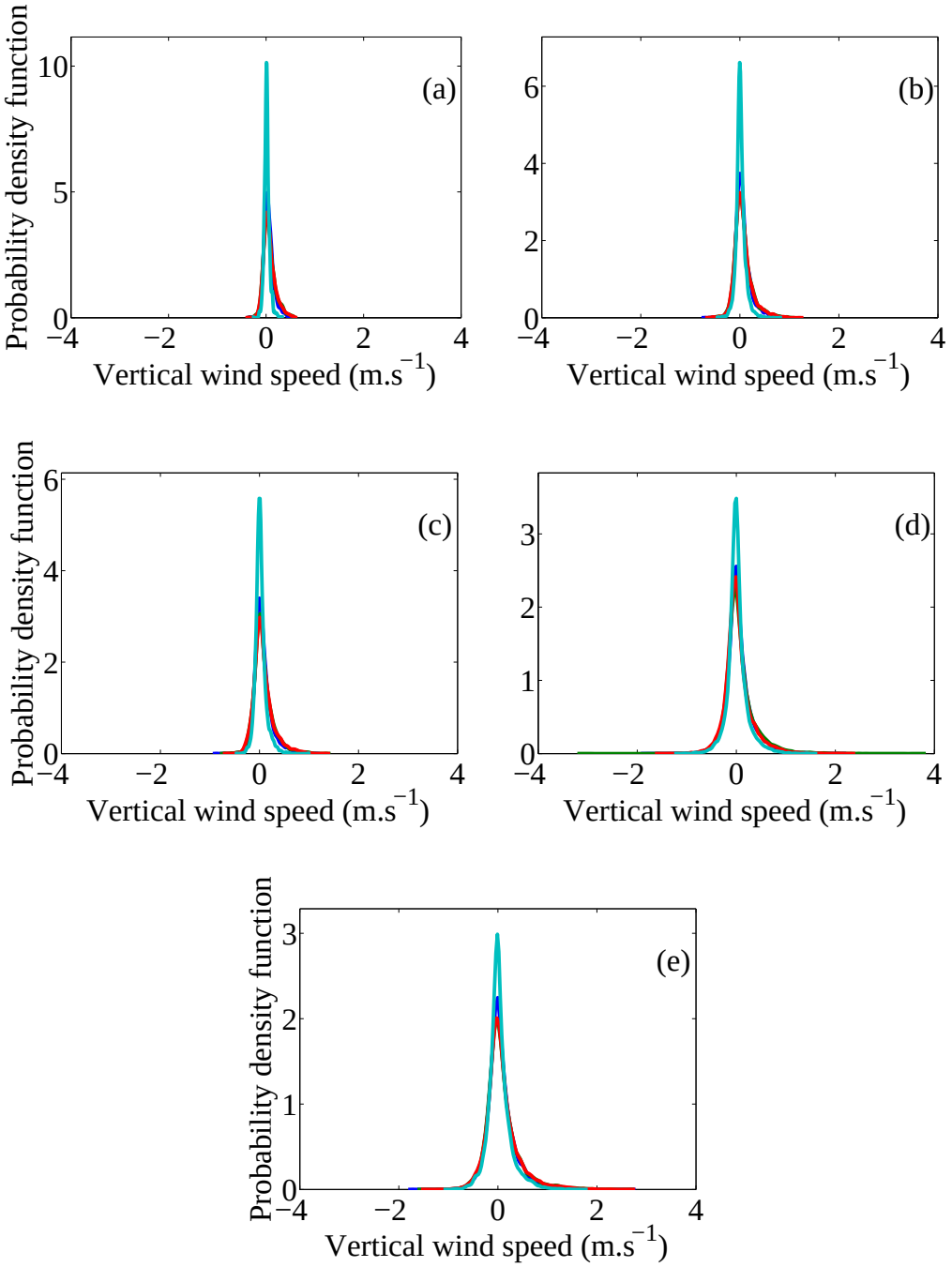

FIGURE 4.15: Same as Fig. 4.8 for P2 period.

4.4 Impact of model and land-cover resolution

In Figs. 4.8, 4.11 and 4.15, FIRE-LR simulations have a 14-km resolved land-cover but finer grid resolutions with respect to REF simulations. The figures show that in all simulations, the vertical wind velocity

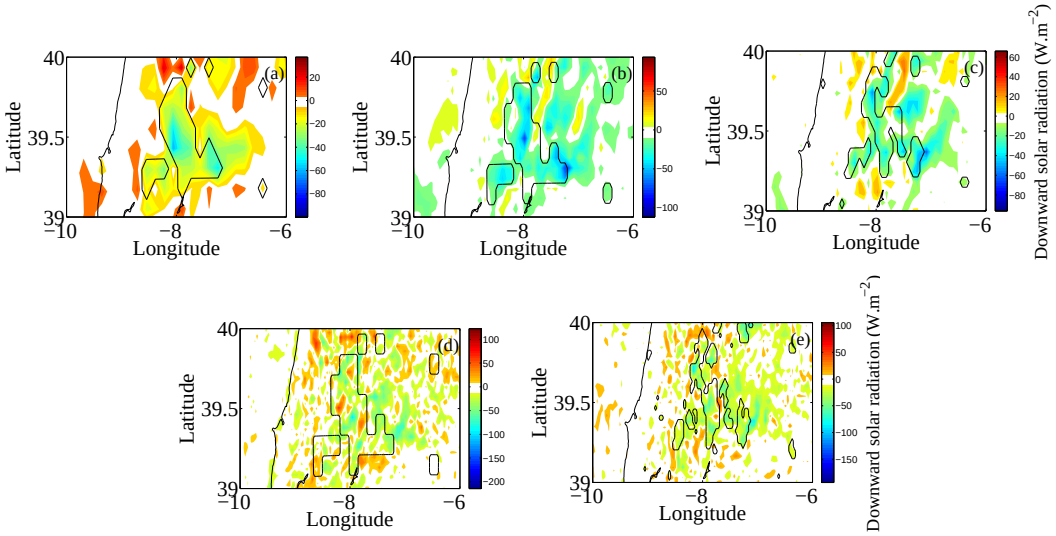

FIGURE 4.16: Same as Fig. 4.9 for P2.

associated with the thermals have a larger standard deviation when the grid resolution is finer. Quantitatively in the REF simulations, the value σ_1 for P1a/P1b/P2b periods is 0.14/0.12/0.05 m.s^{-1} for REF-14 simulation, 0.24/0.17/0.09 m.s^{-1} for REF-7-LR simulation and 0.36/0.27/0.16 m s^{-1} for REF-3.5-LR simulation. There is slightly less than a factor 2 between σ_1 value of REF-7-LR simulation and σ_1 value of REF-14 simulation and slightly less than a factor 4 between σ_1 value of REF-3.5-LR simulation and σ_1 value of REF-14 simulation. This is consistent with the averaging effect of a coarser grid. Indeed, at one grid point of the REF-14 simulation corresponds 4 grid points of the REF-7-LR simulation and 16 grid points of the REF-3.5-LR simulation. If N samples are simulated over the burnt area in REF-7-LR simulation with a standard deviation σ_1, then the N/4 samples simulated over the burnt area in REF-14 simulation have a standard deviation $\sigma_1/\sqrt{(4)}$, which is approximately what we have. So the difference of the vertical velocity PDF widths is mostly due to the averaging effect of the grid mesh. Increasing also the resolution of the land-cover (REF-7-HR and REF-3.5-HR simulations) slightly affects the ratio between the PDF widths with respect to the simulations using a 14-km resolution land-cover (REF-14, REF-7-LR and REF-3.5-LR simulations). Indeed, the value σ_1 is for P1a/P1b/P2b periods is 0.26/0.19/0.09 m.s^{-1} for REF-7-HR simulation and 0.36/0.30/0.19 m.s^{-1} for REF-3.5-HR simulation. The increase of σ_1 with respect to its value for a 14-km resolution land-cover can be attributed to the added variability caused by the higher land-cover variability. It however represents only about 10% of the total variability.

The signature of the mesoscale convergence of over the burnt area due to the differential heating induced by the difference of land properties over the burnt and non-burnt area, is significantly impacted by the resolution. In Figs. 4.8, 4.11, the second peak of the distribution which corresponds to the convergence-induced positive vertical velocities, becomes less distinct as the resolution gets finer. This is explained quantitatively in Fig. 4.17 which displays the behavior of the parameters of Eq. (4.1). Indeed, as for the first mode ("thermal" mode), the width of the second mode ("burnt area" mode) increases as a response

to the finer resolution (including land-cover resolution). The convergence-induced vertical velocity at the inland breeze front increases (i.e. μ_2 increases) when the resolution becomes finer. The finer resolution causes the front to be narrower. Indeed, it is mostly parameterized when the model resolution is 14 or 7 km and the front width thus scales with the model resolution Δ (it is typically 2Δ). At 3.5 km model resolution, the front is explicitly resolved and becomes even thinner. As the resolution gets finer, the horizontal gradients of the horizontal velocities get larger. Mass conservation therefore imposes stronger vertical motion. One can note that μ_2 increases with the model resolution but that for a given model resolution, μ_2 is smaller when a higher resolved land-cover is used. Indeed when the land-cover is provided to the model at 7 or 3.5 km, the burnt area becomes smaller and has a more complex shape with respect to the 14-km resolution land-cover. The smaller size of the burnt area decreases the amplitude of inland breeze produced by the presence of the burnt area, and the more complex shape tends to generate a larger number of converging zone which are no longer concentrated on one single front line. Despite the fact that the convergence-induced vertical velocity increases (i.e. μ_2 increases), the wide two modes seem to merge as we reach 3.5 km resolution. However, all FIRE simulations remain positively skewed in comparison to REF simulations.

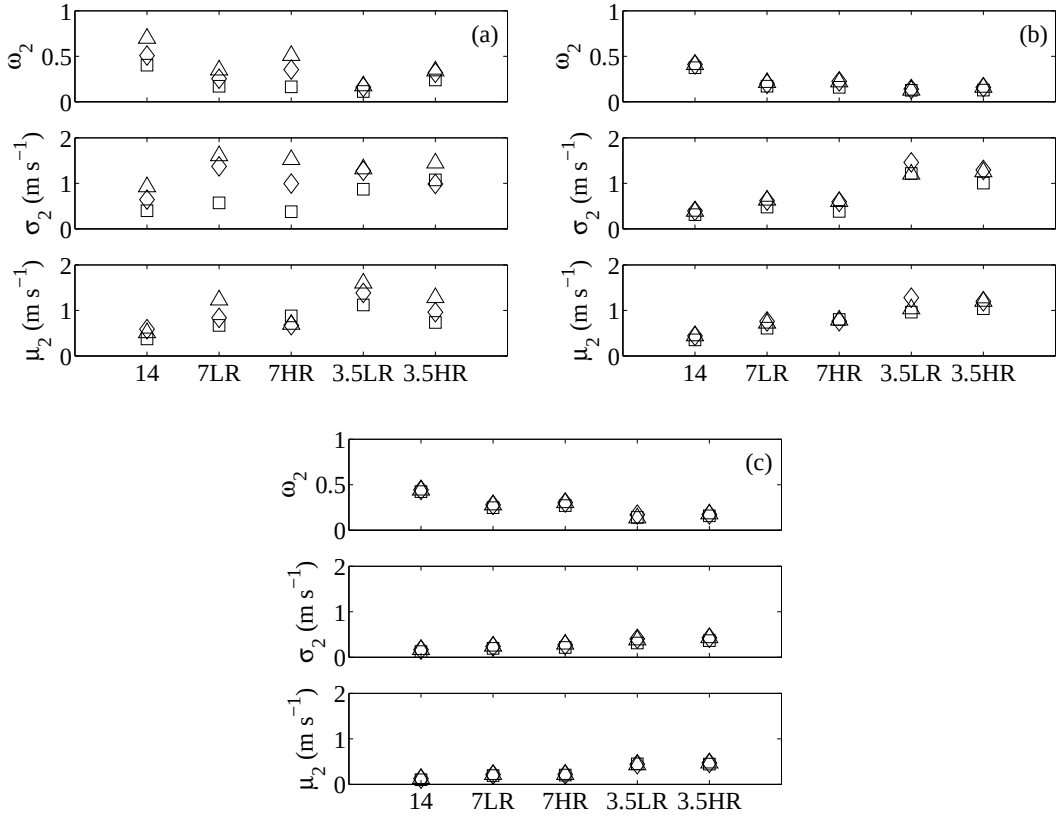

FIGURE 4.17: Relative weight (ω_2), second variability (σ_2; in m.s^{-1}) and second mean (μ_2; in m.s^{-1}) of mid-boundary-layer vertical wind speed. (a,b,c) are for the large patch,. (a) is for P1a, (b) for P1b and (c) for P2. Squares are for FIRE-LT, diamonds for FIRE-MT and triangles for FIRE-ST. Data is taken between 1400UTC and 1600UTC for all the duration of the considered period.

When the model resolution becomes finer ω_2 decreases. The quantity ω_2 represents the relative weight of the second mode representing the burnt area-induced mesoscale convergence to the first mode representing the convection-induced thermals. Geometrically, ω_2 can be interpreted as the ratio of the surface of the burnt area-induced inland breeze front to the total surface of the burnt area. We see in Figs. 4.7, 4.10 and 4.14 that when the model resolution increases, the breeze fronts become thinner as discussed earlier. For a given model resolution, when the land-cover resolution is finer, the burnt area becomes smaller by construction. The dynamics is less impacted by the land-cover resolution than by the model resolution so that the inland breeze fronts occupy less space over the burnt area (Figs. 4.7, 4.10 and 4.14). Therefore ω_2 increases (Fig. 4.17). The width of the second mode, σ_2, increases when the model resolution gets finer up to 2 m s^{-1}, for the same reason given for σ_1. For a given model resolution, the impact of the land-cover resolution on σ_2 is similar to that on μ_2. Even though the behavior of the PDFs parameters with respect to model and land-cover resolution is similar whatever the investigated period, it is more pronounced during P1 period (P1a and P1b with some caution for P1a due to the more limited number of samples used to compute the PDFs) than during P2 period. The presence of the background synoptic wind during P2 tends to damp the amplitude of the differential heating between the burnt and non-burnt areas by the advection of colder marine air masses from the Atlantic Ocean. The behavior of the boundary-layer depth with respect to model and land-cover resolution is strongly correlated to that of the vertical velocity PDFs. The boundary layer depth is shallowest in the REF simulations. It is deeper in FIRE-LT (+600 m in P1a when compared to REF), FIRE-MT (+900 m) and FIRE-ST (+1100 m) simulations.

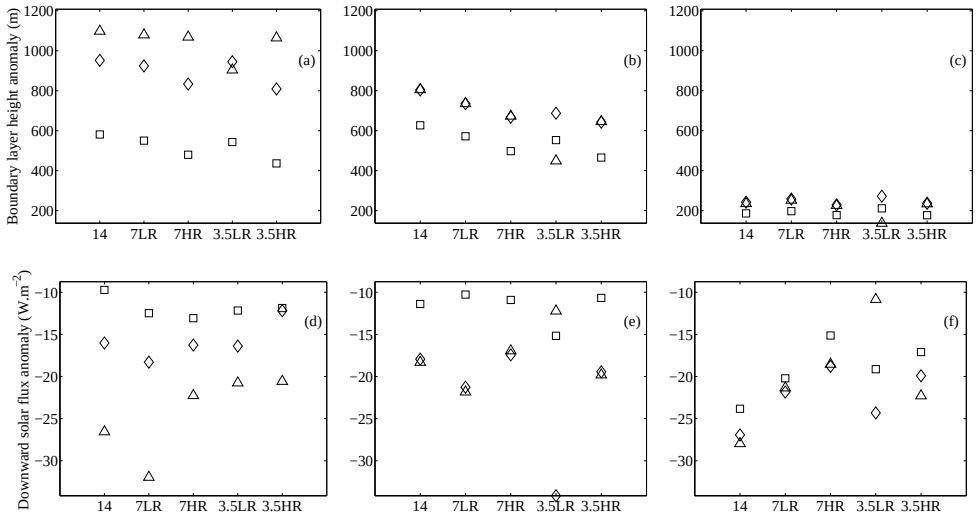

FIGURE 4.18: Boundary layer height (m; upper row) and downward solar flux (W.m^{-2}; lower row) anomalies averaged between 1400 and 1600 UTC over the large patches for period P1a (a,d), P1b (b,e) and P2 (c,f) for all sets of land cover and model resolutions (squares: FIRE-LT - REF; diamonds: FIRE-MT - REF; triangles: FIRE-ST - REF).

The land-cover modifications impact the water cycle. More updrafts bring more cloudiness above the burnt patch where precipitations tend to occur preferentially. A first element of understanding is the level of condensation which is very high in all simulations and its sensitivity to the model or land cover resolutions is weak (not shown). In the REF-simulation, the level of condensation is 3800 m, 3550 m and 2400 m for P1a, P1b and P2 periods, respectively. In FIRE-LT, it reaches 3950 m, 3750 m and 2550 m. Finally in FIRE-MT or FIRE-ST, it is 4000 m, 3800 m and 2550 m. In the FIRE experiments, the boundary-layer depth always reaches values similar to the level of condensation, explaining cloudiness over the burnt patches (Fig. 4.18). For the REF simulation, the boundary-layer depth hardly reaches 2700 m during P1a and 3000 m during P1b, thus explaining the absence of cloudiness (Fig. 4.18a,b,d,e). The already very dry meteorological conditions during the summer heat wave explains the weak sensitivity of the level of condensation to the presence or not of the burnt scar. However, the convergence over the burnt scar has a strong impact on the boundary-layer depth and thus the formation of clouds. During P2, the advection of moist marine air contributes to decrease significantly the level of condensation. The boundary-layer is also shallower. However, its depth is similar to the value of the level of condensation in all simulations, thus explaining the strong decrease of downward solar insolation at the surface (Fig. 4.18c,f). The cloudiness is less sensitive to the model resolution than to the land-cover simulation, and its behavior with respect to the model and land cover resolution is correlated with that of the boundary-layer depth (indeed lower boundary-layer with respect to the level of condensation means lower cloudiness and higher downward solar radiation at the surface). In Fig. 4.18, we see that for a given model resolution, the FIRE simulation performed with a 14-km resolution for the land cover (LR simulations) displays higher cloudiness than the corresponding FIRE simulation with a land cover resolution equals to that of the model (HR simulations). This is due the smaller surface occupied by burnt area in HR simulations with respect to the LR simulations. Therefore, the inland breeze are of smaller size and lower intensity (Courault et al., 2007) (see also Fig. 4.17). The consequence is weaker convergence and updraft above the burnt area, and therefore less clouds. For a given land cover resolution, the higher the model resolution, the stronger the updraft above the burnt area (Fig. 4.17), the larger the cloud cover and the smaller the downward radiation at the surface.

Even though, summer 2003 was very dry, especially in Portugal, there is an interest to look at the precipitation, even weak, that the suite of simulations produce and their anomalies with respect to the REF reference. Indeed, Fig. 4.5 shows a series of weak precipitating events over the burnt area during the whole simulated period. Indeed, due to higher convergence over the burnt areas, the convective air parcels are transport at much higher level, experiencing strong adiabatic cooling which leads to a large relative humidity increase favoring the triggering of precipitation. In Fig. 4.19, we investigate the sensitivity of the simulated precipitation after the fire events with respect to the model and land-cover resolutions. Rain is split into convective (also called parameterized) rain and non-convective (also called explicit) rain. We can first notice the totally different behavior when convection is parameterized (model resolution > 3.5 km) and when it is explicitly resolved (model resolution equals 3.5 km). During P1 period (combining P1a and P1b), no large-scale explicit precipitation are produced by any simulations and

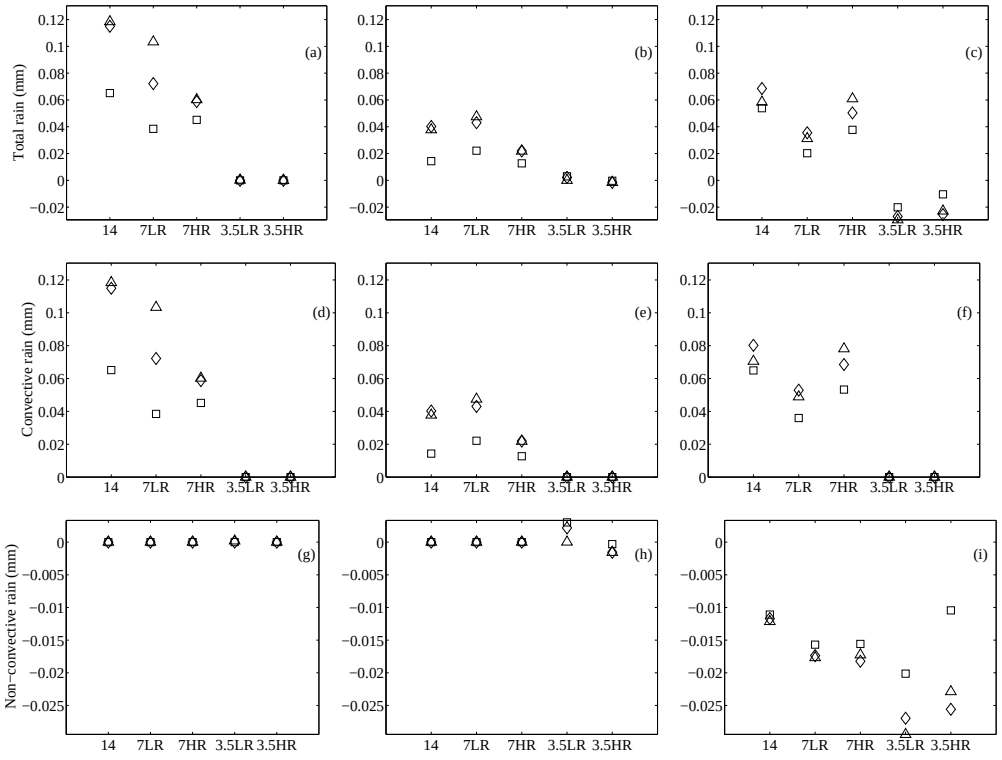

FIGURE 4.19: Total, convective and non-convective precipitation difference with respect to the REF simulation (mm) averaged between 1400 and 1600 UTC over the large patches for period P1a (a,b,c), P1b (d,e,f) and P2 (g,hi) for all sets of land cover and model resolutions (squares: FIRE-LT - REF; diamonds: FIRE-MT - REF; triangles: FIRE-ST - REF).

the precipitation signal only comes from the parameterized convection. Therefore, no precipitation are produced in the FIRE simulations at 3.5 km model resolution (neither in the REF simulation), whereas precipitation are produced in the FIRE simulations at 7 and 14 km model resolutions. With Kain-Fritsch convective parameterization (Kain, 2004), one could expect such a negative feedback loop, generally consistent with explicit simulations Hohenegger et al. (2009). This means that drier soil produces more rain due to enhanced atmosphere instability Hohenegger et al. (2009), Stéfanon et al. (2014) (dry advantage regime). This effect is probably even enhanced because of the breeze induced low level convergence over the burnt patch. Here, the explicit simulations do not produce precipitation at all because of the too dry and hot conditions. During P2 period, the precipitation signal is shared between convective (2/3 of the signal) and non-convective precipitation (1/3 of the signal) (except for the simulations performed at 3.5 km model resolution). As for P1, larger convective precipitation are produced in the FIRE simulations. During P2, large-scale advection of moist marine air in a westerly flow, produces less explicit precipitation in the FIRE simulations, due to higher air temperature over the burnt area which evaporates liquid water in suspension in the air column. This mechanism is more efficient as the model resolution gets finer due to increased dry air entrainment in the stronger updrafts. In total, during P2 period, all

simulations with parameterized convection produce larger precipitation over the burnt area. Conversely, simulations with explicitly resolved convection produce equal or less precipitation over the burnt area. Of course, this result is parameterization dependent but the Kain-Fritsch convective parameterization, which is generally more consistent with explicit simulation, here exacerbates the negative feedback loop.

4.5 Conclusions

Compared to usual land-cover changes like we see for example in deforestation, wildfires bring about more drastic alterations of the land cover. The roughness length is reduced over a burnt area favoring the acceleration of the wind. The darker surface favors downward solar radiation absorption and thus ground heating. This effect is even more pronounced after the wildfire ceases, when the soil moisture has been evaporated enhancing dryness and sensible heat release. Higher sensible heat fluxes over the burnt area produces stronger local convective updrafts. Burnt areas also cause differential thermal heating between the overlying air and that above the preserved surrounding land cover. The contrast in sensible heat flux at the surface between burnt and non-burnt ground creates a convergence area over the wildfire imprint during the day. The converging winds are accelerated by the lower roughness length increasing convergence over the burnt area.

The combination of higher surface heat fluxes, larger differential heating and lower surface roughness produces very intense frontogenesis with vertical velocity reaching few meters per second. This powerful meso-scale circulation can pump more humid air from the surroundings not impacted by the wildfire. This more humid air can be transported at high level in the atmosphere (around 4 km in our simulations). It cools down and can reach saturation, thus generating more cloudiness over the burnt area.

The influence of the age of the burnt scar on the atmospheric response was also investigated. The influence of soil temperature immediately after the wildfire ceases is mainly seen at night as the boundary-layer remains unstably stratified. This effect lasts only few days before the heat is either dissipated in the atmosphere or stored in the deeper layers of soil. Not surprisingly, the warming and drying effect of the wildfire ceases after few weeks. So the intensity of the induced meso-scale circulation decreases with time, even though it remains until full recovery of the vegetation.

All these effects were present in all simulations whatever the land cover and model resolution and there are thus robust processes in both regional climate simulations and process studies or short-time forecast. However, the effect of the wildfires on the water cycle is much more sensitive to the model resolution when precipitation is concerned. Indeed, with the Kain-Fritsch convective parameterization, a negative feedback loop is simulated. This means that drier soil in the burnt area produces more rain due to enhanced atmosphere instability and enhanced convergence due to local larger surface heat fluxes. Because the air is too dry and hot, the simulations with explicitly resolved parameterization do not produce

precipitation. In case of moist air advection, large-scale explicit precipitation decreases in the presence of a burnt area. Indeed, the warmer air over the burnt area and the stronger updrafts increase dry air entrainment and liquid water evaporation. However, parameterized precipitation increase and dominate over the explicit parameterization. Therefore in case of moist air advection, the explicit simulations tend to weaken the water cycle over the burnt area whereas it is the opposite with the simulations with parameterized convection. So despite an atmospheric response to burnt area rather robust with respect to the model resolution, the precipitation signal remains very uncertain, especially because low precipitation are at stake. However, even low precipitation over burnt area can have serious consequences since burnt soil is more hydrophobic and floods and landslides can be facilitated.

Evaluating the accuracy of the simulated changes against observations would definitely give more weight to the conclusions but is absolutely not straightforward. Indeed, the most significant signal is located over the burnt area and its duration is limited by the westerly synoptic flow that damps the response of the atmosphere to the burnt surface only few days after the wildfire. Accurate in-situ measurements in the region where the atmospheric perturbation by the wildfire could be measured are not available during the wildfire and immediately after. Information on cloudiness and boundary layer height could be inferred from satellite, but with too large uncertainty since the large optical thickness of the smoke plume is detrimental to the accuracy of the satellite retrievals. Conducting such a verification with observations for one single case would require a dedicated methodological development which is much beyond the scope of this study and is left for future dedicated work.

This chapter partly answers the question raised as a third research objective of this thesis. We see that the important changes in surface heat fluxes balance can cause significant changes in the atmospheric flow for recent burnt scar, at least in simulations.

Chapter 5

Conclusions

This thesis highlighted the interweaving of forest fires and meteorology. I aimed at putting into light both the meteorological driving factors of large wildfire occurrence, how they could be used to improve fire danger assessment and their feedback on regional weather.

I found that heatwaves are important favorable conditions for large wildfires to occur, and could be an element of explanation for the synchronicity of large-scale wildfire events (megafires, San-Miguel-Ayanz et al. (2013)). Their dynamics are strongly linked to the duration of wildfire events and the strong fuel drying they incur causes very large burnt areas, as it was observed in the 2003 Portugal catastrophe. Furthermore, a second mode linked to high burnt area and high fire intensity was found. It resembles a synoptic blocking, however less pronounced and elongated into a curved ridge. These two modes of high burnt area were investigated using probabilistic cellular automata. This modeling framework helped us understand that fire propagation is strongly linked to the phenomenon of percolation, characterized by the possibility of an infinite propagation in the model. Percolation starts occurring abruptly above a certain threshold of fire propagation probability. This threshold varies with wind speed, explaining the two modes that we observed. An intuitive explanation accompanying this rather theoretical argument is that when wind speed is moderate, wildfire backpropagation is strongly impaired whereas forward propagation is weakly enhanced. This leads to smaller wildfires for moderate wind speeds. With these findings, answers to my first research objective were given.

Using this knowledge, I found that probabilities of especially large or intense wildfire occurrence could be reconstructed using few meteorological parameters, even though these probabilities were insufficient to build a proper fire risk assessment system. These findings tackle the issue raised as a second research objective. I find that the statistical law that best represents the logarithm of fire size and fire intensity is the Log-Normal. Using the strong hypothesis that the conditional distribution function of both fire variables with respect to meteorology is also Log-Normal, I designed a methodology to retrieve the probabilities of large or particularly intense wildfire occurrence. I used the 2-meter air temperature, the surface wind speed and the spring precipitation days anomaly as meteorological covariates, thereby considering the impact of weather at various time-scales. These probabilities give some contrast to fire

danger in summer, which is an improvement when compared to the usual approach using the Canadian Fire Weather Index as fire danger index. I also found that our two modes happened for different values of spring precipitation days anomaly. The low-wind-speed mode, related to heatwaves, is seen for wetter springs whereas the high-wind-speed mode can be observed for drier springs.

Finally, as fire significantly modifies the properties of the land surface, they impact local meteorology by triggering inland breezes and enhanced dry convection. This was verified using WRF simulations over Portugal for the 2003 month of August. We see the transport of surrounding humid air above the drier and darker burnt area, triggering enhanced cloudiness. The impact on precipitation occurrence is unclear, as the time period we chose to perform our simulations covers very few precipitation days. As it depends on inland breezes, this phenomenon especially impact weather during heatwaves, showing the important feedback between the two phenomena. The intensity of the weather modifications observed in our simulations varies with the age of the burnt scar. As soil temperature and moisture anomalies disappear, respectively because of heat propagation to atmosphere and precipitations, the inland breezes grow weaker. With vegetation recovery and the disappearance of the physical land surface properties modifications by fire, the impact on weather is completely negated. With this study insights have been given on the impacts of burnt scars on local weather, my third research objective.

Consolidation of this hereby exposed knowledge would help increase confidence in the results. For example a measurement campaign over recent burnt scars could help experimentally verify the findings of Chapter 4. These measurements could be focused on heatwave time periods, since in simulations the impact of burnt scars was most intense during low-wind, high-temperature conditions. On the other hand, a question that remains in suspense is the influence of burnt-scar-related land-cover changes on the water cycle. If the convergence of air masses over the burnt area causes more precipitations, this would add more proof to the negative precipitation-soil-moisture feedback first observed in simulations by Hohenegger et al. (2009). Taking into account these findings in weather simulations could add more accuracy to local rainfall forecasting.

Our studies mainly focused on short term links between weather and wildfires. Indications of linkage between spring drought and wildfires found in Chapter 3 could be further studied. Using a land-surface model incorporating fuel moisture and amount coupled with the vegetation life-cycle, we could trace the physical mechanisms leading to higher burnt area in years with drier springs. This would lead to longer term risk indications of fire danger, which could be helpful for firefighting resources management.

Finally we saw in Chapter 2 that cellular automata were useful for burnt scar modeling and theoretical investigations of fire data. Improving this tool would be useful, both for research and risk analysis using burn probability maps (Miller et al., 2008). Incorporating the influence of fuel amount and moisture in the local rule controlling the dynamics of the automata would be an interesting improvement. To complete this goal, mapping of these two quantities are required and measurement campaigns could be useful to calibrate the physical numerical models that could be used for their prediction. On the short term, this tool could be used to enhance the quality of air pollution alerts when wildfires occur. A system based on early satellite detection, wildfire total burnt area derivation using a cellular automata algorithm and the calculation of atmospheric pollutant transportation using the WRF/CHIMERE coupled model

could lead to accurate predictions of wildfire-related air pollution events.

Appendix A

Algorithmic implementation of the PCA

```
1  // MATLAB/C++ implementation of the probabilistic cellular
       automata fire propagation model (PCA)
2  // To compile:
3  // >> cd /path/to/CA_mex_wind.cpp
4  // >> mex CA_mex_wind.cpp
5  // To use in MATLAB
6  // [ca] = CA_mex_wind(p0,u,v);
7
8  // p0 is the constant part of the propagation probability
       (double)
9  // u is the zonal wind ((N+2,N+2) double array)
10 // v is the meridional wind ((N+2,N+2) double array)
11 // The random seed is not set here but could be implemented as a
       parameter of the CA_mex_wind function for reproductibility
12
13 #include "mex.h"
14 #include <iostream>
15 #include <cmath>
16 #include <vector>
17 #include <array>
18 #include <string>
19 #include <cstdlib>
20
21 using namespace std;
22
```

```
23 #define S_MAX 4 // Used to set an upper theshold on Cell states
      (only 1, 2, 3 and 4 are authorized)
24
25 #define c1 0.045
26 #define c2 0.131 // Constants for wind function (Alexandridis et
      al. (2008))
27
28 const double PI = 3.1416;
29 const int N = 101; // The PCA grid is a (N+2)x(N+2) square
      lattice
30
31 // Definition of the Cell class
32 // The PCA grid is a (N+2)x(N+2) Cell array
33
34 class Cell{
35   int state; // state of the Cell
36           // 1 is never burning
37           // 2 is unburnt
38           // 3 is burning
39           // 4 is burnt
40   public:
41     // Method to set the state
42     void sets(int s){
43       state = s;
44     }
45     // Method to get the state
46     int gets() const{
47       return state;
48     }
49     // Method to increment the state
50     void incs(){
51       state++;
52     }
53     // Default constructor (state <- unburnt)
54     Cell(){
55       state = 2;
56     }
57     // Constructor for a specified state
58     Cell(int s){
```

```
59        state = s;
60      }
61      // Overloading of = operator
62      // Creates a new Cell object with same state
63      Cell operator= (Cell C){
64        int s = C.gets();
65        return Cell(s);
66      }
67  };
68
69
70  // Definition of the Cells class
71  // Corresponds to a PCA grid
72  typedef array<array<Cell,N+2>,N+2> Cells;
73  // Table is a class used for saving doubles corresponding to
      each Cell of the PCA
74  typedef array<array<double,N+2>,N+2> Table;
75  // TableN is used for saving neighbors of each interior Cell of
      the PCA grid
76  typedef array<array<array<array<int,2>,8>,N>,N> TableN;
77  // TableA is used for saving the Angle table corresponding to
      the angles between the  vertical axis (oriented up) and the
      direction of propagation
78  typedef array<array<double,3>,3> TableA;
79
80  // Function that prints the PCA in the command line (used for
      debugging only, without the MATLAB link)
81
82  void showCA(Cells const& CA){
83    for (int i = 0; i < N+2; i++){
84      for (int j = 0; j < N+2; j++){
85        if (j < N+1){
86          int n;
87          if (CA[i][j].gets() == 2){
88            n = 0;
89          }
90          else {
91            n = CA[i][j].gets();
92          }
```

```
93          cout << n << " ";
94        }
95        else{
96          cout << CA[i][j].gets() << endl;
97        }
98      }
99    }
100 }
101
102 // Function used to print a line between each calls of showCA()
      in debugging
103
104 void blankline(){
105   string s = "\n";
106   s += "/";
107   for (int i = 0; i < N; i++){
108     s += " *";
109   }
110   s += " /";
111   s += "\n";
112   cout << s << endl;
113 }
114
115 // Function used to save the coordinates of the neighbors of a
      Cell located at (i,j)
116
117 array<array<int,2>,8> getNeighbors(int i, int j){
118
119   array<array<int,2>,8> M;
120
121   M[0][0] = i-1;
122   M[0][1] = j-1;
123
124   M[1][0] = i-1;
125   M[1][1] = j;
126
127   M[2][0] = i-1;
128   M[2][1] = j+1;
129
```

```
130   M[3][0] = i+1;
131   M[3][1] = j-1;
132
133   M[4][0] = i+1;
134   M[4][1] = j;
135
136   M[5][0] = i+1;
137   M[5][1] = j+1;
138
139   M[6][0] = i;
140   M[6][1] = j-1;
141
142   M[7][0] = i;
143   M[7][1] = j+1;
144
145   return M;
146 }
147
148 // Function to define the neighbors of all Cell-s in the PCA
149
150 TableN initTableNeighbors(){
151   TableN TableNeighbors;
152   for (int i = 1; i < N+1; i++){
153     for (int j = 1; j < N+1; j++){
154       array<array<int,2>,8> NN = getNeighbors(i,j);
155       for (int n1 = 0; n1 < 8; n1++){
156         for (int n2 = 0; n2 < 2; n2++){
157           TableNeighbors[i-1][j-1][n1][n2] = NN[n1][n2];
158         }
159       }
160     }
161   }
162   return TableNeighbors;
163 }
164
165 // Function to define the angles between a PCA Cell and its
166 // neighbors
167
168 array<array<double,3>,3> initAngle(){
```

```
169   array<array<double,3>,3> Angle;
170
171   Angle[0][0] = -3*PI/4;
172   Angle[0][1] = PI;
173   Angle[0][2] = 3*PI/4;
174   Angle[1][0] = -PI/2;
175   Angle[1][1] = 0;
176   Angle[1][2] = PI/2;
177   Angle[2][0] = -PI/4;
178   Angle[2][1] = 0;
179   Angle[2][2] = PI/4;
180
181   return Angle;
182 }
183
184 // Function that explores the neighborhood of Cell (i,j) of the
      PCA and returns the burning ones
185 // Used for the the computation of the fire propagation
186
187 vector<array<int,2>> BurningNeighbors(Cells const& CA, int i,
      int j, TableN const& TableNeighbors){
188   vector<array<int,2>> Burn;
189   for (int n = 0; n < 8; n++){
190     int state_n = CA[TableNeighbors[i-1][j-1][n][0]]\
191       [TableNeighbors[i-1][j-1][n][1]].gets();
192     if (state_n > 2 && state_n < S_MAX){
193       array<int,2> k;
194       k[0] = TableNeighbors[i-1][j-1][n][0];
195       k[1] = TableNeighbors[i-1][j-1][n][1];
196       Burn.push_back(k);
197     }
198   }
199   return Burn;
200 }
201
202 // Function to compute the wind function in the probability of
      propagation given the wind (U,V)
203 // U is the zonal wind
204 // V is the meridional wind
```

```
205 // (i1,j1) is the burning Cell
206 // (i2,j2) is the Cell that will burn if the fire propagates
207
208 double proba_wind(int i1, int j1, int i2, int j2, Table const&
       U, Table const& V, TableA const& Angle){
209   double angleW; // Angle between the wind direction and the
        horizontal axis (right oriented)
210   if (U[i2-1][j2-1] == 0){
211     if (V[i2-1][j2-1] == 0){
212       angleW = 0;
213     }
214     else if (V[i2-1][j2-1] > 0){
215       angleW = PI/2;
216     }
217     else {
218       angleW = -PI/2;
219     }
220   }
221   else if (U[i2-1][j2-1] < 0){
222     if (V[i2-1][j2-1] == 0){
223       angleW = PI;
224     }
225     else {
226       angleW = atan(V[i2-1][j2-1]/U[i2-1][j2-1]) + PI;
227     }
228   }
229   else if (U[i2-1][j2-1] > 0){
230     if (V[i2-1][j2-1] == 0){
231       angleW = 0;
232     }
233     else {
234       angleW = atan (V[i2-1][j2-1]/U[i2-1][j2-1]);
235     }
236   }
237   double theta = -Angle[i2-i1+1][j2-j1+1] - PI/2 - angleW; //
        Angle between the wind and the propagation direction
238   double W = sqrt(pow(U[i2-1][j2-1],2) + pow(V[i2-1][j2-1],2));
        // Wind speed
```

```
239   double p = exp(W * (c1 + c2 * (cos(theta)-1))); // Wind
        function in the probability (Alexandridis et al. (2008))
240   return p;
241 }
242
243 // Function to compute the propagation probability between a
    (i1,j1) burning Cell and a (i2,j2) unburned Cell
244
245 double compute_proba(Cells const& CA, int i1, int j1, int i2,
    int j2, double const& p0,
246  Table const& U, Table const& V, TableA const& Angle){
247
248   double p; // Propagation probability
249   double pw = proba_wind(i1, j1, i2, j2, U, V, Angle); // Wind
        function in the propagation probability
250   double pcorr = i1 != i2 && j1 != j2 ? 1/sqrt(2) : 1; //
        Corrective factor for diagonal propagation
251
252   p = p0 * pw * pcorr;
253
254   if (p > 1) {
255     p = 1;
256   }
257   return p;
258 }
259
260 // Function that takes the PCA grid at time t and returns
    another PCA grid at time t+1
261
262 Cells evol(Cells const& CA, double const& p0, Table const& U,
    Table const& V, TableN const& TableNeighbors, TableA const&
    Angle){
263   Cells CA2 = CA;
264   #pragma omp parallel for
265   for (int i = 1; i < N+1; i++){
266     for (int j = 1; j < N+1; j++){
267       if (CA[i][j].gets() >2 && CA[i][j].gets() < S_MAX){
268         CA2[i][j].incs();
269       }
```

```
270       else if (CA2[i][j].gets() == 2){
271         vector<array<int,2>> Neighbors =
              BurningNeighbors(CA,i,j,TableNeighbors);
272         if (Neighbors.size() > 0){
273           double NP = 1;
274           for (int n = 0; n < Neighbors.size(); n++){
275             NP *= 1 - compute_proba(CA,i,j,Neighbors[n][0]\
276               ,Neighbors[n][1],p0,U,V,Angle);
277           }
278           double Guess = (double) rand() / (double) RAND_MAX;
279           if (Guess < 1 - NP){
280             CA2[i][j].incs();
281           }
282         }
283       }
284     }
285   }
286   return CA2;
287 }
288
289 // Function to determine if a PCA grid contains at least one
      burning Cell
290 // Returns 0 if not
291 // Returns 1 otherwise
292
293 int isBurning(Cells const& CA){
294   for (int i = 1; i < N+1; i++){
295     for (int j = 1; j < N+1; j++){
296       if (CA[i][j].gets() > 2 && CA[i][j].gets() < S_MAX){
297         return 1;
298       }
299     }
300   }
301   return 0;
302 }
303
304 // Main function
305
```

```
306 void mexFunction(int nlhs, mxArray *plhs[], int nrhs, const
       mxArray *prhs[])
307 {
308   // Creation of Cells vector
309
310   int entier = 0;
311   mexPrintf("Pointer declaration\n");
312
313   #define P0_IN prhs[0]
314   #define U_IN prhs[1]
315   #define V_IN prhs[2]
316   #define A_OUT plhs[0]
317
318   double p0, *U, *V;
319   double *A;
320
321   p0 = mxGetScalar(P0_IN);
322   U = (double *) mxGetPr(U_IN);
323   V = (double *) mxGetPr(V_IN);
324
325   // Allocation of the Cells vector CAs containing the PCA grids
       for all time steps
326
327   vector<Cells> CAs;
328
329   // Initialisation of the PCA at t = 0 and the u and v wind
       arrays
330
331   mexPrintf("Assignation of the different input variables\n");
332
333   static Cells CA;
334   static Table u, v;
335
336
337   #pragma omp parallel for
338   for (int i = 0; i < N+2; i++){
339     for (int j = 0; j < N+2; j++){
340       CA[i][j] = Cell();
341       CA[i][j].sets(2);
```

```
342       if(i != 0 && i != N+1 && j != 0 && j != N+1){
343         u[i][j] = U[N*(i-1) + j-1];
344         v[i][j] = V[N*(i-1) + j-1];
345       }
346     }
347   }
348
349   // Definition of the borders and initialisation of the
        wildfire, in the middle of the grid
350
351   for (int j = 0; j < N+2; j++){
352     CA[0][j].sets(1);
353     CA[N+1][j].sets(1);
354   }
355
356   for (int i = 0; i < N+2; i++){
357     CA[i][0].sets(1);
358     CA[i][N+1].sets(1);
359   }
360
361   CA[floor(N/2)+1][floor(N/2)+1].sets(3);
362   CAs.push_back(CA);
363
364   // Initialisation of the neighbors and angle arrays
365
366   mexPrintf("Calculation of the Neighbors and Angle Tables\n");
367   static TableN TableNeighbors = initTableNeighbors();
368   static TableA Angle = initAngle();
369
370   // Computation of the evolution of the cellular automata
371
372   mexPrintf("Beginning of the main loop \n");
373
374   int T = 0;
375
376   while (isBurning(CAs.back())){
377     T++;
378     CAs.push_back(evol(CAs.back(),p0,u,v,TableNeighbors,Angle));
379   }
```

```
380
381   mexPrintf("End of the main loop\n");
382
383   const int K = 3;
384   int dims[K];
385   dims[0] = N;
386   dims[1] = N;
387   dims[2] = T+1;
388
389   mexPrintf("Creation of the output pointers\n");
390
391   A_OUT = mxCreateNumericArray(K,dims,mxDOUBLE_CLASS,mxREAL);
392   A = mxGetPr(A_OUT);
393
394   mexPrintf("Assignment of the output\n");
395
396   for (int i = 1; i < N+1; i++){
397     for (int j = 1; j < N+1; j++){
398       for (int t = 0; t < T+1; t++){
399         A[i-1 + N*(j-1) + N*N*t] = CAs[t][i][j].gets();
400       }
401     }
402   }
403
404   mexPrintf("End of the program\n");
405
406   return;
407 }
```

CA_mex_wind.cpp

Appendix B

Derivation of the $C(V)$ constant

In this Appendix, the calculation of $C(V)$ is detailed. The quantity $C(V)$ corresponds to the sum of the probabilities that the fire propagates from a neighboring cell to the center cell (Figure B.1).

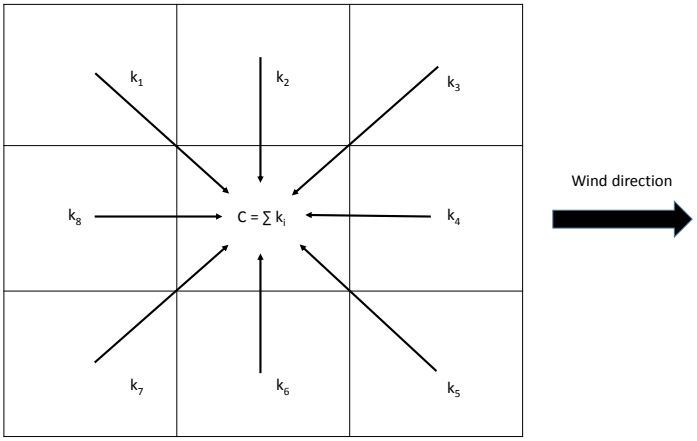

FIGURE B.1: Schematic of the calculation of $C(V)$.

For all 8 neighbors we can write:

$$p_i = k_i p_0 \tag{B.1}$$

with k_i being a coefficient depending on the direction of propagation. One can write

$$k_i = \gamma_i \exp\{V\,[c_1 + c_2\,(cos\theta_i - 1)]\} \tag{B.2}$$

with θ_i being the angle between the direction of propagation and the direction of the wind for the i component and γ_i being equal to γ or 1 depending on whether the propagation direction is diagonal or

not in the PCA grid. One can write:

$$k_1 = k_7 = \gamma \exp\left\{V\left[c_1 - c_2\left(1 - \sqrt{2}/2\right)\right]\right\} \tag{B.3}$$

$$k_2 = k_6 = \exp\left[V\left(c_1 - c_2\right)\right] \tag{B.4}$$

$$k_3 = k_5 = \gamma \exp\left\{V\left[c_1 - c_2\left(1 + \sqrt{2}/2\right)\right]\right\} \tag{B.5}$$

$$k_4 = \exp\left[V\left(c_1 - 2c_2\right)\right] \tag{B.6}$$

$$k_8 = \exp\left(Vc_1\right) \tag{B.7}$$

The quantity $C(V)$ is the sum of the k_i coefficients and thus writes:

$$\begin{aligned} C(V) \quad = \quad & \exp\left(Vc_1\right) + 2\exp\left[V\left(c_1 - c_2\right)\right] + \exp\left[V\left(c_1 - 2c_2\right)\right] \\ & + 2\gamma \exp\left\{V\left[c_1 + c_2\left(\tfrac{\sqrt{2}}{2} - 1\right)\right]\right\} \\ & + 2\gamma \exp\left\{V\left[c_1 - c_2\left(\tfrac{\sqrt{2}}{2} + 1\right)\right]\right\} \end{aligned} \tag{B.8}$$

which can be simplified into:

$$\begin{aligned} C(V) \quad = \quad & \exp\left(Vc_1\right) \times \left\{\left[1 + \exp\left(-Vc_2\right)\right]^2 + \right. \\ & \left. \sqrt{2}\left(\exp\left[Vc_2\left(\tfrac{\sqrt{2}}{2} - 1\right)\right] + \exp\left[-Vc_2\left(\tfrac{\sqrt{2}}{2} + 1\right)\right]\right)\right\} \end{aligned} \tag{B.9}$$

using $\gamma = 1/\sqrt{2}$.

Bibliography

Aguado, I., Chuvieco, E., Borén, R., Nieto, H., 2007. Estimation of dead fuel moisture content from meteorological data in mediterranean areas. applications in fire danger assessment. International Journal of Wildland Fire 16 (4), 390–397.

Alexandridis, A., Vakalis, D., Siettos, C. I., Bafas, G. V., 2008. A cellular automata model for forest fire spread prediction: The case of the wildfire that swept through spetses island in 1990. Applied Mathematics and Computation 204 (1), 191–201.

Alonso-Betanzos, A., Fontenla-Romero, O., Guijarro-Berdiñas, B., Hernández-Pereira, E., Inmaculada Paz Andrade, M., Jiménez, E., Luis Legido Soto, J., Carballas, T., 2003. An intelligent system for forest fire risk prediction and fire fighting management in galicia. Expert Systems with Applications 25 (4), 545–554.

Amatulli, G., Camia, A., San-Miguel-Ayanz, J., 2013. Estimating future burned areas under changing climate in the eu-mediterranean countries. Science of the Total Environment 450, 209–222.

Amiro, B., MacPherson, J., Desjardins, R., 1999. BOREAS flight measurements of forest-fire effects on carbon dioxide and energy fluxes. Agricultural and Forest Meteorology 96 (4), 199–208.

Anderson, T. W., Darling, D. A., 1954. A test of goodness of fit. Journal of the American Statistical Association 49 (268), 765–769.

Avissar, R., Schmidt, T., 1998. An evaluation of the scale at which ground-surface heat flux patchiness affects the convective boundary layer using large-eddy simulations. Journal of the Atmospheric Sciences 55 (16), 2666–2689.

Barriopedro, D., Fischer, E. M., Luterbacher, J., Trigo, R. M., García-Herrera, R., 2011. The hot summer of 2010: redrawing the temperature record map of europe. Science 332 (6026), 220–224.

Bastin, S., Drobinski, P., Dabas, A., Delville, P., Reitebuch, O., Werner, C., 2005. Impact of the rhône and durance valleys on sea-breeze circulation in the marseille area. Atmos. Res. 74, 303–328.

Batllori, E., Parisien, M.-A., Krawchuk, M. A., Moritz, M. A., 2013. Climate change-induced shifts in fire for mediterranean ecosystems. Global Ecology and Biogeography 22 (10), 1118–1129.

Bedia, J., Herrera, S., Gutiérrez, J. M., et al., 2014. Assessing the predictability of fire occurrence and area burned across phytoclimatic regions in spain. Natural Hazards and Earth System Sciences 14 (1), 53–66.

Beringer, J., Hutley, L. B., Tapper, N. J., Coutts, A., Kerley, A., O'Grady, A. P., 2003. Fire impacts on surface heat, moisture and carbon fluxes from a tropical savanna in northern australia. International Journal of Wildland Fire 12 (4), 333–340.

Berjak, S. G., Hearne, J. W., 2002. An improved cellular automaton model for simulating fire in a spatially heterogeneous savanna system. Ecological Modelling 148 (2), 133–151.

Beygelzimer, A., Kakadet, S., Langford, J., Arya, S., Mount, D., Li, S., 2013. FNN: Fast Nearest Neighbor Search Algorithms and Applications. R package version 1.1.
URL `http://CRAN.R-project.org/package=FNN`

Black, E., Blackburn, M., Harrison, G., Hoskins, B., Methven, J., 2004. Factors contributing to the summer 2003 european heatwave. Weather 59 (8), 217–223.

Brunel, E., Comte, F., Lacour, C., 2010. Minimax estimation of the conditional cumulative distribution function. Sankhya A 72 (2), 293–330.

Cardil, A., Salis, M., Spano, D., Delogu, G., Molina Terrén, D., 2014. Large wildland fires and extreme temperatures in sardinia (italy). iForest-Biogeosciences and Forestry 7 (3), 162.

Carmo, M., Moreira, F., Casimiro, P., Vaz, P., 2011. Land use and topography influences on wildfire occurrence in northern portugal. Landscape and Urban Planning 100 (1), 169–176.

Cassou, C., Terray, L., Phillips, A. S., 2005. Tropical atlantic influence on european heat waves. Journal of climate 18 (15), 2805–2811.

Castro, F., Tudela, A., Sebastià, M., 2003. Modeling moisture content in shrubs to predict fire risk in catalonia (spain). Agricultural and Forest Meteorology 116 (1), 49–59.

Chambers, S., Beringer, J., Randerson, J., Chapin III, F., 2005. Fire effects on net radiation and energy partitioning: Contrasting responses of tundra and boreal forest ecosystems. J. Geophys. Res. 110 (D09106).

Clark, T., Jenkins, M., Coen, J., Packham, D., 1996. A coupled atmosphere-fire model: Role of the convective froude number and dynamic fingering at the fireline. International Journal of Wildland Fire 6 (4), 177–190.

Cortez, P., Morais, A. d. J. R., 2007. A data mining approach to predict forest fires using meteorological data.

Courault, D., Drobinski, P., Brunet, Y., Lacarrere, P., Talbot, C., 2007. Impact of surface heterogeneity on a buoyancy-driven convective boundary layer in light winds. Boundary-Layer Meteorology 124 (3), 383–403.

Davies, S. J., Unam, L., 1999. Smoke-haze from the 1997 indonesian forest fires: effects on pollution levels, local climate, atmospheric co2 concentrations, and tree photosynthesis. Forest Ecology and Management 124, 137 – 144.

Davies, T., Cullen, M., Malcolm, A., Mawson, M., Staniforth, A., White, A., Wood, N., 2005. A new dynamical core for the met office's global and regional modelling of the atmosphere. Q. J. R. Meteorol. Soc. 131, 1759–1782.

DeBano, L., 2000. The role of fire and soil heating on water repellency in wildland environments: a review. Journal of Hydrology 231232, 195–206.

Dee, D., Uppala, S., Simmons, A., Berrisford, P., Poli, P., Kobayashi, S., Andrae, U., Balmaseda, M., Balsamo, G., Bauer, P., et al., 2011. The era-interim reanalysis: Configuration and performance of the data assimilation system. Quarterly Journal of the Royal Meteorological Society 137 (656), 553–597.

Delignette-Muller, M. L., Dutang, C., 2015. fitdistrplus: An R package for fitting distributions. Journal of Statistical Software 64 (4), 1–34.
URL `http://www.jstatsoft.org/v64/i04/`

Dimitrakopoulos, A. P., Vlahou, M., Anagnostopoulou, C. G., Mitsopoulos, I., 2011. Impact of drought on wildland fires in greece: implications of climatic change? Climatic Change 109 (3-4), 331–347.

Drobinski, P., Bastin, S., Dabas, A., Delville, P., Reitebuch, O., 2006. Variability of three-dimensional sea breeze structure in southern france: observations and evaluation of empirical scaling laws. Ann. Geophys. 24, 1783–1799.

Drobinski, P., Dubos, T., 2009. Linear breeze scaling: from large-scale land/sea breezes to mesoscale inland breezes. Quarterly Journal of the Royal Meteorological Society 135 (644), 17661775.

Dudhia, J., 1989. Numerical study of convection observed during the winter monsoon experiment using a mesoscale two-dimensional model. J. Atmos. Sci. 46, 3077–3107.

EFFIS, 2003. Forest fires in europe - 2003 fire campaign. Joint Research Center, European Commission.
URL `http://forest.jrc.ec.europa.eu/effis/reports/annual-fire-reports/`

Ek, M., Mitchell, K., Lin, Y., Rogers, E., Grunmann, P., Koren, V., Gayno, G., Tarpley, D., 2003. Implementation of Noah land-surface model advances in the NCEP operational mesoscale Eta model, 12845.

Ek, M. B., Holtslag, A. A. M., 2004. Influence of soil moisture on boundary layer cloud development. J. Hydrometeorol. 5, 86–89.

Encinas, A. H., Encinas, L. H., White, S. H., del Rey, A. M., Sánchez, G. R., 2007a. Simulation of forest fire fronts using cellular automata. Advances in Engineering Software 38 (6), 372–378.

Encinas, L. H., White, S. H., del Rey, A. M., Sanchez, G. R., 2007b. Modelling forest fire spread using hexagonal cellular automata. Applied mathematical modelling 31 (6), 1213–1227.

Estoque, M., 1962. Variability of three-dimensional sea breeze structure in southern france: observations and evaluation of empirical scaling laws. J. Atmos. Sci. 19, 244–250.

European Commission, 2010. Forest fires in europe 2009. Office for Official Publication of the European Communities, Luxembourg EUR 24502 EN, 81.

Flannigan, M., Harrington, J., 1988. A study of the relation of meteorological variables to monthly provincial area burned by wildfire in canada (1953-80). Journal of Applied Meteorology 27 (4), 441–452.

Flannigan, M., Wotton, B., et al., 2001. Climate, weather, and area burned. Forest fires. New York: Academic Press. p 351, 73.

Flannigan, M. D., Krawchuk, M. A., de Groot, W. J., Wotton, B. M., Gowman, L. M., 2009. Hymex, a 10-year multidisciplinary program on the mediterranean water cycle. International Journal of Wildland Fire 18, 483–507.

Flaounas, E., Drobinski, P., Vrac, M., Bastin, S., Lebeaupin-Brossier, C., Stéfanon, M., Borga, M., Calvet, J., 2013. Precipitation and temperature space-time variability and extremes in the mediterranean region: evaluation of dynamical and statistical downscaling methods. Clim. Dyn. 40, 2687–2705.

Fox, J., Weisberg, S., 2011. An R Companion to Applied Regression, 2nd Edition. Sage, Thousand Oaks CA.
URL `http://socserv.socsci.mcmaster.ca/jfox/Books/Companion`

Ganteaume, A., Camia, A., Jappiot, M., San-Miguel-Ayanz, J., Long-Fournel, M., Lampin, C., 2013. A review of the main driving factors of forest fire ignition over europe. Environmental management 51 (3), 651–662.

Gentine, P., Holtslag, A., D'Andrea, F., Ek, M., 2013. Surface and atmospheric controls on moist convection onset over land. J. Hydrometeorol. 14, 14431462.

Giglio, L., Randerson, J., Van der Werf, G., Kasibhatla, P., Collatz, G., Morton, D., DeFries, R., 2010. Assessing variability and long-term trends in burned area by merging multiple satellite fire products. Biogeosciences 7 (3).

Görgen, K., Lynch, A. H., Marshall, A. G., Beringer, J., 2006. Impact of abrupt land cover changes by savanna fire on northern australian climate. Journal of Geophysical Research: Atmospheres 111 (D19).

Haines, D. A., Main, W. A., Frost, J. S., Simard, A. J., 1983. Fire-danger rating and wildfire occurrence in the northeastern united states. Forest Science 29 (4), 679–696.

Hastie, T., Tibshirani, R., Friedman, J., Hastie, T., Friedman, J., Tibshirani, R., 2009. The elements of statistical learning. Vol. 2. Springer.

Hernandez, C., Drobinski, P., Turquety, S., 2015a. How much does weather control fire size and intensity in the mediterranean region ? Annales Geophisicae.

Hernandez, C., Drobinski, P., Turquety, S., 2015b. Impact of wildfire-induced land cover modification on local meteorology: A sensitivity study of the 2003 wildfires in portugal. Atmospheric Research 164, 49–64.

Hernandez, C., Drobinski, P., Turquety, S., Dupuy, J.-L., 2015c. Size of wildfires in the euro-mediterranean region: observations and theoretical analysis. Natural Hazards and Earth System Sciences Discussions 3 (2), 1203–1230.

Hernandez, C., Keribin, C., Drobinski, P., Turquety, S., 2015d. Statistical modelling of wildfire size and intensity: a step toward meteorological forecasting of summer extreme fire risk. Annales Geophysicae 33 (12), 1495–1506.
URL `http://www.ann-geophys.net/33/1495/2015/`

Hohenegger, C., Brockhaus, P., Bretherton, C. S., Schr, C., 2009. The soil moistureprecipitation feedback in simulations with explicit and parameterized convection. Journal of Climate 22 (19), 5003–5020.

Hoinka, K. P., Carvalho, A., Miranda, A. I., 2009. Regional-scale weather patterns and wildland fires in central portugal. International Journal of Wildland Fire 18 (1), 36–49.

Hong, S.-Y., Dudhia, J., Chen, S.-H., 2004. A revised approach to ice microphysical processes for the bulk parameterization of clouds and precipitation. Monthly Weather Review 132 (1), 103–120.

Ichoku, C., Giglio, L., Wooster, M. J., Remer, L. A., 2008. Global characterization of biomass-burning patterns using satellite measurements of fire radiative energy. Remote Sensing of Environment 112 (6), 2950–2962.

Jacob, D., Petersen, J., Eggert, B., Alias, A., Christensen, O. B., Bouwer, L., Braun, A., Colette, A., Déqué, M., Georgievski, G., Georgopoulou, E., Gobiet, A., Menut, L., Nikulin, G., Haensler, A., Hempelmann, N., Jones, C., Keuler, K., Kovats, S., Krner, N., Kotlarski, S., Kriegsmann, A., Martin, E., Meijgaard, E., Moseley, C., Pfeifer, S., Preuschmann, S., Radermacher, C., Radtke, K., Rechid, D., Rounsevell, M., Samuelsson, P., Somot, S., Soussana, J.-F., Teichmann, C., Valentini, R., Vautard, R., Weber, B., Yiou, P., 2014. Euro-cordex: new high-resolution climate change projections for european impact research. Regional Environmental Change 14, 563–578.

Kain, J., 2004. The kain-fritsch convective parameterization: An update. J. Appl. Meteorol. 43, 170–181.

Kilinc, Musa, J. B., 2007. The spatial and temporal distribution of lightning strikes and their relationship with vegetation type, elevation, and fire scars in the northern territory. J. Climate 20, 11611173.

Knowles, J. B., 1993. The influence of forest fire induced albedo differences on the generation of mesoscale circulations. Tech. rep.

Kochanski, A. K., Jenkins, M. A., Mandel, J., Beezley, J., Krueger, S., 2013. Real time simulation of 2007 santa ana fires. Forest Ecology and Management 294, 136–149.

Koutsias, N., Xanthopoulos, G., Founda, D., Xystrakis, F., Nioti, F., Pleniou, M., Mallinis, G., Arianoutsou, M., 2013. On the relationships between forest fires and weather conditions in greece from long-term national observations (1894–2010). International Journal of Wildland Fire 22 (4), 493–507.

Kremens, R., Faulring, J., Hardy, C., 2003. Measurement of the time-temperature and emissivity history of the burn scar for remote sensing applications. In: 5th Symposium on Fire and Forest Meteorology and the 2nd International Wildland Fire Ecology and Fire Management Congress. American Meteorological Society, Orlando, FL, USA.

Le Houérou, H. N., 1987. Vegetation wildfires in the mediterranean basin: evolution and trends. Ecologia Mediterranea. XIII 13, 13–24.

Leisch, F., Tibshirani, R., 2014. bootstrap: Functions for the Book "An Introduction to the Bootstrap". R package version 2014.4.
URL `http://CRAN.R-project.org/package=bootstrap`

Levin, N., Saaroni, H., 1999. Fire weather in israelsynoptic climatological analysis. GeoJournal 47 (4), 523–538.

Linn, R., Reisner, J., Colman, J. J., Winterkamp, J., 2002. Studying wildfire behavior using firetec. International journal of wildland fire 11 (4), 233–246.

Loepfe, L., Rodrigo, A., Lloret, F., 2014. Two thresholds determine climatic control of forest fire size in europe and northern africa. Regional Environmental Change 14 (4), 1395–1404.

Matthews, S., 2006. A process-based model of fine fuel moisture. International Journal of Wildland Fire 15 (2), 155–168.

McMichael, C. E., 2004. Modeling the effects of fire on streamflow in a chaparral watershed.

Mendes-Lopes, J. M., Ventura, J. M., Amaral, J. M., 2003. Flame characteristics, temperature–time curves, and rate of spread in fires propagating in a bed of pinus pinaster needles. International Journal of Wildland Fire 12 (1), 67–84.

Miller, C., Parisien, M., Ager, A., Finney, M., et al., 2008. Evaluating spatially-explicit burn probabilities for strategic fire management planning. Transactions on Ecology and the Environment 119, 245–252.

Mlawer, E., Taubman, S., Brown, P., Iacono, M., Clough, S., 1997. Radiative transfer for inhomogeneous atmospheres: Rrtm, a validated correlated-k model for the longwave. Journal of Geophysical Research 102.

Mölders, N., Kramm, G., 2007. Influence of wildfire induced land-cover changes on clouds and precipitation in interior alaska a case study. Atmospheric Research 84 (2), 142–168.

Monin, A., Obukhov, A., 1954. Basic laws of turbulence mixing in the ground layer of the atmosphere.

Moreira, F., Viedma, O., Arianoutsou, M., Curt, T., Koutsias, N., Rigolot, E., Barbati, A., Corona, P., Vaz, P., Xanthopoulos, G., et al., 2011. Landscape–wildfire interactions in southern europe: implications for landscape management. Journal of environmental management 92 (10), 2389–2402.

Morvan, D., Dupuy, J., 2004. Modeling the propagation of a wildfire through a mediterranean shrub using a multiphase formulation. Combustion and Flame 138 (3), 199–210.

Mouillot, F., Rambal, S., Joffre, R., 2002. Simulating climate change impacts on fire frequency and vegetation dynamics in a mediterranean-type ecosystem. Global Change Biology 8 (5), 423–437.

Noh, Y., Cheon, W., Hong, S., Raasch, S., 2003. Improvement of the k-profile model for the planetary boundary layer base on large eddy simulation data.

Omrani, H., Drobinski, P., Dubos, T., 2012. Investigation of indiscriminate nudging and predictability in a nested quasi-geostrophic model. Q. J. R. Meteorol. Soc. 138, 401–427.

Omrani, H., Drobinski, P., Dubos, T., 2013. Optimal nudging strategies in regional climate modelling: investigation in a big-brother experiment over the european and mediterranean regions. J. Clim.

Pak, S. I., Hayakawa, T., 2011. Forest fire modeling using cellular automata and percolation threshold analysis. In: American Control Conference (ACC), 2011. IEEE, pp. 293–298.

Pausas, J. G., Paula, S., 2012. Fuel shapes the fire–climate relationship: evidence from mediterranean ecosystems. Global Ecology and Biogeography 21 (11), 1074–1082.

Pereira, M. G., Trigo, R. M., da Camara, C. C., Pereira, J., Leite, S. M., 2005. Synoptic patterns associated with large summer forest fires in portugal. Agricultural and Forest Meteorology 129 (1), 11–25.

Petters, M. D., Carrico, C. M., Kreidenweis, S. M., Prenni, A. J., DeMott, P. J., Collett, J. L., Moosmller, H., 2009. Cloud condensation nucleation activity of biomass burning aerosol. Journal of Geophysical Research: Atmospheres 114 (D22).

Pielke, R. A., Adegoke, J., Beltran-Przekurat, A., Hiemstra, C. A., Lin, J., Nair, U. S., Niyogi, D., Nobis, T. E., 2007. An overview of regional land-use and land-cover impacts on rainfall. Tellus B 59 (3), 587–601.

Pielke, R. A., Dalu, G. A., Snook, J. S., Lee, T. J., Kittel, T. G. F., 1991. Nonlinear influence of mesoscale land use on weather and climate. Journal of Climate 4 (11), 10531069.

Preisler, H. K., Brillinger, D. R., Burgan, R. E., Benoit, J., 2004. Probability based models for estimation of wildfire risk. International Journal of wildland fire 13 (2), 133–142.

R Core Team, 2013. R: A Language and Environment for Statistical Computing. R Foundation for Statistical Computing, Vienna, Austria.
URL `http://www.R-project.org/`

Rothermel, R. C., 1972. A mathematical model for predicting fire spread in wildland fuels.

Running, S. W., 2006. Is global warming causing more, larger wildfires? SCIENCE-NEW YORK THEN WASHINGTON- 313 (5789), 927.

Russo, L., Russo, P., Vakalisc, D., Siettos, C., 2014. Detecting weak points of wildland fire spread: A cellular automata model risk assessment simulation approach. Chemical Engineering 36.

Sakr, G. E., Elhajj, I. H., Mitri, G., 2011. Efficient forest fire occurrence prediction for developing countries using two weather parameters. Engineering Applications of Artificial Intelligence 24 (5), 888–894.

Salameh, T., Drobinski, P., Dubos, T., 2010. The effect of indiscriminate nudging time on large and small scales in regional climate modelling: application to the mediterranean basin. Q. J. R. Meteorol. Soc. 136, 170–182.

San-Miguel-Ayanz, J., Moreno, J. M., Camia, A., 2013. Analysis of large fires in european mediterranean landscapes: lessons learned and perspectives. Forest Ecology and Management 294, 11–22.

Schimel, D., Baker, D., 2002. Carbon cycle: The wildfire factor. Nature 420, 29–30.

Schoenberg, F. P., Peng, R., Woods, J., 2003. On the distribution of wildfire sizes. Environmetrics 14 (6), 583–592.

Scholes, R. J., Walker, B. H., 1993. An african savanna: synthesis of the nylsvley study., xii + 306 pp.

Sedano, F., Kempeneers, P., San Miguel, J., Strobl, P., Vogt, P., 2013. Towards a pan-european burnt scar mapping methodology vased on single date medium resolution optical remote sensing data. International Journal of Applied Earth Observation and Geoinformation 20, 52–59.

Segal, M., Avissar, R., McCumber, M. C., Pielke, R. A., 1988. Evaluation of vegetation effects on the generation and modification of mesoscale circulations. Journal of The Atmospheric Sciences 45 (16), 22682293.

Seiler, W., Crutzen, P., 1980. Estimates of gross and net fluxes of carbon between the biosphere and the atmosphere from biomass burning. Climatic Change 2 (3), 207–247.

Seity, Y., Brousseau, P., Malardel, S., Hello, G., Bénard, P., Bouttier, F., Lac, C., Masson, V., 2011. The arome-france convective-scale operational model. Mon. Wea. Rev. 139, 976–991.

Sharples, J., McRae, R., Weber, R., Gill, A., 2009. A simple index for assessing fuel moisture content. Environmental Modelling & Software 24 (5), 637–646.

Sharples, J. J., 2008. Review of formal methodologies for wind–slope correction of wildfire rate of spread. International Journal of Wildland Fire 17 (2), 179–193.

Silva, J. S., Rego, F., Fernandes, P., Rigolot, E., 2010a. Towards integrated fire management: outcomes of the European project Fire Paradox. European Forest Institute.

Silva, J. S., Rego, F., Fernandes, P., Rigolot, E., 2010b. Towards integrated fire management: outcomes of the European project Fire Paradox. European Forest Institute.

Simmons, A., Uppala, S., Dee, D., Kobayashi, S., 2006. Era-interim: New ecmwf reanalysis products from 1989 onwards. ECMWF Newsletter.

Skamarock, W., Klemp, J., 2007. A time-split nonhydrostatic atmospheric model for research and nwp applications. J. Comput. Phys. 227, 3465–3485.

Sousa, P. M., Trigo, R. M., Pereira, M. G., Bedia, J., Gutiérrez, J. M., 2015. Different approaches to model future burnt area in the iberian peninsula. Agricultural and Forest Meteorology 202, 11–25.

Spracklen, D. V., Mickley, L. J., Logan, J. A., Hudman, R. C., Yevich, R., Flannigan, M. D., Westerling, A. L., 2009. Impacts of climate change from 2000 to 2050 on wildfire activity and carbonaceous aerosol concentrations in the western united states. Journal of Geophysical Research: Atmospheres 114 (D20).

Stéfanon, M., D'Andrea, F., Drobinski, P., 2012b. Heatwave classification over europe and the mediterranean region. Env. Res. Lett. 7 (1), 014023.

Stéfanon, M., Drobinski, P., D'Andrea, F., de Noblet-Ducoudré, N., 2012a. Effects of interactive vegetation phenology on the 2003 summer heat waves. J. Geophys. Res. 117, D24103.

Stéfanon, M., Drobinski, P., D'Andrea, F., Lebeaupin-Brossier, C., Bastin, S., 2014. Soil moisture-temperature feedbacks at meso-scale during heat waves over western europe. Clim. Dyn. 42, 1309–1324.

Stéfanon, M., Drobinski, P., DAndrea, F., Lebeaupin-Brossier, C., Bastin, S., 2014. Soil moisture-temperature feedbacks at meso-scale during summer heat waves over western europe. Climate dynamics 42 (5-6), 1309–1324.

Stoof, C. R., Vervoort, R., Iwema, J., Elsen, E., Ferreira, A., Ritsema, C., 2012. Hydrological response of a small catchment burned by experimental fire. Hydrology and Earth System Sciences 16 (2), 267–285.

Trigo, R. M., Pereira, J., Pereira, M. G., Mota, B., Calado, T. J., Dacamara, C. C., Santo, F. E., 2006. Atmospheric conditions associated with the exceptional fire season of 2003 in portugal. International Journal of Climatology 26 (13), 1741–1757.

Trouet, V., Taylor, A. H., Wahl, E. R., Skinner, C. N., Stephens, S. L., 2010. Fire-climate interactions in the american west since 1400 CE. Geophysical Research Letters 37 (4).

Trunfio, G. A., 2004. Predicting wildfire spreading through a hexagonal cellular automata model. In: Cellular Automata. Springer, pp. 385–394.

Tryhorn, L., Lynch, A., Abramson, R., Parkyn, K., 2008. On the meteorological mechanisms driving postfire flash floods: A case study. Monthly Weather Review 136 (5), 1778–1791.

Turquety, S., Menut, L., Anav, A., Viovy, N., Maignan, F., Wooster, M., 2014. Apiflame v1. 0: high-resolution fire emission model and application to the euro-mediterranean region. Geoscientific Model Development 7, 587–612.

Val Martin, M., Logan, J., Kahn, R., Leung, F., Nelson, D., Diner, D., 2010. Smoke injection heights from fires in north america: analysis of 5 years of satellite observations. Atmos. Chem. Phys 10 (4), 1491–1510.

Van Wagner, C., Pickett, T., et al., 1985. Equations and FORTRAN program for the Canadian forest fire weather index system. Vol. 33.

Van Wagner, C., et al., 1987. Development and structure of the Canadian forest fire weather index system. Vol. 35.

Van Wagner, C. E., et al., 1974. Structure of the canadian forest fire weather index.

Vautard, R., Yiou, P., D'andrea, F., De Noblet, N., Viovy, N., Cassou, C., Polcher, J., Ciais, P., Kageyama, M., Fan, Y., 2007. Summertime european heat and drought waves induced by wintertime mediterranean rainfall deficit. Geophysical Research Letters 34 (7).

Vidale, P. L., Pielke, R. A., Steyaert, L. T., Barr, A., 1997. Case study modeling of turbulent and mesoscale fluxes over the boreas region. Journal of Geophysical Research: Atmospheres 102 (D24), 29167–29188.

Wendt, C., Beringer, J., Tapper, N., Hutley, L., 2007. Local boundary-layer development over burnt and unburnt tropical savanna: an observational study. Boundary-Layer Meteorology 124 (2), 291–304.

Westerling, A. L., Hidalgo, H. G., Cayan, D. R., Swetnam, T. W., 2006. Warming and earlier spring increase western us forest wildfire activity. science 313 (5789), 940–943.

Wooster, M. J., Roberts, G., Perry, G., Kaufman, Y., 2005. Retrieval of biomass combustion rates and totals from fire radiative power observations: Frp derivation and calibration relationships between

biomass consumption and fire radiative energy release. Journal of Geophysical Research: Atmospheres (1984–2012) 110 (D24).

Zampieri, M., D'Andrea, F., Vautard, R., Ciais, P., de Noblet-Ducoudré, N., Yiou, P., 2009. Hot european summers and the role of soil moisture in the propagation of mediterranean drought. Journal of Climate 22 (18), 4747–4758.

Abstract

The question this thesis stems from is: "To which extent weather controls the life cycle of forest fires in the Mediterranean?". The analysis developed here is based on remotely-sensed fire data, meteorological reanalyses and numerical simulations.
A large part of the thesis work focused on the impact of weather on wildfires. First I showed that weather controls the life cycle of forest fires very tightly when these fires are large enough. Many factors are crucial: the strength of the heatwave, the precipitation deficit in month preceding the summer season and finally wind speed. The relationship between fire size and wind was found very atypical by comparison with other regions (Asia, Central Europe). The largest burned areas are observed for either low wind speeds or high wind situations, with a minimum for moderate winds. This counter-intuitive behavior is observed solely during heatwaves. The causes of these different types or fire/wind relationships were identified. These results allowed to build the foundations of a statistical modeling framework that can be used to forecast not just fire risk but also the distribution of fire size and intensity. This step towards forecasting is innovative and much more informative than fire risk modeled currently used.
A second part was written about on the impact of fires on local weather. I designed a numerical sensibility study of the August 2003 Portugal fire event. In this study, I showed the triggering of inland breezes over the burned areas strengthening convection. I studied the sensibility of this phenomenon with respect to the dynamical and land-use resolution in the model. Finally I showed that burned area were favorable to increased cloudiness with an effect of increased precipitation risk (even if the precipitation signal stays very weak over the unique studied month).

Résumé

La question à la base de cette thèse est "À quel point la météorologie contrôle le cycle de vie des feux de forêts en Méditerranée?". L'analyse développée repose sur des observations satellitaires de feux, des réanalyses d'observations météorologiques et des simulations numériques.
Une grande partie du travail de thèse a porté sur l'impact de la météorologie sur les feux de forêts. Il a été tout d'abord été montré que la météorologie contrôle très fortement le cycle de vie des feux, quand ces feux sont très grands. Plusieurs facteurs sont déterminants: l'amplitude de la canicule, le déficit de précipitation des mois précédant la période estivale et enfin le vent. La relation entre surface brulée et vent s'est d'ailleurs révélée très atypique par rapport à d'autres régions du monde (Asie/Europe Centrale). Les plus grandes surfaces brulées sont observées soit pour des vents faibles, soit pour des vents forts avec un minimum aux vents intermédiaires. Ce comportement contre-intuitif n'est observé que pour les épisodes caniculaires. Les causes de ces différents types de relation feux-vent ont pu être identifiées. Ces travaux ont permis de poser les bases d'une modélisation statistique pour envisager la prévision non seulement du risque de feux mais du niveau d'extension et d'intensité du feu. Cette démarche vers la prévision est innovante et bien plus informative que les modèles de risque de feux en opération actuellement.
Une deuxième partie a porté sur l'impact des feux sur la météorologie en s'appuyant sur une étude numérique de sensibilité de l'épisode des feux du Portugal en août 2003. Dans cette étude, j'ai montré la formation de brises continentales au dessus des zones brulées renforant la convection. J'ai étudié la sensibilité de ce phénomène à la résolution du modèle et de la surface brulée. J'ai enfin montré que les surfaces brulées étaient favorables à la formation de nébulosité au dessus des zones affectées avec pour effet d'accrotre le risque de précipitation (même si le signal en précipitation reste très faible sur le seul mois étudié).